広島大学学位請求論文

Measurement of low transverse-momentum direct photons in Cu+Cu collisions at $\sqrt{s_{NN}}$ = 200 GeV

核子対あたり重心系衝突エネルギー200GeV 銅+銅原子核衝突における 低横運動量直接光子の測定

2021 年

星野 知也

目次

１． 主論文

Measurement of low transverse-momentum direct photons in Cu+Cu collisions at $\sqrt{s_{NN}}$ = 200 GeV
核子対あたり重心系エネルギー200GeV 銅+銅原子核衝突における低横運動量直接光子の測定

２． 公表論文

題目：Low-momentum direct-photon measurement in Cu+Cu collisions at $\sqrt{s_{NN}}$ = 200 GeV
著者：A. Adare et.al.,（別紙、共著者リスト①参照）
Physical Review C 98, 054902 (2018)

３． 参考論文

(1) 題目：Azimuthally anisotropic emission of low-momentum direct photons in Au+Au collisions at $\sqrt{s_{NN}}$ = 200 GeV
著者：A. Adare et.al.,（別紙、共著者リスト②参照）
Physical Review C 94, 064901 (2016)

(2) 題目：Dielectron production in Au+Au collisions at $\sqrt{s_{NN}}$ = 200 GeV
著者：A. Adare et.al.,（別紙、共著者リスト③参照）
Physical Review C 93, 014904 (2016)

共著者リスト①

A. Adare, S. Afanasiev, C. Aidala,, N. N. Ajitanand, Y. Akiba,, †, H. Al-Bataineh, J. Alexander, M. Alfred, K. Aoki,,, L. Aphecetche, R. Armendariz, S. H. Aronson, J. Asai, E. T. Atomssa, R. Averbeck, T. C. Awes, B. Azmoun, V. Babintsev, A. Bagoly, G. Baksay, L. Baksay, A. Baldisseri, K. N. Barish, P. D. Barnes, B. Bassalleck, S. Bathe, S. Batsouli, V. Baublis, A. Bazilevsky, S. Belikov, R. Belmont, R. Bennett, A. Berdnikov, Y. Berdnikov, A. A. Bickley, M. Boer, J. G. Boissevain, J. S. Bok, H. Borel, K. Boyle,, M. L. Brooks, J. Bryslawskyj, H. Buesching, V. Bumazhnov, G. Bunce,, S. Butsyk,, S. Campbell,, V. Canoa Roman, B. S. Chang, J.-L. Charvet, S. Chernichenko, C. Y. Chi, J. Chiba, M. Chiu, I. J. Choi, T. Chujo,, P. Chung, A. Churyn, V. Cianciolo, C. R. Cleven, B. A. Cole, M. P. Comets, M. Connors, P. Constantin, M. Csanád, T. Csörgő, T. Dahms, T. W. Danley, K. Das, G. David, M. B. Deaton, K. Dehmelt,, H. Delagrange, A. Denisov, D. d'Enterria, A. Deshpande, E. J. Desmond, O. Dietzsch, A. Dion, J. H. Do, M. Donadelli, O. Drapier, A. Drees, A. K. Dubey, J. M. Durham, A. Durum, V. Dzhordzhadze, Y. V. Efremenko, J. Egdemir, F. Ellinghaus, W. S. Emam, A. Enokizono, H. En'yo, S. Esumi, K. O. Eyser, W. Fan, N. Feege, D. E. Fields, M. Finger, M. Finger, Jr., F. Fleuret, S. L. Fokin, Z. Fraenkel, J. E. Frantz, A. Franz, A. D. Frawley, K. Fujiwara, Y. Fukao, T. Fusayasu, S. Gadrat, P. Gallus, P. Garg, I. Garishvili, H. Ge, A. Glenn,, H. Gong, M. Gonin, J. Gosset, Y. Goto, R. Granier de Cassagnac, N. Grau, S. V. Greene, M. Grosse Perdekamp, T. Gunji, H.-Å. Gustafsson, T. Hachiya, A. Hadj Henni, C. Haegemann, J. S. Haggerty, H. Hamagaki, R. Han, H. Harada, E. P. Hartouni, K. Haruna, S. Hasegawa, T. O. S. Haseler, E. Haslum, R. Hayano, X. He, M. Heffner, T. K. Hemmick, T. Hester, H. Hiejima, J. C. Hill, K. Hill, R. Hobbs, A. Hodges, M. Hohlmann, W. Holzmann, K. Homma, B. Hong, T. Horaguchi, D. Hornback, T. Hoshino, N. Hotvedt, J. Huang, T. Ichihara, H. Iinuma, K. Imai, M. Inaba, Y. Inoue, D. Isenhower, L. Isenhower, M. Ishihara, T. Isobe, M. Issah, A. Isupov, D. Ivanishchev, B. V. Jacak, Z. Ji, J. Jia, J. Jin, O. Jinnouchi, B. M. Johnson, K. S. Joo, D. Jouan, F. Kajihara, S. Kametani, N. Kamihara, J. Kamin, M. Kaneta, J. H. Kang, H. Kanou, D. Kawall, A. V. Kazantsev, V. Khachatryan, A. Khanzadeev, J. Kikuchi, D. H. Kim, D. J. Kim, E. Kim, E.-J. Kim, M. Kim, D. Kincses, E. Kinney, Á. Kiss, E. Kistenev, A. Kiyomichi, J. Klay, C. Klein-Boesing, L. Kochenda, V. Kochetkov, B. Komkov, M. Konno, D. Kotchetkov, D. Kotov, A. Kozlov, A. Král, A. Kravitz, J. Kubart, G. J. Kunde, B. Kurgyis, N. Kurihara, K. Kurita,, M. J. Kweon, Y. Kwon, G. S. Kyle, R. Lacey, Y. S. Lai, J. G. Lajoie, A. Lebedev, D. M. Lee, M. K. Lee, S. H. Lee, T. Lee, M. J. Leitch, M. A. L. Leite, B. Lenzi, Y. H. Leung, N. A. Lewis, X. Li, X. Li, S. H. Lim, T. Liška, A. Litvinenko, M. X. Liu, S. Lökös, B. Love, D. Lynch, C. F. Maguire, T. Majoros, Y. I. Makdisi, A. Malakhov, M. D. Malik, V. I. Manko, Y. Mao,, L. Mašek, H. Masui, F. Matathias, M. McCumber, P. L. McGaughey, D. McGlinchey, Y. Miake, A. C. Mignerey, D. E. Mihalik, P. Mikeš, K. Miki, T. E. Miller, A. Milov, S. Mioduszewski, M. Mishra, J. T. Mitchell, M. Mitrovski, G. Mitsuka,, T. Moon, A. Morreale, D. P. Morrison, S. I. Morrow, T. V. Moukhanova, D. Mukhopadhyay, J. Murata, S. Nagamiya, K. Nagashima, Y. Nagata, J. L. Nagle, M. Naglis, I. Nakagawa, Y. Nakamiya, T. Nakamura, K. Nakano,, J. Newby, M. Nguyen, B. E. Norman, R. Nouicer, T. Novák, N. Novitzky, A. S. Nyanin, E. O'Brien, S. X. Oda, C. A. Ogilvie, H. Ohnishi, M. Oka, K. Okada, O. O. Omiwade, J. D. Orjuela Koop, J. D. Osborn, A. Oskarsson, M. Ouchida,

K. Ozawa, R. Pak, D. Pal, A. P. T. Palounek, V. Pantuev, V. Papavassiliou, J. Park, S. Park, W. J. Park, S. F. Pate, M. Patel, H. Pei, J.-C. Peng, W. Peng, H. Pereira, D. V. Perepelitsa, V. Peresedov, D. Yu. Peressounko, C. E. PerezLara, C. Pinkenburg, M. L. Purschke, A. K. Purwar, H. Qu, P. V. Radzevich, J. Rak,, A. Rakotozafindrabe, I. Ravinovich, K. F. Read, S. Rembeczki, M. Reuter, K. Reygers, V. Riabov, Y. Riabov, D. Richford, T. Rinn, G. Roche, A. Romana, M. Rosati, S. S. E. Rosendahl, P. Rosnet, Z. Rowan, P. Rukoyatkin, J. Runchey, V. L. Rykov, B. Sahlmueller, N. Saito, T. Sakaguchi, S. Sakai, H. Sakata, H. Sako, V. Samsonov, M. Sarsour, S. Sato,, S. Sawada, B. K. Schmoll, J. Seele, R. Seidl, V. Semenov, R. Seto, D. Sharma,, I. Shein, A. Shevel, T.-A. Shibata, K. Shigaki, M. Shimomura, K. Shoji, A. Sickles, C. L. Silva, D. Silvermyr, C. Silvestre, K. S. Sim, C. P. Singh, V. Singh, M. J. Skoby, S. Skutnik, M. Slunečka, A. Soldatov, R. A. Soltz, W. E. Sondheim, S. P. Sorensen, I. V. Sourikova, F. Staley, P. W. Stankus, E. Stenlund, M. Stepanov, A. Ster, S. P. Stoll, T. Sugitate, C. Suire, Z. Sun, J. Sziklai, T. Tabaru, S. Takagi, E. M. Takagui, A. Taketani, Y. Tanaka, K. Tanida, M. J. Tannenbaum, A. Taranenko, P. Tarján, T. L. Thomas, R. Tieulent, M. Togawa, A. Toia, J. Tojo, L. Tomášek, H. Torii, R. S. Towell, V.-N. Tram, I. Tserruya, Y. Tsuchimoto, Y. Ueda, B. Ujvari, C. Vale, H. Valle, H. W. van Hecke, J. Velkovska, R. Vértesi,, A. A. Vinogradov, M. Virius, V. Vrba,, E. Vznuzdaev, M. Wagner, D. Walker, X. R. Wang, D. Watanabe, Y. Watanabe, F. Wei, J. Wessels, S. N. White, D. Winter, C. P. Wong, C. L. Woody, M. Wysocki, W. Xie, C. Xu, Q. Xu, Y. L. Yamaguchi, A. Yanovich, Z. Yasin, J. Ying, S. Yokkaichi, J. H. Yoo, G. R. Young, I. Younus,, H. Yu, I. E. Yushmanov, W. A. Zajc, O. Zaudtke, C. Zhang, S. Zharko, S. Zhou, J. Zimamyi, L. Zolin, and L. Zou (PHENIX Collaboration)

共著者リスト②

A. Adare, S. Afanasiev, C. Aidala, N. N. Ajitanand, Y. Akiba, R. Akimoto, H. Al-Bataineh, J. Alexander, M. Alfred, H. Al-Ta'ani, A. Angerami, K. Aoki, N. Apadula, Y. Aramaki, H. Asano, E. C. Aschenauer, E. T. Atomssa, R. Averbeck, T. C. Awes, B. Azmoun, V. Babintsev, M. Bai, G. Baksay, L. Baksay, N. S. Bandara, B. Bannier, K. N. Barish, B. Bassalleck, A. T. Basye, S. Bathe, V. Baublis, C. Baumann, S. Baumgart, A. Bazilevsky, M. Beaumier, S. Beckman, S. Belikov, R. Belmont, R. Bennett, A. Berdnikov, Y. Berdnikov, A. A. Bickley, D. S. Blau, J. S. Bok, K. Boyle, M. L. Brooks, J. Bryslawskyj, H. Buesching, V. Bumazhnov, G. Bunce, S. Butsyk,, C. M. Camacho, S. Campbell, P. Castera, C.-H. Chen, C. Y. Chi, M. Chiu, I. J. Choi, J. B. Choi, S. Choi, R. K. Choudhury, P. Christiansen, T. Chujo, P. Chung, O. Chvala, V. Cianciolo, Z. Citron, B. A. Cole, M. Connors, P. Constantin, M. Csanád, T. Csörgő, T. Dahms, S. Dairaku, I. Danchev, T. W. Danley, K. Das, A. Datta, M. S. Daugherity, G. David, K. DeBlasio, K. Dehmelt, A. Denisov, A. Deshpande, E. J. Desmond, K. V. Dharmawardane, O. Dietzsch, L. Ding, A. Dion, P. B. Diss, J. H. Do, M. Donadelli, L. D'Orazio, O. Drapier, A. Drees, K. A. Drees, J. M. Durham, A. Durum, D. Dutta, S. Edwards,, Y. V. Efremenko, F. Ellinghaus, T. Engelmore, A. Enokizono, H. En'yo, S. Esumi, K. O. Eyser, B. Fadem, N. Feege, D. E. Fields, M. Finger, M. Finger, Jr., F. Fleuret, S. L. Fokin, Z. Fraenkel, J. E. Frantz, A. Franz, A. D. Frawley, K. Fujiwara, Y. Fukao, T. Fusayasu, K. Gainey, C. Gal, P. Gallus, P. Garg,, A. Garishvili, I. Garishvili, H. Ge, F. Giordano, A. Glenn, H. Gong, X. Gong, M.

Gonin, Y. Goto, R. Granier de Cassagnac, N. Grau, S. V. Greene, M. Grosse Perdekamp, T. Gunji, L. Guo, H.-Å. Gustafsson, T. Hachiya, J. S. Haggerty, K. I. Hahn, H. Hamagaki, J. Hamblen, H. F. Hamilton, R. Han, S. Y. Han, J. Hanks, E. P. Hartouni, S. Hasegawa, T. O. S. Haseler, K. Hashimoto, E. Haslum, R. Hayano, X. He, M. Heffner, T. K. Hemmick, T. Hester, J. C. Hill, M. Hohlmann, R. S. Hollis, W. Holzmann, K. Homma, B. Hong, T. Horaguchi, Y. Hori, D. Hornback, T. Hoshino, N. Hotvedt, J. Huang, S. Huang, T. Ichihara,, R. Ichimiya, J. Ide, H. Iinuma, Y. Ikeda,, K. Imai, J. Imrek, M. Inaba, A. Iordanova, D. Isenhower, M. Ishihara, T. Isobe, M. Issah, A. Isupov, D. Ivanishchev, B. V. Jacak, M. Javani, M. Jezghani, J. Jia, X. Jiang, J. Jin, B. M. Johnson, K. S. Joo, D. Jouan, D. S. Jumper, F. Kajihara, S. Kametani, N. Kamihara, J. Kamin, S. Kanda, S. Kaneti, B. H. Kang, J. H. Kang, J. S. Kang, J. Kapustinsky, K. Karatsu, M. Kasai, D. Kawall, M. Kawashima, A. V. Kazantsev, T. Kempel, J. A. Key, V. Khachatryan, A. Khanzadeev, K. M. Kijima, B. I. Kim, C. Kim, D. H. Kim, D. J. Kim, E. Kim, E.-J. Kim, G. W. Kim, H. J. Kim, K.-B. Kim, M. Kim, S. H. Kim, Y.-J. Kim, Y. K. Kim, B. Kimelman, E. Kinney, K. Kiriluk, Á. Kiss, E. Kistenev, R. Kitamura, J. Klatsky, D. Kleinjan, P. Kline, T. Koblesky, L. Kochenda, Y. Komatsu,, B. Komkov, M. Konno, J. Koster, D. Kotchetkov, D. Kotov, A. Kozlov, A. Král, A. Kravitz, F. Krizek, G. J. Kunde, K. Kurita, M. Kurosawa, Y. Kwon, G. S. Kyle, R. Lacey, Y. S. Lai, J. G. Lajoie, A. Lebedev, B. Lee, D. M. Lee, J. Lee, K. Lee, K. B. Lee, K. S. Lee, S. Lee, S. H. Lee, S. R. Lee, M. J. Leitch, M. A. L. Leite, M. Leitgab, E. Leitner, B. Lenzi, B. Lewis, X. Li, P. Liebing, S. H. Lim, L. A. Linden Levy, T. Liška, A. Litvinenko, H. Liu, M. X. Liu, B. Love, R. Luechtenborg, D. Lynch, C. F. Maguire, Y. I. Makdisi, M. Makek, A. Malakhov, M. D. Malik, A. Manion, V. I. Manko, E. Mannel, Y. Mao, H. Masui, S. Masumoto,, F. Matathias, M. McCumber, P. L. McGaughey, D. McGlinchey, C. McKinney, N. Means, A. Meles, M. Mendoza, B. Meredith, Y. Miake, T. Mibe, A. C. Mignerey, P. Mikeš,, K. Miki,, A. Milov, D. K. Mishra, M. Mishra, J. T. Mitchell, Y. Miyachi, S. Miyasaka,, S. Mizuno, A. K. Mohanty, S. Mohapatra, P. Montuenga, H. J. Moon, T. Moon, Y. Morino, A. Morreale, D. P. Morrison, S. Motschwiller, T. V. Moukhanova, T. Murakami, J. Murata, A. Mwai, T. Nagae, S. Nagamiya, K. Nagashima, J. L. Nagle, M. Naglis, M. I. Nagy, I. Nakagawa, H. Nakagomi, Y. Nakamiya, K. R. Nakamura,, T. Nakamura, K. Nakano, C. Nattrass, A. Nederlof, P. K. Netrakanti, J. Newby, M. Nguyen, M. Nihashi, T. Niida, S. Nishimura, R. Nouicer, T. Novák, N. Novitzky, A. S. Nyanin, E. O'Brien, S. X. Oda, C. A. Ogilvie, M. Oka, K. Okada, Y. Onuki, J. D. Orjuela Koop, J. D. Osborn, A. Oskarsson, M. Ouchida, K. Ozawa, R. Pak, V. Pantuev, V. Papavassiliou, B. H. Park, I. H. Park, J. Park, J. S. Park, S. Park, S. K. Park, W. J. Park, S. F. Pate, L. Patel, M. Patel, H. Pei, J.-C. Peng, H. Pereira, D. V. Perepelitsa, G. D. N. Perera, V. Peresedov, D.Yu. Peressounko, J. Perry, R. Petti, C. Pinkenburg, R. Pinson, R. P. Pisani, M. Proissl, M. L. Purschke, A. K. Purwar, H. Qu, J. Rak, A. Rakotozafindrabe, B. J. Ramson, I. Ravinovich, K. F. Read, K. Reygers, D. Reynolds, V. Riabov, Y. Riabov,, E. Richardson, T. Rinn, D. Roach, G. Roche, S. D. Rolnick, M. Rosati, C. A. Rosen, S. S. E. Rosendahl, P. Rosnet, Z. Rowan, J. G. Rubin, P. Rukoyatkin, P. Ružička, B. Sahlmueller, N. Saito, T. Sakaguchi, K. Sakashita, H. Sako, V. Samsonov, M. Sano, S. Sano,, M. Sarsour, S. Sato, T. Sato, S. Sawada, B. Schaefer, B. K. Schmoll, K. Sedgwick, J. Seele, R. Seidl, A.Yu. Semenov, A. Sen, R. Seto, P. Sett, A. Sexton, D. Sharma, I. Shein, T.-A. Shibata, K. Shigaki, M. Shimomura, K. Shoji, P. Shukla, A. Sickles,, C. L. Silva, D. Silvermyr,, C. Silvestre, K. S. Sim, B. K. Singh, C. P. Singh,

V. Singh, M. Slunečka, M. Snowball, R. A. Soltz, W. E. Sondheim, S. P. Sorensen, I. V. Sourikova, N. A. Sparks, P. W. Stankus, E. Stenlund, M. Stepanov, A. Ster, S. P. Stoll, T. Sugitate, A. Sukhanov, T. Sumita, J. Sun, J. Sziklai, E. M. Takagui, A. Takahara, A. Taketani, R. Tanabe, Y. Tanaka, S. Taneja, K. Tanida, M. J. Tannenbaum, S. Tarafdar, A. Taranenko, P. Tarján, E. Tennant, H. Themann, T. L. Thomas, R. Tieulent, A. Timilsina, T. Todoroki, M. Togawa, A. Toia, L. Tomášek, M. Tomášek,, H. Torii, C. L. Towell, R. Towell, R. S. Towell, I. Tserruya, Y. Tsuchimoto, T. Tsuji, C. Vale, H. Valle, H. W. van Hecke, M. Vargyas, E. Vazquez-Zambrano, A. Veicht, J. Velkovska, R. Vértesi, A. A. Vinogradov, M. Virius, A. Vossen, V. Vrba,, E. Vznuzdaev, X. R. Wang, D. Watanabe, K. Watanabe, Y. Watanabe,, Y. S. Watanabe, F. Wei, R. Wei, J. Wessels, A. S. White, S. N. White, D. Winter, S. Wolin, J. P. Wood, C. L. Woody, R. M. Wright, M. Wysocki,, B. Xia, W. Xie, L. Xue, S. Yalcin, Y. L. Yamaguchi, K. Yamaura, R. Yang, A. Yanovich, J. Ying, S. Yokkaichi, J. H. Yoo, I. Yoon, Z. You, G. R. Young, I. Younus, H. Yu, I. E. Yushmanov, W. A. Zajc, A. Zelenski, C. Zhang, S. Zhou, L. Zolin, and L. Zou (PHENIX Collaboration)

共著者リスト③

A. Adare, C. Aidala, N. N. Ajitanand, Y. Akiba, R. Akimoto, J. Alexander, M. Alfred, H. Al-Ta'ani, A. Angerami, K. Aoki, N. Apadula,, Y. Aramaki,, H. Asano, E. C. Aschenauer, E. T. Atomssa, R. Averbeck, T. C. Awes, B. Azmoun, V. Babintsev, M. Bai, N. S. Bandara, B. Bannier, K. N. Barish, B. Bassalleck, S. Bathe,, V. Baublis, S. Baumgart, A. Bazilevsky, M. Beaumier, S. Beckman, R. Belmont, A. Berdnikov, Y. Berdnikov, D. S. Blau, J. S. Bok, K. Boyle, M. L. Brooks, J. Bryslawskyj, H. Buesching, V. Bumazhnov, S. Butsyk, S. Campbell, P. Castera, C.-H. Chen,, C. Y. Chi, M. Chiu, I. J. Choi, J. B. Choi, S. Choi, R. K. Choudhury, P. Christiansen, T. Chujo, O. Chvala, V. Cianciolo, Z. Citron, B. A. Cole, M. Connors, M. Csanád, T. Csörgő, S. Dairaku,, T. W. Danley, A. Datta, M. S. Daugherity, G. David, K. DeBlasio, K. Dehmelt, A. Denisov, A. Deshpande, E. J. Desmond, K. V. Dharmawardane, O. Dietzsch, L. Ding, A. Dion, P. B. Diss, J. H. Do, M. Donadelli, L. D'Orazio, O. Drapier, A. Drees, K. A. Drees, J. M. Durham, A. Durum, S. Edwards, Y. V. Efremenko, T. Engelmore, A. Enokizono, S. Esumi, K. O. Eyser, B. Fadem, N. Feege, D. E. Fields, M. Finger, M. Finger, Jr., F. Fleuret, S. L. Fokin, J. E. Frantz, A. Franz, A. D. Frawley, Y. Fukao, T. Fusayasu, K. Gainey, C. Gal, P. Gallus, P. Garg, A. Garishvili, I. Garishvili, H. Ge, F. Giordano, A. Glenn, X. Gong, M. Gonin, Y. Goto, R. Granier de Cassagnac, N. Grau, S. V. Greene, M. Grosse Perdekamp, T. Gunji, L. Guo, H.-Å. Gustafsson, T. Hachiya, J. S. Haggerty, K. I. Hahn, H. Hamagaki, H. F. Hamilton, S. Y. Han, J. Hanks, S. Hasegawa, T. O. S. Haseler, K. Hashimoto, E. Haslum, R. Hayano, X. He, T. K. Hemmick, T. Hester, J. C. Hill, R. S. Hollis, K. Homma, B. Hong, T. Horaguchi, Y. Hori, T. Hoshino, N. Hotvedt, J. Huang, S. Huang, T. Ichihara, H. Iinuma, Y. Ikeda, K. Imai, J. Imrek, M. Inaba, A. Iordanova, D. Isenhower, M. Issah, D. Ivanishchev, B. V. Jacak, M. Javani, M. Jezghani, J. Jia,, X. Jiang, B. M. Johnson, K. S. Joo, D. Jouan, D. S. Jumper, J. Kamin, S. Kanda, S. Kaneti, B. H. Kang, J. H. Kang, J. S. Kang, J. Kapustinsky, K. Karatsu, M. Kasai, D. Kawall, A. V. Kazantsev, T. Kempel, J. A. Key, V. Khachatryan, A. Khanzadeev, K. M. Kijima, B. I. Kim, C. Kim, D. J. Kim, E.-J. Kim, G. W. Kim, H. J. Kim, K.-B. Kim, M. Kim, Y.-J. Kim, Y. K. Kim, B. Kimelman, E. Kinney, Á. Kiss, E. Kistenev,

R. Kitamura, J. Klatsky, D. Kleinjan, P. Kline, T. Koblesky, Y. Komatsu, B. Komkov, J. Koster, D. Kotchetkov, D. Kotov, A. Král, F. Krizek, G. J. Kunde, K. Kurita, M. Kurosawa, Y. Kwon, G. S. Kyle, R. Lacey, Y. S. Lai, J. G. Lajoie, A. Lebedev, B. Lee, D. M. Lee, J. Lee, K. B. Lee, K. S. Lee, S Lee, S. H. Lee, S. R. Lee, M. J. Leitch, M. A. L. Leite, M. Leitgab, B. Lewis, X. Li, S. H. Lim, L. A. Linden Levy, M. X. Liu, B. Love, D. Lynch, C. F. Maguire, Y. I. Makdisi, M. Makek, A. Manion, V. I. Manko, E. Mannel, S. Masumoto, M. McCumber,, P. L. McGaughey, D. McGlinchey,, C. McKinney, A. Meles, M. Mendoza, B. Meredith, Y. Miake, T. Mibe, A. C. Mignerey, A. Milov, D. K. Mishra, J. T. Mitchell, Y. Miyachi, S. Miyasaka,, S. Mizuno, A. K. Mohanty, S. Mohapatra, P. Montuenga, H. J. Moon, T. Moon, D. P. Morrison, S. Motschwiller, T. V. Moukhanova, T. Murakami, J. Murata, A. Mwai, T. Nagae, S. Nagamiya, K. Nagashima, J. L. Nagle, M. I. Nagy, I. Nakagawa, H. Nakagomi, Y. Nakamiya, K. R. Nakamura, T. Nakamura, K. Nakano, C. Nattrass, A. Nederlof, P. K. Netrakanti, M. Nihashi, T. Niida, S. Nishimura, R. Nouicer, T. Novák, N. Novitzky, A. S. Nyanin, E. O'Brien, C. A. Ogilvie, K. Okada, J. D. Orjuela Koop, J. D. Osborn, A. Oskarsson, M. Ouchida, K. Ozawa, R. Pak, V. Pantuev, V. Papavassiliou, B. H. Park, I. H. Park, J. S. Park, S. Park, S. K. Park, S. F. Pate, L. Patel, M. Patel, H. Pei, J.-C. Peng, H. Pereira, D. V. Perepelitsa,, G. D. N. Perera, D. Yu. Peressounko, J. Perry, R. Petti,, C. Pinkenburg, R. Pinson, R. P. Pisani, M. Proissl, M. L. Purschke, H. Qu, J. Rak, B. J. Ramson, I. Ravinovich, K. F. Read,, D. Reynolds, V. Riabov, Y. Riabov, E. Richardson, T. Rinn, D. Roach, G. Roche, S. D. Rolnick, M. Rosati, Z. Rowan, J. G. Rubin, B. Sahlmueller, N. Saito, T. Sakaguchi, H. Sako, V. Samsonov, M. Sano, M. Sarsour, S. Sato, S. Sawada, B. Schaefer, B. K. Schmoll, K. Sedgwick, R. Seidl, A. Sen, R. Seto, P. Sett, A. Sexton, D. Sharma, I. Shein, T.-A. Shibata, K. Shigaki, M. Shimomura, K. Shoji, P. Shukla, A. Sickles,, C. L. Silva, D. Silvermyr, K. S. Sim, B. K. Singh, C. P. Singh, V. Singh, M. Slunečka, M. Snowball, R. A. Soltz, W. E. Sondheim, S. P. Sorensen, I. V. Sourikova, P. W. Stankus, E. Stenlund, M. Stepanov, A. Ster, S. P. Stoll, T. Sugitate, A. Sukhanov, T. Sumita, J. Sun, J. Sziklai, E. M. Takagui, A. Takahara, A. Taketani, Y. Tanaka, S. Taneja, K. Tanida,, M. J. Tannenbaum, S. Tarafdar, A. Taranenko, E. Tennant, H. Themann, R. Tieulent, A. Timilsina, T. Todoroki, L. Tomášek, M. Tomášek, H. Torii, C. L. Towell, R. Towell, R. S. Towell, I. Tserruya, Y. Tsuchimoto, T. Tsuji, C. Vale, H. W. van Hecke, M. Vargyas, E. Vazquez-Zambrano, A. Veicht, J. Velkovska, R. Vértesi, M. Virius, A. Vossen, V. Vrba,, E. Vznuzdaev, X. R. Wang, D. Watanabe, K. Watanabe, Y. Watanabe, Y. S. Watanabe, F. Wei, R. Wei, A. S. White, S. N. White, D. Winter, S. Wolin, C. L. Woody, M. Wysocki,, B. Xia, L. Xue, S. Yalcin, Y. L. Yamaguchi, R. Yang, A. Yanovich, J. Ying, S. Yokkaichi, J. H. Yoo, I. Yoon, Z. You, I. Younus, H. Yu, I. E. Yushmanov, W. A. Zajc, A. Zelenski, S. Zhou, and L. Zou (PHENIX Collaboration)

主論文

Measurement of low transverse-momentum direct photons in Cu+Cu collisions at $\sqrt{s_{NN}} = 200$ GeV

Tomoya Hoshino

March 3, 2021

Abstract

The measurement of direct photons in the experiments of relativistic heavy-ion collisions is an essential tool for exploring the hot and dense matter created by the collisions. The hot-dense matter, called Quark-Gluon Plasma, is a new state of matter in which quarks and gluons are deconfined from nucleons. Direct photons are defined by the photons that they do not arise from the hadron decays. Photons interact with the electromagnetic force, while quarks and gluons interact only by the strong force with each other. Thus, direct photons leave the created medium without interaction with other particles once produced, and they can carry the QGP information. Therefore, they are an excellent probe into the characteristics of hot-dense matter. Thermal photons emitted from the hot-dense matter are supposed to be the dominant contribution at the low transverse-momentum region. They are expected to reflect the thermodynamic properties. Therefore, measurements of low transverse-momentum direct-photons are crucial to understanding the characteristic of QGP.

The PHENIX experiment at the Relativistic Heavy Ion Collider (RHIC) has carried out the low transverse-momentum direct photon measurements in p+p, d+Au, and Au+Au collisions. Furthermore, the ALICE experiment at the Large Hadron Collider (LHC) has measured direct photons in Pb+Pb collisions with higher collision energy than RHIC. Spectra and yields of the direct photons are measured in the above experiments, and thermal properties are studied within a wide range of system size and collision energy.

We have measured low transverse-momentum direct photons by the virtual photon method in Cu+Cu collisions with the center-of-mass energy per nucleon pairs of 200 GeV taken at the PHENIX experiment in the year 2005. Virtual photons convert to low mass electron pairs through internal conversion; therefore, we measure quasi-real virtual photons that appeared as electron pairs in low invariant mass. The virtual photons are statistically extracted as excess above hadronic sources after subtracting a large amount of background. The most crucial part of this analysis is background subtraction to tackle the virtual photon component extraction. We execute to estimate the uncorrelated background by the elliptic flow adjusted mixed-event method. We carry out the well-tuned Monte Carlo simulations to estimate the correlated backgrounds from Dalitz decays and jets. The direct

photon component is successfully extracted as the direct photon fraction by fitting on the foreground distribution by backgrounds and known hadronic contribution.

The direct photon fractions, which are the direct to inclusive photon ratio, are measured as a function of transverse momentum for three collision centralities; minimum bias, 0–40%, and 40–94% centrality events. The direct photon spectra are calculated by converting from the direct photon fractions. The spectra are compared to the $N_{\rm coll}$ scaled p+p results, and the excess yields are observed in Cu+Cu collisions. The excess yields are parameterized by an exponential function, and the inverse slope gives an effective temperature $T_{\rm eff} = 285 \pm 53({\rm stat}) \pm 57({\rm syst})$ MeV/c for minimum bias events. The integrated direct photon yield called the rapidity density is calculated from the summing spectra as a function of $N_{\rm part}$. The rapidity densities for Cu+Cu collisions are compared to the Au+Au results to discuss the centrality and the collision system size dependences of the direct photon production. The Cu+Cu data provide the results in small $N_{\rm part}$ region. A power-law function can describe the $N_{\rm part}$ dependence. The rapidity densities are also compared to the results from lower to higher collision energies with several collision system as a function of charged-particle multiplicity, $dN_{\rm ch}/d\eta$. The power-law function can describe the multiplicity dependence. It supposes that the low transverse-momentum direct photons are originated in the hadron gas phase and the vicinity of QGP-hadron gas phase transition.

In conclusion, we measure low transverse-momentum direct photons in Cu+Cu collisions at $\sqrt{s_{NN}} = 200$ GeV by the virtual photon method with the PHENIX detector at RHIC. The Cu+Cu results provide the collision system size dependence of the direct photon production, especially in small $N_{\rm part}$ region. The Cu+Cu and Au+Au results follow the same scaling, and there seems to be no qualitative change in the photon sources for different collision system size. The scaling can be applied to the wide range of the collision energies, and it suggests that the source of the low transverse-momentum direct photons is near the transition from QGP to hadron phase.

Contents

List of Figures

List of Tables

Chapter 1

Introduction

Quarks and gluons are the most fundamental particles, and they constitute hadrons. Gluons hold together quarks by the strong force. Quarks and gluons cannot be taken out by themselves, and the phenomenon is called quark confinement. Relativistic heavy-ion physics aims to explore the nature of the created hot-and-dense matter where quarks and gluons are liberated from confinement. The quark deconfined phase is called Quark-Gluon Plasma. The early universe, a microsecond after the Big Bang, is considered to be Quark-Gluon Plasma. Ultra-relativistic heavy-ion collisions are the only experiments reproducing the Quark-Gluon Plasma in the laboratory.

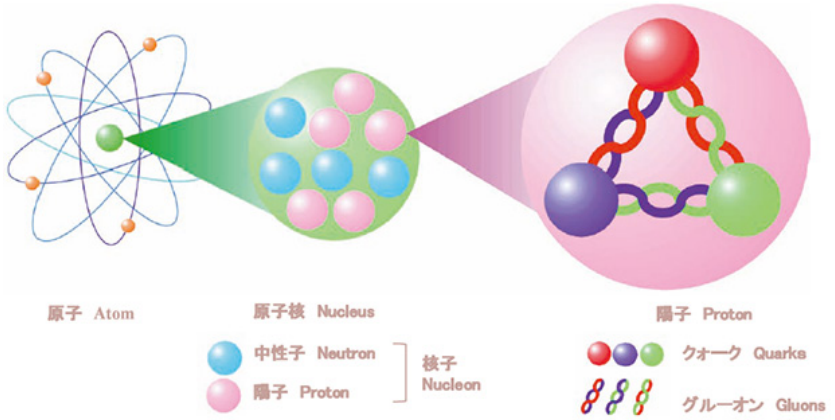

Figure 1.1: The schematic view of the hierarchy from atoms to quarks and gluons. Atoms are composed of neutrons, protons, and electrons. Quarks and gluons constitute nucleons, such as protons and neutrons. [1]

In the first half of this chapter, we introduce relativistic heavy-ion collisions and Quark-Gluon Plasma with current experimental results related to this thesis. In the last half of this chapter, we focus on explaining direct photons emitted from Quark-Gluon Plasma and describing our thesis motivation.

1.1 Quark Gluon Plasma

Quark-gluon plasma is a new state of matter that appears in high-temperature and high-density state [2]. Quarks and gluons are the most fundamental particles constituting nuclear matters. In the low-temperature state, quarks themselves are confined by the strong interaction mediated by gluons. Under extreme conditions, however, quarks and gluons are deconfined, and they constitute a plasma state. Quarks and gluons are liberated from nucleons in the plasma. In the early stage of the universe, immediately after the big bang, the state was Quark-Gluon Plasma. The phase transition to the hadronic phase occurred 10 microseconds after the big bang as the temperature dropped.

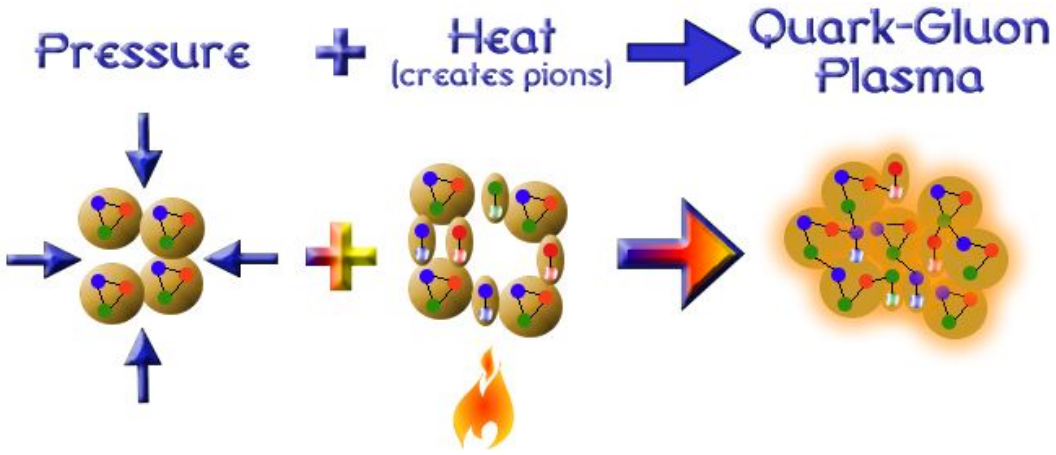

Figure 1.2: Quark-Gluon Plasma appears in the hot-and-dense condition. In the Quark-Gluon Plasma, quarks and gluons are liberated from the quark confinement. [3]

The dynamics of quarks and gluons is described by Quantum Chromodynamics (QCD), a theory of strong interactions. QCD exhibits an attribute

of the asymptotic freedom that the coupling strength between quarks and gluons decreases with increasing energy and momentum scales. The strength of the force is stronger over the long distance.

According to the asymptotic freedom property [4], under the extraordinarily high-temperature and high-density condition, quarks and gluons do not constitute hadrons, yet, they are the component of the many-body system, which is called as Quark-Gluon Plasma. The new state is first proposed by Bjorken in 1982 [5].

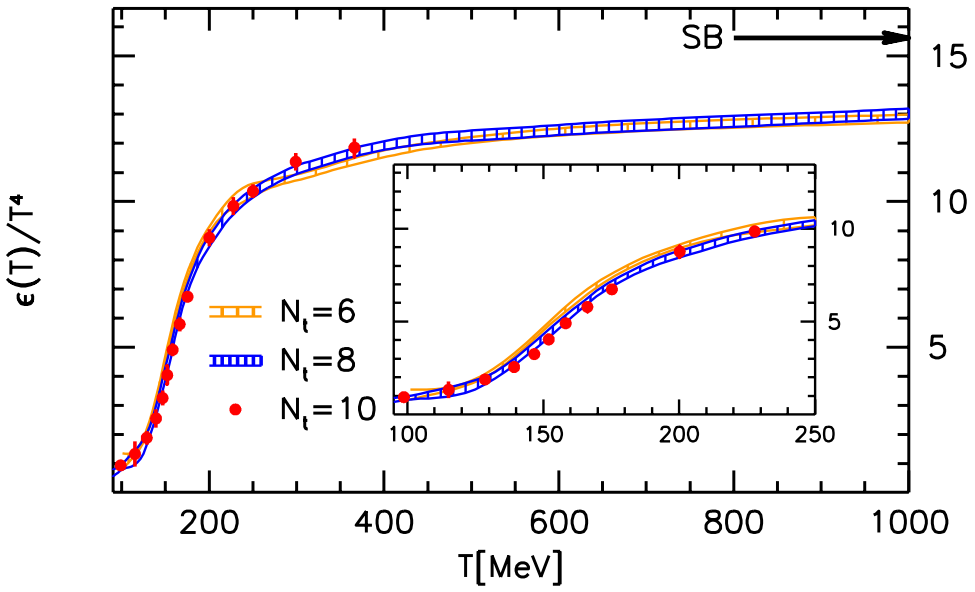

Figure 1.3: The energy density as a function of the temperature calculated by the lattice QCD. The energy density rapidly changes around the temperature $T \simeq 160$ MeV. [6]

The phase transition was initially conjectured in the 1970s and studied as a phenomenological model called the MIT bug model [7]. The model describes the QCD phase transition using phenomenology, which explains the different characteristics between the inside and outside the hadron. This model is an instinctive picture, and then the model itself is not QCD and not accurate. The phase transition temperature calculated from the boundary condition by the model is $T_c \simeq 130$ MeV. This calculation is considered with the three kinds of pions, and other hadron's contribution is ignored.

The numerical QCD lattice calculation at finite temperature based on the first-principles calculation has confirmed the QCD phase transition. Figure 1.3 shows an energy density as a function of temperature calculated by a lattice QCD [6]. This calculation considers u, d, and s quarks. The energy density rapidly changes around the temperature $T \simeq 160$ MeV. This temperature is estimated phase transition temperature, T_c and the energy density increases about ten times between a hadronic state and a QGP state.

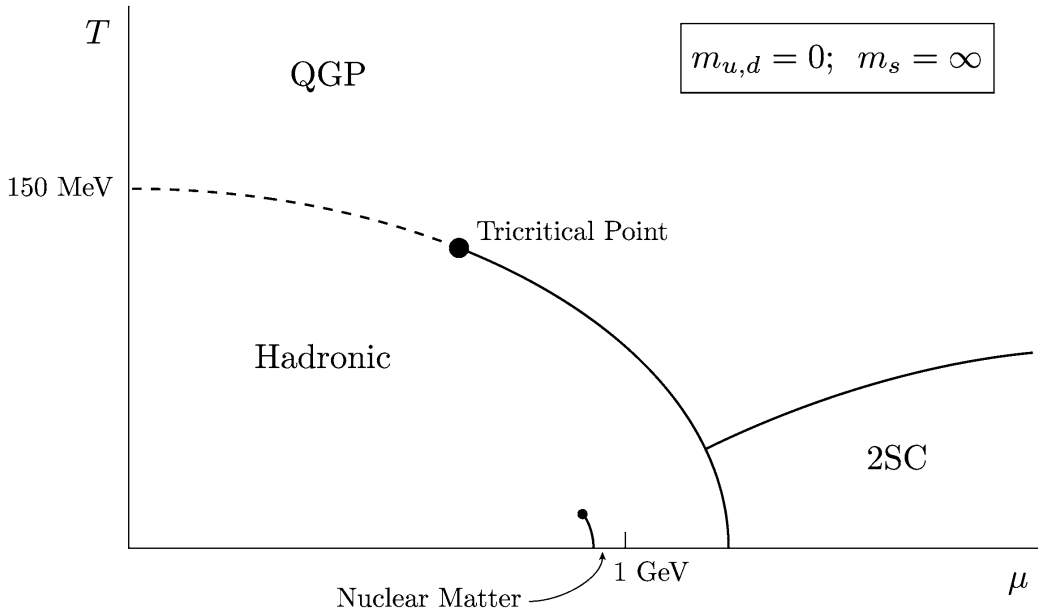

Figure 1.4: Theoretical phase diagram of nuclear matter. The black lines indicate the phase transition between different phases. The diagram shows as a function of temperature T and baryon chemical potential μ. [8]

Figure 1.4 shows a theoretical QCD phase diagram [8], which shows the state of matter with the relationship between temperature and energy density. Although the lattice QCD calculations indicate the phase transition to QGP from the hadronic phase and critical temperature T_c. However, the boundary between the hadronic matter and the QGP matter is still unknown, and the characteristic of QGP is also not yet fully understood experimentally.

1.2 Relativistic heavy-ion collisions

Quark-Gluon Plasma appears in high temperature and low baryon density, such as in the early Universe at the first 10^{-5} seconds after the Big Bang. The only possible approach to create the QGP state in the laboratories is the ultra-relativistic heavy-ion collision experiments. The experiments can reproduce the hot-and-dense condition by colliding the heavy nuclei, such as coppers and golds.

The heavy-ion collision experiments can achieve the high-temperature and high-density conditions by accelerating and colliding ions up to near the speed of light. Many experiments have researched the QGP state and explored its characteristics with the various collision systems and energies.

Researching the QGP state in Relativistic Heavy Ion Collider (RHIC) at Brookhaven National Laboratory (BNL) began in the year 2000 with the Au+Au collisions at $\sqrt{s_{NN}} = 130$ GeV. In the next year, 2001, the full energy of $\sqrt{s_{NN}} = 200$ GeV in Au+Au collisions was archived. Extensive results of experimental observations in RHIC implies the formation of QGP [9, 10, 11, 12]. In the Large Hadron Collider (LHC) at CERN, several experiments are also researching the characteristic of QGP. The LHC has begun operating in 2008, and the collider can reach to a higher collision energy than RHIC, $\sqrt{s} = 14$ TeV for p+p and $\sqrt{s_{NN}} = 5.5$ TeV for Pb+Pb collisions.

Two major results would implicate the production of high-temperature and high-density matter created in the heavy-ion collisions. High transverse-momentum particle suppression is the first measurement that high transverse-momentum particle productions are strongly suppressed compared to that of p+p collisions [13]. The results imply that the particles produced in initial hard scattering interact with the hot-and-dense matter and lose their energy. The other significant result is the strong elliptic flow [14]. The produced particle distribution in momentum space is not uniform but has azimuthal anisotropy with respect to the reaction plane. The overlapping region of two nuclei is a short ellipse in the direction of the reaction plane, and the inside of the region is high pressure. The generated particles follow the pressure gradient and are in motion. Consequently, the geometry of the collisions is converted into an anisotropy in momentum space. It was found that the viscosity of the produced matter is close to zero, the perfect-fluid, by comparing to the relativistic hydrodynamic calculations [15].

1.3 Geometry of heavy ion collisions

The Glauber model quantifies the geometrical configuration of the collision. The model is widely used in high-energy heavy-ion physics. It can express the collision geometry as the impact parameter b, the number of binary nucleon-nucleon collisions N_{coll}, the number of participating nucleons N_{part} and the nuclear overlap function $T_{AB}(b)$ [16].

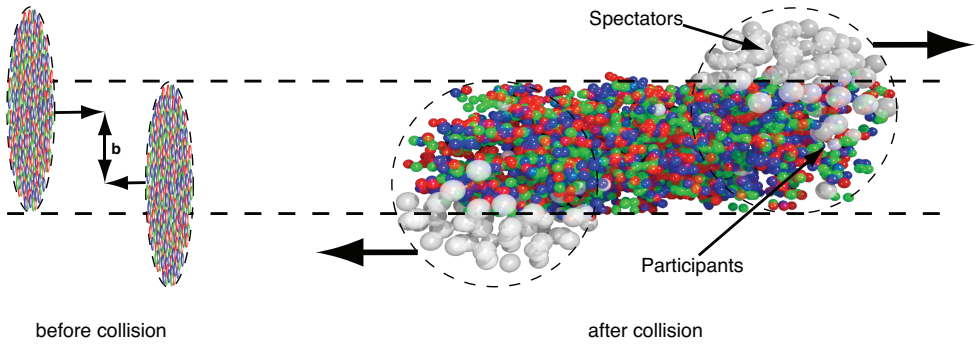

Figure 1.5: A schematic image of the heavy ion collision [17]. Left: Two nuclei collide with the impact parameter b before the collision. Right: After the collision, the spectator nucleons pass away in the longitudinal direction, while particles are produced in the participant zone.

Two nuclei are accelerated to close to the speed of light by accelerator and collide in the ultra-relativistic heavy-ion experiment. These nuclei appear 'pancake' due to the Lorentz contraction and collide with geometrical overlap. The overlap is defined by the impact parameter b shown in Fig. 1.5. The parameter b is associated with centrality in the experiment. Besides, the interacting nucleons in the geometrical overlap region are called participants, and the nucleons outside the region are called spectators, which are unaffected by the collisions. N_{coll} is the total number of nucleon-nucleon collisions in the participants, whereas N_{part} is the total number of the nucleons included in the participants.

The distribution of nucleons in a nucleus can be described with the nuclear density $\rho_A(\boldsymbol{r})$ as

$$T_A(\boldsymbol{s}) = \int dz \rho_A(z, \boldsymbol{s}) \tag{1.1}$$

where $\boldsymbol{s}$ is the coordinates in (x, y), which indicates the center of nucleus. The nuclear overlap function of nucleus A and B can be expressed using the parameter b, T_A and T_B as

$$T_{AB}(\boldsymbol{b}) = \int d^2 s T_A(\boldsymbol{s}) T_B(\boldsymbol{s} - \boldsymbol{b}). \tag{1.2}$$

where $d^2 s = 2\pi s ds$ is the two dimensional overlap area.

The number of binary nucleon-nucleon collisions N_{coll} is described using T_{AB} as

$$N_{\text{coll}}(b) = \int d^2 s \sigma_{NN}^{in} T_A(\boldsymbol{b}) T_B(\boldsymbol{s} - \boldsymbol{b}) = \sigma_{NN}^{in} \cdot T_{AB}(\boldsymbol{b}) \tag{1.3}$$

where σ_{NN}^{in} is the inelastic cross section of the nucleon-nucleon interaction.

The number of participating nucleons N_{part} is

$$\begin{aligned} N_{\text{part}} = & \int d^2 s T_A(\boldsymbol{s}) \left(1 - \exp\left(-\sigma_{NN} T_B(\boldsymbol{s} - \boldsymbol{b})\right)\right) \\ & + \int d^2 T_B(\boldsymbol{s} - \boldsymbol{b}) \left(1 - \exp\left(-\sigma_{NN} T_A(\boldsymbol{s})\right)\right). \end{aligned} \tag{1.4}$$

1.4 Space time evolution

Figure 1.6 shows the schematic diagram of the space-time evolution in heavy-ion collisions. Relativistic heavy-ion collisions produce hot and dense matter. The created matter develops while undergoing several phases from the initial hard scattering to the final hadron emission. The time evolution of the heavy-ion collisions is as follows.

Pre equilibrium

Two accelerated heavy ions collide head-on and pass through each other, causing nucleons to release kinetic energy in the overlapping region where passed nuclei through. The collision occurs at $z = 0$ and time $t = 0$ along the longitudinal axis in the center of mass frame. Initial hard scattering between partons occurs, and the overlap region becomes high energy density. This phase is named the pre-equilibrium phase, and perturbative QCD following parton cascade can describe this phase. This phase becomes a local thermal-equilibrium state shortly.

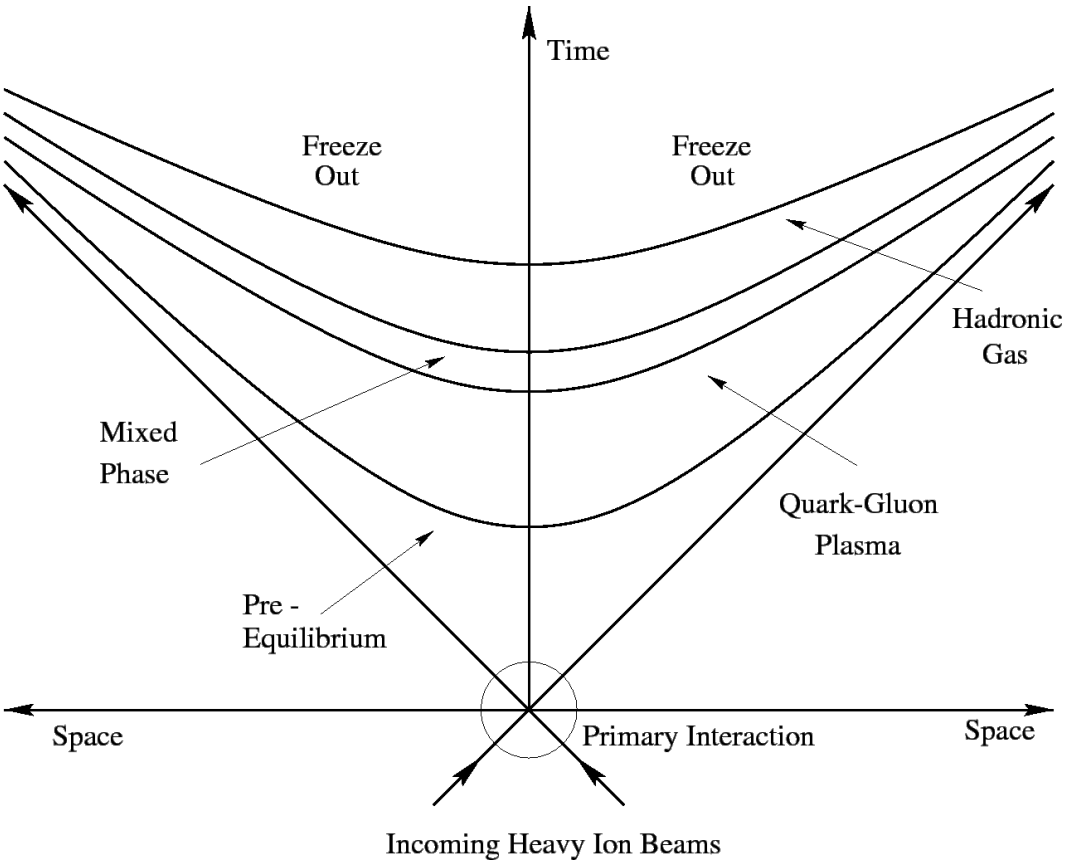

Figure 1.6: A schematic diagram of the space-time evolution in heavy-ion collisions. Quark-Gluon Plasma is formed through a pre-equilibrium state after the heavy-ion collision. Produced particles, including hadrons, photons, and leptons, are detected after the freeze-out. [18]

Quark-Gluon Plasma

The reaction area expands by the initial pressure in the collision. Quarks and gluons continue to lead to multiple scattering; eventually, the system would reach the local thermal equilibrium. The system reaches sufficient temperature 300∼600 MeV and energy density to form Quark-Gluon Plasma (QGP). The formation time is expected to be ∼0.6 fm/c. The hydrodynamics can describe this QGP phase.

Mixed phase and Hadronic gas

After the QGP formation, the system expands rapidly, and thereby the temperature drops down to the critical temperature $T_c \approx 170$ MeV. Once the QGP matter reaches the T_c, the matter begins to hadronize in which quarks and gluons are confined into hadrons. This phase is called the hadronic gas. The hadronic matter expands with the collectivity, and the system temperature goes down.

The mixed phase exists if the transition has occurred in the first-order phase transition in which thermodynamic variable discontinuously changes. The perturbative QCD calculations suggest that the transition is cross-over that the variables change continuously.

Freeze out

The system shifts to the freeze-out phase when the temperature reaches the freeze-out point $T_F \approx 100$ MeV. The type of particles is fixed because the interacting particles' mean free path is smaller than the system size. Finally, the elastic collisions between hadrons cease, and the system reaches a thermal freeze-out point, whereby the momentum of all particles are frozen.

1.5 Direct photons and thermal photons

Direct photons are the photon that they do not arise from hadron decays [19]. They are an essential probe to understand the characteristics of hot and dense matter created in the ultra-relativistic nucleus-nucleus collisions. Electromagnetic probes include direct photons, are rare probes in the heavy-ion collisions because the coupling constant $\alpha = \frac{e^2}{4\pi\hbar c}$ in QED is smaller than the constant $\alpha_s = \frac{g_s^2}{4\pi\hbar c}$ in QCD. Photons only interact with the electromagnetic force, while quarks and gluons interact with the strong force. Therefore, photons can carry pure information about the phase where they are emitted [20]. Besides, photons are produced in the whole stages of the time evolution in the heavy-ion collisions. Consequently, direct photons are a clean probe to understand the time-evolution of the created system in heavy-ion collisions.

Typical photon sources in heavy-ion collisions are shown in Fig. 1.7 [21]. Photons are generally classified into direct photons and decay photons. Decay photons are originated from electromagnetic decays of hadrons such as $\pi^0 \to \gamma\gamma$. Direct photons arise from the initial hard scattering, thermal

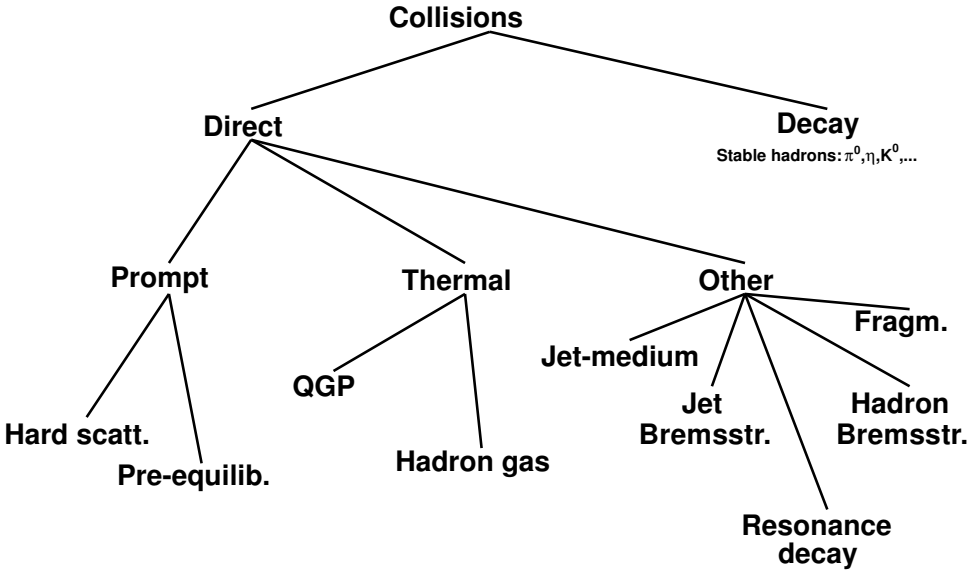

Figure 1.7: Sources of direct photons in heavy-ion collisions. Produced photons in the heavy-ion collisions are classified into two types: direct photons and decay photons. [21]

radiations from QGP and hadron gas, and other sources. The initial hard scattering produces prompt photons, and the perturbative QCD models can express it. Thermal photons are emitted as the black-body radiation from the hot medium. Thermal photon measurement is direct proof to ensure that the created matter is above the phase transition temperature, and it also can access the thermal equilibrium time of the medium. Figure 1.8 shows a theoretical prediction of direct photon yield as a function of transverse momentum in Au+Au collisions at $\sqrt{s_{NN}} = 200$ GeV [22]. Above the 3 GeV/c region, the major source is pQCD photons by initial hard scattering of the collisions. Below the 1 GeV/c region, the dominant source is thermal photons emitted from the hadron gas. The QGP thermal radiation is most sensitive between $1 < p_T < 3$ GeV/c. The contribution of decay photons is about 10 times that of direct photons. In the experiments, photons are measured as an integral of all photon sources, including direct and decay photons. Direct photons are measured by subtracting decay photon contributions.

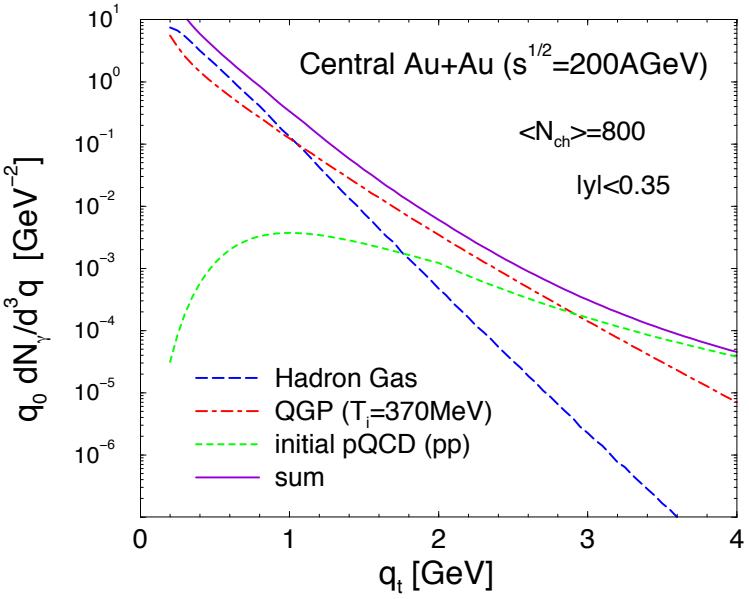

Figure 1.8: A theoretical prediction of direct photon yield as a function of transverse momentum in Au+Au collisions at $\sqrt{s_{NN}}$ = 200 GeV. Each photon source has a different dominant transverse-momentum region. [22]

1.6 Direct virtual photons

Any sources of high-energy photons also emit virtual photons that the photons convert into low invariant-mass electron pairs (e^+e^- pairs). If virtual photon invariant-mass m_{γ^*} is more than twice of electron mass m_e, the virtual photon converts to an electron pair. This production attributes the higher-order process of direct photon production.

Figure 1.9 shows an example of the virtual photon production in gluon Compton scattering. The Compton scattering occurs at the initial collision in heavy-ion collisions. The scattering process associates with producing low invariant-mass electron pairs through the internal conversion. Another source of the virtual photon is Dalitz decays ($\pi^0 \rightarrow \gamma + \gamma^* \rightarrow \gamma + e^+e^-$) described by the Kroll-Wada formula [23].

The associated electron pair production can relate to photon production

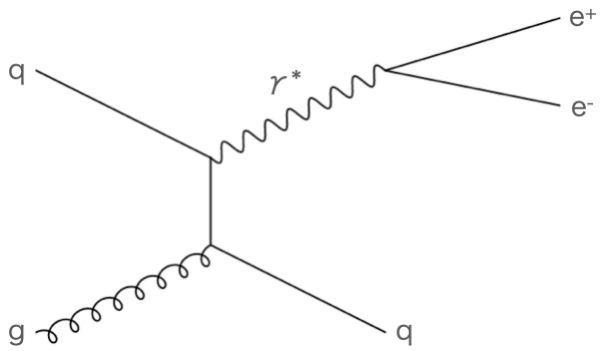

Figure 1.9: Feynman diagram of quark-gluon Compton scattering ($qg \rightarrow g\gamma^* \rightarrow e^+e^-q$)

with the formula written as

$$\frac{dN^2}{dm_{ee}} = \frac{2\alpha}{3\pi}\frac{1}{m_{ee}}\sqrt{1-\frac{4m_e^2}{m_{ee}^2}}\left(1+\frac{2m_e^2}{m_{ee}^2}\right)SdN_\gamma \tag{1.5}$$

where α, m_e, m_{ee} are the fine-structure constant, the electron and the electron-pair mass, respectively. S is a process dependent factor, including a form factor and a phase-space. For virtual photons, the factor goes to 1 as $m_{ee} \rightarrow 0$ or $m_{ee} \ll p_T$. Equation 1.5 describes the relationship not only decays from virtual photons but also electron pairs from Dalitz decays. Therefore, the shape of invariant mass distributions is different between virtual photons and electron pairs from Dalitz decays.

1.7 Related measurements

This section introduces dielectron and direct photon results measured in several collision systems and energies in RHIC at BNL and the LHC at CERN. We primarily focus on the low transverse-momentum region in heavy-ion collisions, which are directly related to the thesis. Dielectrons are produced throughout the entire stages of the collision system time-evolution, as well as direct photons. These electromagnetic probes have no color charge, and therefore they can provide clean information to understand the time evolution of the created matter.

1.7.1 Dielectron measurement

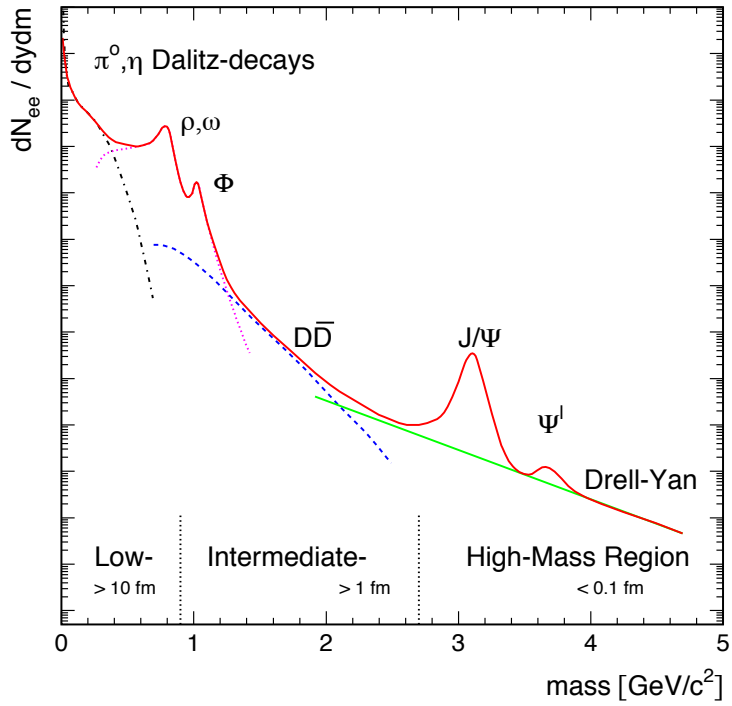

Figure 1.10: Expected dielectron source in heavy-ion collisions [24]

Electron-positron pairs or dielectrons are an excellent probe for understanding the created matter's time-evolution due to escaping from the matter without final state interactions. Therefore, the dielectron spectra contain the whole time evolution and dynamics. The properties of low-mass vector mesons are a candidate for searching chiral symmetry restoration in the high-temperature state. Moreover, the direct photon contribution from the internal conversion is also included in the spectra at the low invariant mass region.

Figure 1.10 shows an expected dielectron spectrum in heavy-ion collisions [24]. The spectra can be classified into three regions: the high-mass, intermediate-mass, and low-mass regions. The high-mass region is located above the J/Ψ invariant mass. The dominant contribution in this region is the hard scattering on partons. Dielectrons are produced through the Drell-

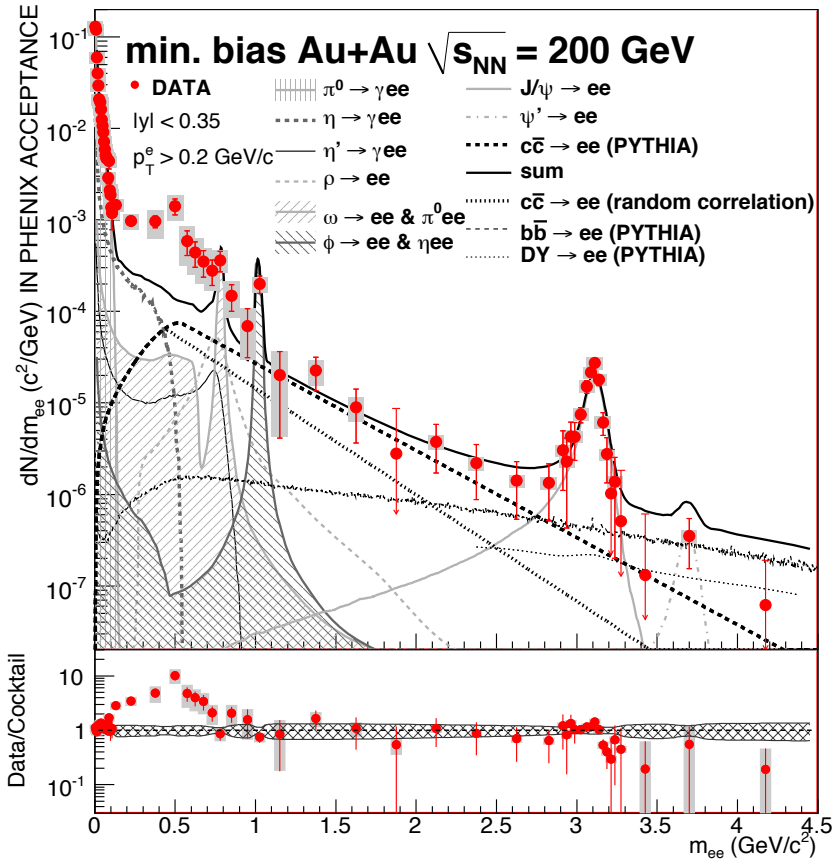

Figure 1.11: Dielectron spectrum in minimum bias Au+Au collisions at $\sqrt{s_{NN}}$ =200GeV measured by the PHENIX experiment [25]

Yan process ($q\bar{q} \to l^+l^-$) and correlated semi-leptonic decays of heavy quark pairs, as well as J/Ψ and Ψ' particles. The invariant mass range between ϕ and J/Ψ is the intermediate region. Thermal radiation dielectrons arisen from the hot medium are expected to contribute to the region by the theoretical models. The electron pairs originated from the semi-leptonic decay of $c\bar{c}$ is a dominant background in the intermediate-mass region. The low-mass region places under the ϕ meson invariant mass. Dalitz decays of π^0 and η mesons contributes as the dominant source, and ρ and ω also appear in the region. In-medium decay of ρ meson arising from the hadronic phase is expected to be another dominant source. The lifetime of the ρ meson, 1.3

fm/c, is much shorter than the expected lifetime of the hadronic phase, and ρ couples to the $\pi\pi$ channel strongly. Therefore, the shape and the yield can reflect on the medium modifications due to chiral symmetry restoration [26]. In addition, the quasi-real virtual photon contribution appears in the region where the low transverse-momentum is much greater than its invariant mass. Any source of real photons also emits virtual photons, which convert to low mass dielectrons. The contribution arises from the initial hard scattering such as Compton scattering and thermal radiation from the hot medium.

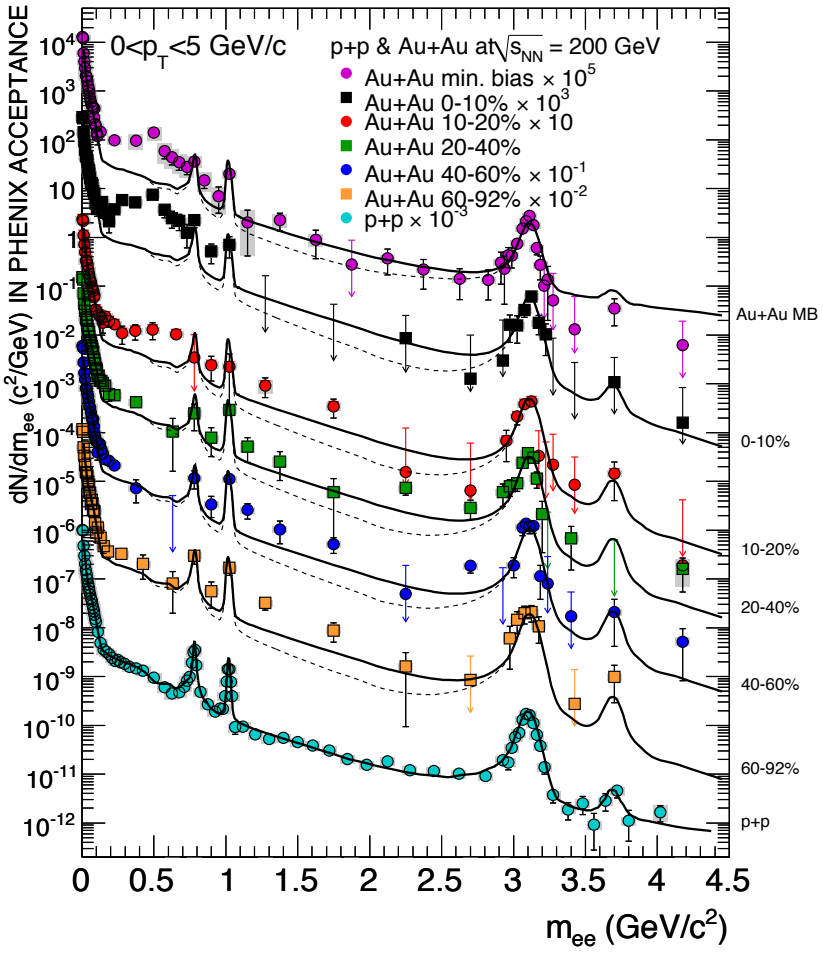

Figure 1.12: Dielectron spectrum in p+p and Au+Au collisions at $\sqrt{s_{NN}}$ =200GeV measured by the PHENIX experiment [25]

Dielectron spectra have been measured in p+p and Au+Au collisions at $\sqrt{s_{NN}}$ = 200 GeV reported by the PHENIX experiment [25]. Figure 1.11 shows the inclusive dielectron invariant-mass spectrum in minimum-bias Au+Au collisions. The inclusive spectrum is compared to expectations from hadronic decays, heavy flavor, and Drell-Yan contributions, which are evaluated by the well-tuned simulations. The data and expectations are compared as a ratio. An enhancement appears at the low invariant-mass region. The enhancement factor, defined as the ratio between the measured and the expected yields, is studied for different centralities. The enhancement increases with centrality, and it is qualitatively consistent with the conjecture that an in-medium enhancement arises from the scattering process of $\pi\pi$ or $q\bar{q}$ annihilation. Figure 1.13 shows the measured spectra for six centrality bins in Au+Au collisions, together with p+p results. The expectations from the hadron decay models represented by the solid and dashed lines are compared to the measurements. The detailed study of the enhancement is reported by the PHENIX experiment [27]. The excess yields calculated by the data subtracted hadronic cocktail excluding vacuum ρ are consistent with the expectations from the thermal radiation from the hadronic (ρ broadening) and QGP phases.

The STAR experiment measures the dielectron production in several collision energies from $\sqrt{s_{NN}}$ = 19.6 to 200 GeV [28, 29, 30]. The RHIC collider provided several beam energies to study the phase diagram of the QCD matter, and the program is called the Beam Energy Scan. Figure 1.14 shows the results of the dielectron spectra with several collision energies from $\sqrt{s_{NN}}$ = 19.6 to 200 GeV [30]. The enhancement in the invariant mass region of the ω and ϕ mesons are studied in several collision energies. The invariant mass and width of vector mesons could be modified because of interactions with the hot and dense matter. The STAR experiment studies the mass shape and width of ω and ϕ in Au+Au collisions at $\sqrt{s_{NN}}$ = 200 GeV [29]. The mass shift from the measurement agrees with the PDG values within the uncertainties.

Dielectron invariant-mass spectra in Cu+Cu collisions at $\sqrt{s_{NN}}$ = 200 GeV are reported as a preliminary result by the PHENIX experiment [31]. The spectra for 0–10% and 10–20% are shown in Fig. 1.15. The inclusive spectra are compared to the expectations from hadronic cocktail, heavy flavor, and Drell-Yan contributions. The large enhancement in the mass above the pion mass and below the omega mass is reported in the minimum bias events.

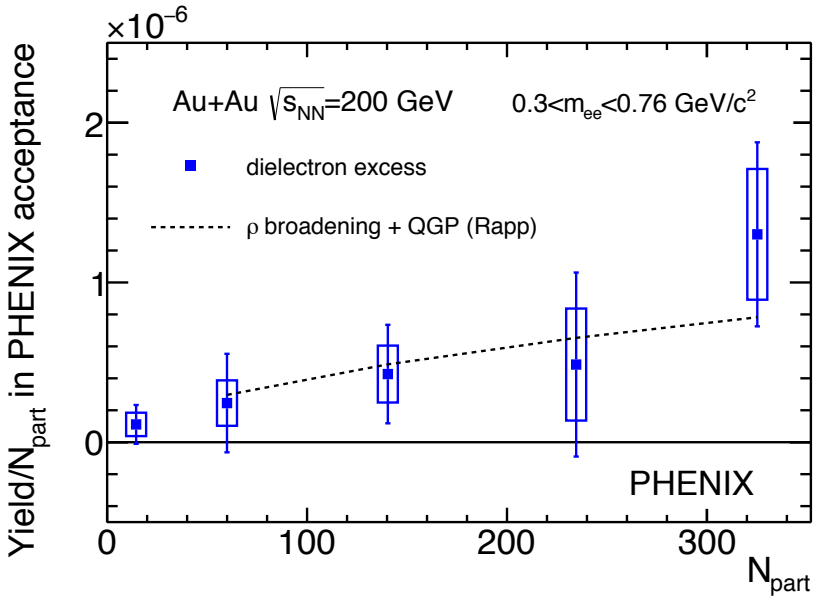

Figure 1.13: Centrality dependece of the dielectron enhancement in $0.3 < m_{ee} < 0.76$ GeV/c^2 in Au+Au collisions at $\sqrt{s_{NN}} = 200$ GeV. The dielectron yields after subtracting the hadronic cocktail without ρ broadening are compared to the model calculations. [27]

Dielectron azimuthal anisotropy is measured in Au+Au collisions at $\sqrt{s_{NN}} =$ 200 GeV by the STAR experiment [32]. The result of dielectron azimuthal anisotropy at the low invariant mass region, $m_{ee} < 1.1$ GeV/c^2, is consistent with the simulated anisotropy for π^0, η, ω, and ϕ. The dielectron anisotropy at high mass region, $1.1 < m_{ee} < 2.9$ GeV/c^2, is consistent with the estimated anisotropy magnitude from $c\bar{c}$ contribution.

1.7.2 Direct photon spectra

Direct photons are also a clean probe in heavy-ion collisions because they are color blind particles originating from the whole stage. Direct photons carry pure information about the property of created matter. Supposing the hot-and-dense matter is created in the heavy-ion collisions, the matter would radiate thermal photons. Thermal photons are assumed that they appear in the low transverse-momentum region by theoretical models. Meanwhile, the

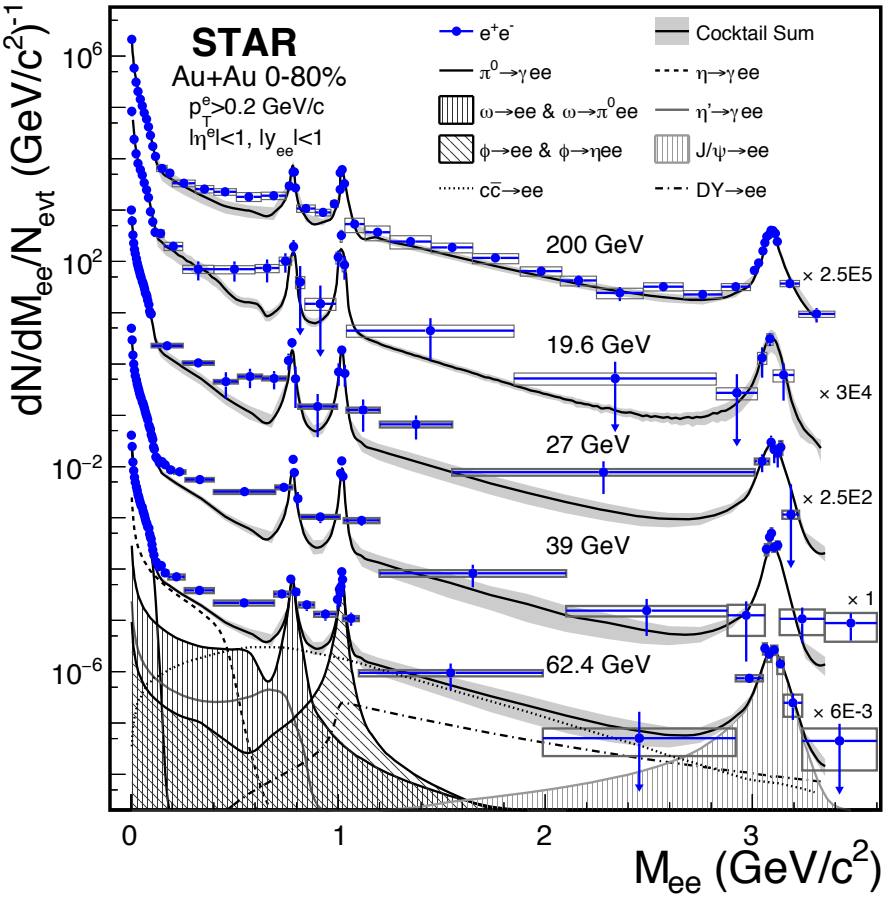

Figure 1.14: Dielectron spectra in Au+Au collisions with several collision energies measured by the STAR experiment [30]

prompt photons produced in the initial hard scattering are the dominant contribution at the high transverse momentum region.

Direct photons at high-transverse momentum region

Direct photons at the high transverse-momentum region are mainly produced by the initial hard scattering. The PHENIX experiment measures centrality dependence of direct photon production in Au+Au collisions at $\sqrt{s_{NN}} = 200$ GeV [33]. Direct photons are measured by subtracting the decay photons from the inclusive photons. Accordingly, experiments measure the inclusive

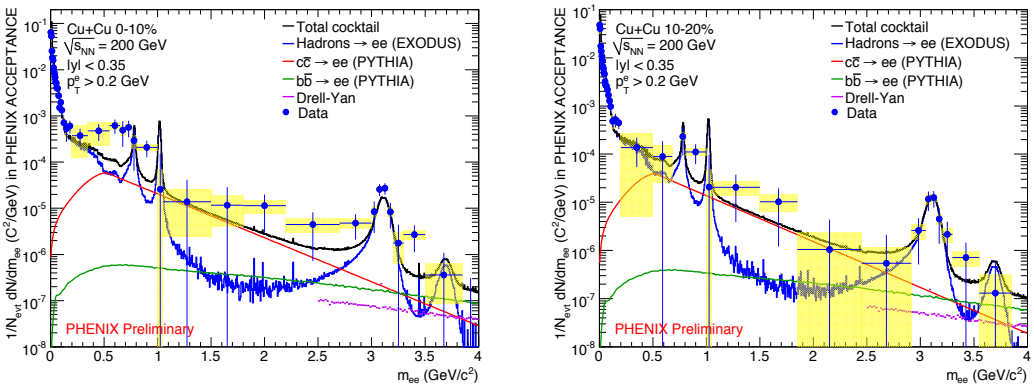

Figure 1.15: Dielectron spectra in Cu+Cu collisions at $\sqrt{s_{NN}} = 200$ GeV for 0–10% (left) and 10–20% (right) centrality classes measured by the PHENIX experiment [31]

photon spectra, whereas the Monte Carlo simulations evaluate the decay photon spectra based on the measured π^0 and η spectra. The following double ratio is defined:

$$R_\gamma = \frac{(\gamma/\pi^0)_{\text{Measured}}}{(\gamma/\pi^0)_{\text{Background}}} \approx \frac{\gamma_{\text{Measured}}}{\gamma_{\text{Background}}}. \tag{1.6}$$

The denominator is the ratio of background photon to π^0, while the numerator is the ratio of the measured photon to π^0. Significant deviations of the double ratio above unity indicate a direct photon excess. Figure 1.16 shows the double ratio in Au+Au collisions at $\sqrt{s_{NN}} = 200$ GeV. A significant excess is observed at high transverse-momentum.

Direct photon spectra are calculated from the double ratio and measured inclusive spectra and it expresses as

$$\gamma_{\text{direct}} = \left(1 - R_\gamma^{-1}\right) \gamma_{\text{measured}}. \tag{1.7}$$

The calculated direct photon spectra for various centralities are shown in Fig. 1.17. The vertical error bars with the arrow indicate the measurement consistent with zero yields. The solid curves in the figures express perturbative QCD predictions. The theoretical calculations can describe the measured data well, especially in the high transverse-momentum region. Meanwhile, in the low transverse-momentum region, the total errors are too large to compare with the pQCD predictions adequately.

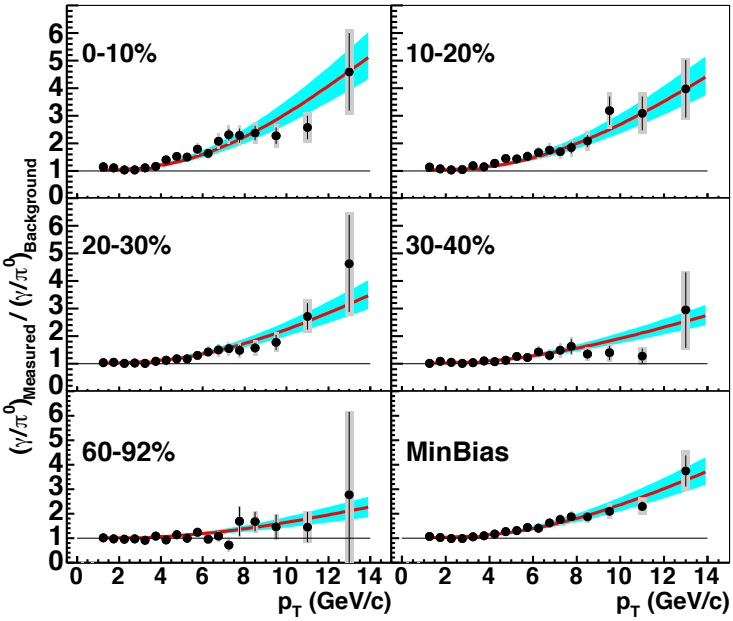

Figure 1.16: The double ratio of measured $(\gamma/\pi^0)_{\text{Measured}}$ invariant yield ratio to the background decay $(\gamma/\pi^0)_{\text{Background}}$ ratio as a function of transverse momentum in Au+Au collisions at $\sqrt{s_{NN}} = 200$ GeV measured by the real photon measuremnet in the PHENIX experiment [33]

The direct photon yields in the high transverse momentum region can be described by the N_{coll} scaling from p+p collisions, whereas the hadron yields are suppressed in the heavy-ion collisions [34, 35]. The suppression can be measured by the R_{AA} variable given by

$$R_{AA} = \frac{E\frac{d^3N_{AA}}{dp^3}}{N_{\text{coll}}E\frac{d^3N_{pp}}{dp^3}} = \frac{E\frac{d^3N_{AA}}{dp^3}}{T_{AA}\frac{d^3N_{pp}}{dp^3}}. \tag{1.8}$$

Here, the denominator and numerator denote the T_{AA} scaled invariant yield in p+p collisions and invariant yield in heavy-ion collisions, respectively.

Direct photons at low transverse momentum

At the low transverse-momentum region, thermal photons from the hot medium are expected the dominant source. Direct photon spectrum in rela-

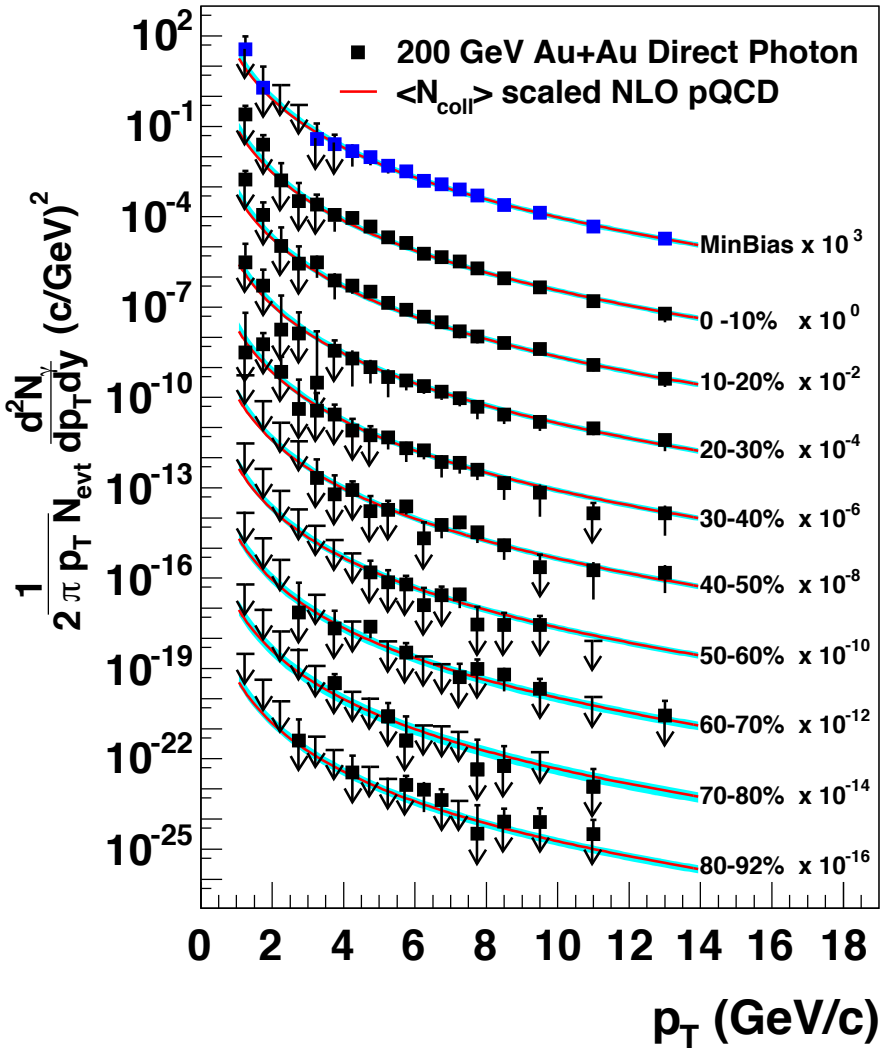

Figure 1.17: Direct photon spectra as a function of transverse momentum in Au+Au collisions at $\sqrt{s_{NN}}$ =200GeV measured by the PHENIX experiment. The spectra are obtained for nine centrality bins, and the solid curves denote the pQCD predictions. [33]

tivistic heavy-ion collisions was first measured in the WA98 collaboration at the SPS collider in CERN [36, 37]. The direct photon yield measurement in the central Pb+Pb collisions was interpreted either as thermal photons from

QGP or multiple soft scatterings without QGP formation [38]. The PHENIX experiment at RHIC has successfully measured low transverse-momentum direct-photons in p+p, d+Au, and Au+Au collisions at $\sqrt{s_{NN}} = 200$ GeV [25, 39, 40]. Thermal photons are observed in Au+Au collisions, whereas the p+p and d+Au results are consistent with the pQCD calculations. As mentioned above, the signal-to-background ratio in real photon measurements worsens at the low transverse-momentum region due to the vast number of backgrounds and detector resolution degradation. Therefore, the measurements have done by the virtual photon method. The method uses the internal conversion that the virtual photons convert to electron pairs. The method improves the signal-to-background ratio by a factor of about 5 to avoid π^0 meson contribution.

The first measurement of thermal photons is reported in Au+Au collisions at $\sqrt{s_{NN}} = 200$ GeV by the PHENIX experiment [39]. The direct photon spectra for three centrality bins are shown in Fig. 1.18. The Au+Au results with three centralities are presented together with the p+p results. The theoretical prediction from pQCD calculations describes the p+p results well, while an excess over the prediction is observed in Au+Au collisions. The direct photo excess yields in Au+Au collisions are implied by the thermal radiation from the QGP matter. The effective temperature is obtained from the fit by an exponential function to the yields, and $T = 233$ MeV/c for the minimum bias collisions. The STAR experiment also measure direct photons via the virtual photon in Au+Au collisions at $\sqrt{s_{NN}} = 200$ GeV with the transverse momentum ranges $1 < p_T < 3$ GeV/c and $5 < p_T < 10$ GeV/c [41].

It is remarkable that the direct photons at $\sqrt{s_{NN}} = 200$ GeV are only measured in p+p, d+Au and Au+Au, yet to be measured in Cu+Cu collisions. Consequently, it is worth measuring the direct photons in Cu+Cu collisions to compare the other collision system at the same collision energy to study the collision system-size dependence.

1.7.3 Centrality dependency of direct photons

Low transverse-momentum direct photons are also measured by the external conversion method. The method improves the real photon measurement, and it uses the conversion electron pairs originated in the interaction between real photons and detector materials. The direct photon measurement via the external conversion extends to the lower side of the transverse mo-

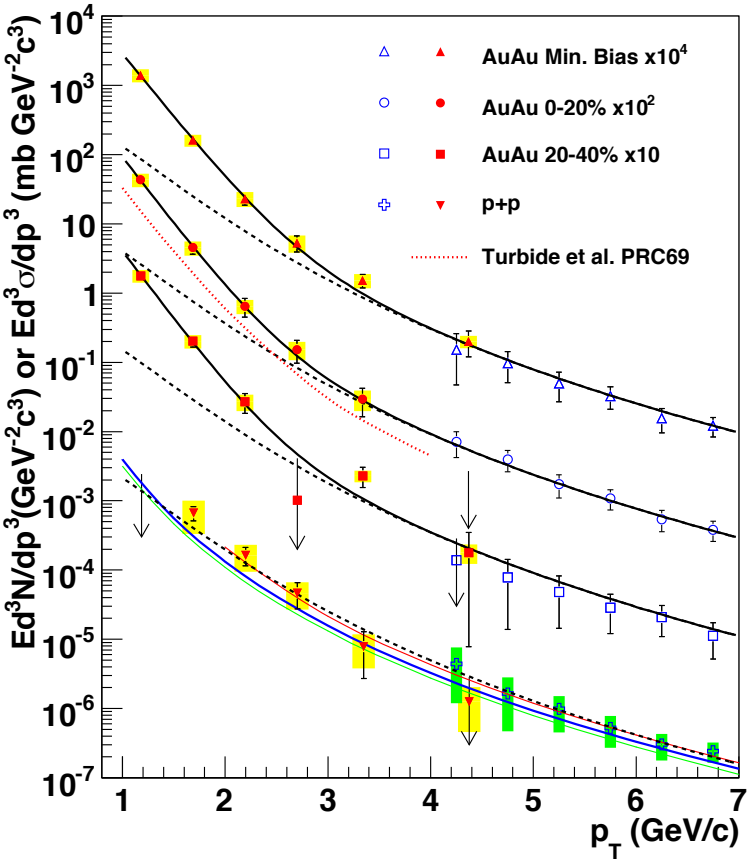

Figure 1.18: Direct photon spectra measured by the internal conversion method and the real photons in Au+Au collisions at $\sqrt{s_{NN}}$ =200 GeV reported by the PHENIX experiment [39]

mentum range. It is also successful that the method measures with a wide range of centrality compared to the virtual photon method. Therefore, the detailed production mechanisms of direct photons can be provided by the measurements.

The external conversion method is performed in Au+Au collisions at $\sqrt{s_{NN}} = 200$ GeV, and the results of the thermal photon spectra are shown in Fig. 1.19. The thermal photon spectra are calculated from the direct photon spectra by subtracting the scaled p+p results. The slopes of the spectra indicate the estimated effective temperature of the created matter. The effective temperatures are calculated from the fit by an exponential function

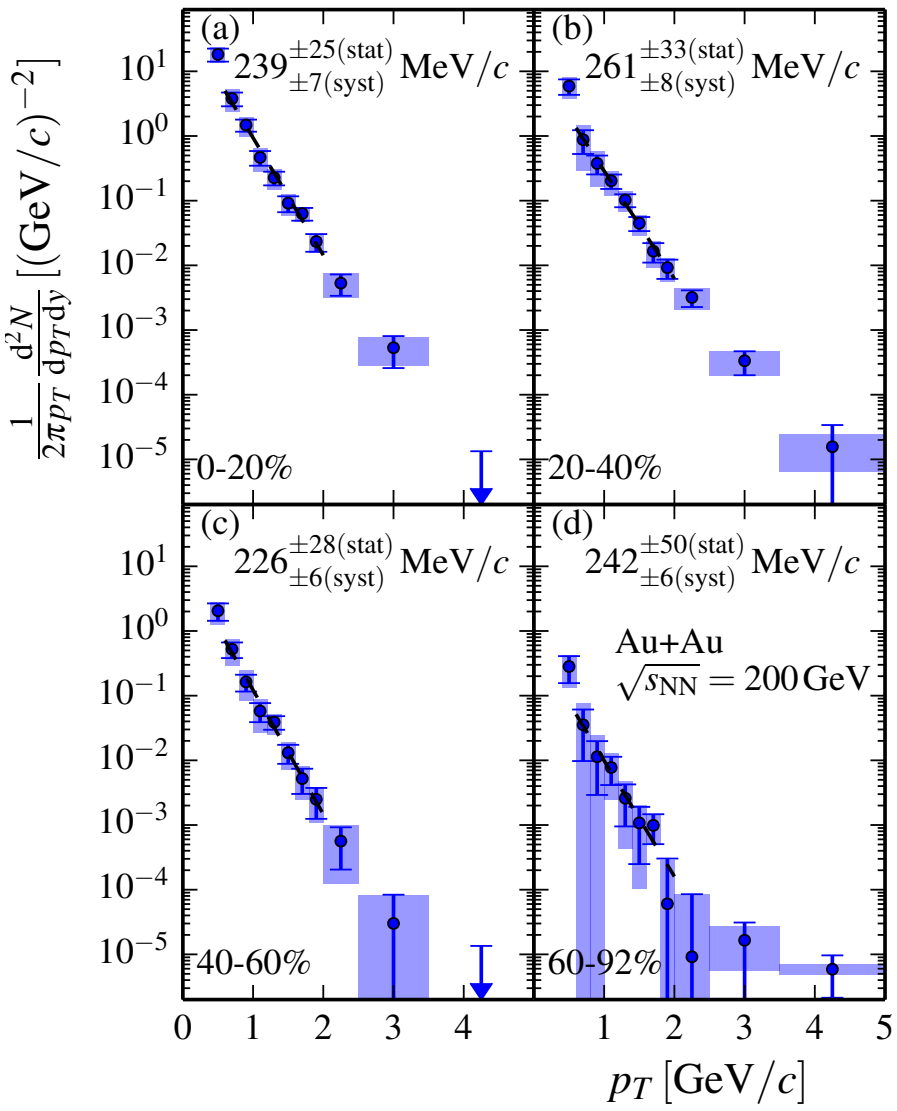

Figure 1.19: Thermal photon spectra by the external conversion method in Au+Au collisions at $\sqrt{s_{NN}}$ = 200 GeV, together with the exponential fit results. [42]

with the fit range $0.6 < p_T < 2.0$ GeV/c, and they are approximately 240 MeV/c independents of centrality. Figure 1.20 shows the integrated thermal photon yields as a function of the number of participants N_{part} for different

limits of lower transverse momentum integration. The $N_{\rm part}$ dependence of the integrated yields have the same power in the power-law function $AN_{\rm part}^{\alpha}$, and the average power results $\alpha = 1.38 \pm 0.03(\text{stat}) \pm 0.07(\text{syst})$.

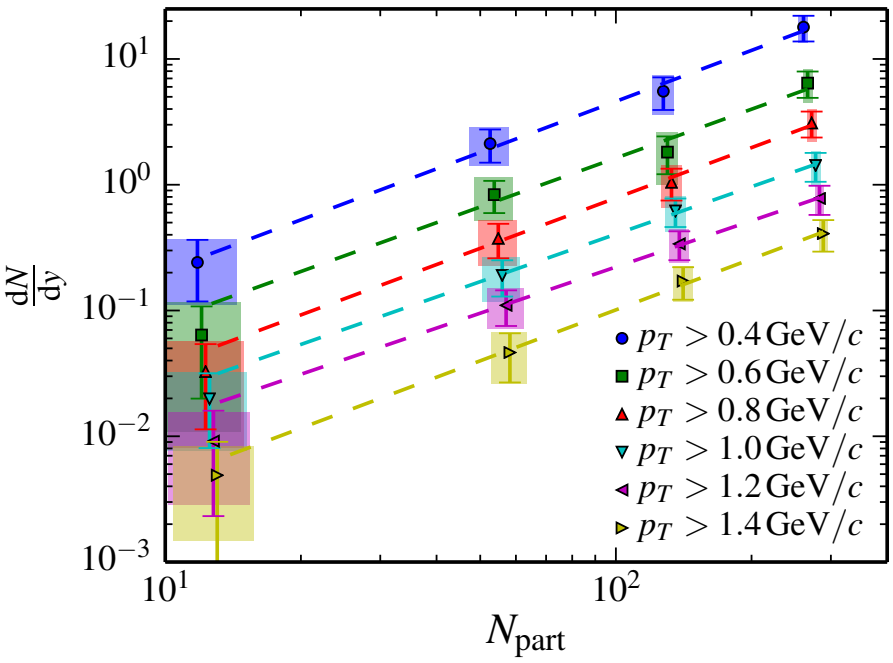

Figure 1.20: Integrated thermal photon yields for different lower transverse-momentum limit in Au+Au collisions at $\sqrt{s_{NN}} = 200$ GeV [42]

1.7.4 Collisions energy dependence of direct photons

Direct photons have also been measured in lower collision energies in the RHIC collider and higher collision energies in the LHC. RHIC provides the exploration of the QCD phase diagram with Beam Energy Scan (BES) in 2010 and 2011 as BES phase-1 [43]. The PHENIX experiment collected the Au+Au collision data at $\sqrt{s_{NN}} = 39$ and 62.4 GeV and reported direct photon production [44]. Besides, the LHC collider can provide higher collision energies than RHIC because it has a larger circumference, about 30 km. The ALICE experiment at the LHC reported the direct photon measurement in Pb+Pb collisions at $\sqrt{s_{NN}} = 2.76$ TeV [45].

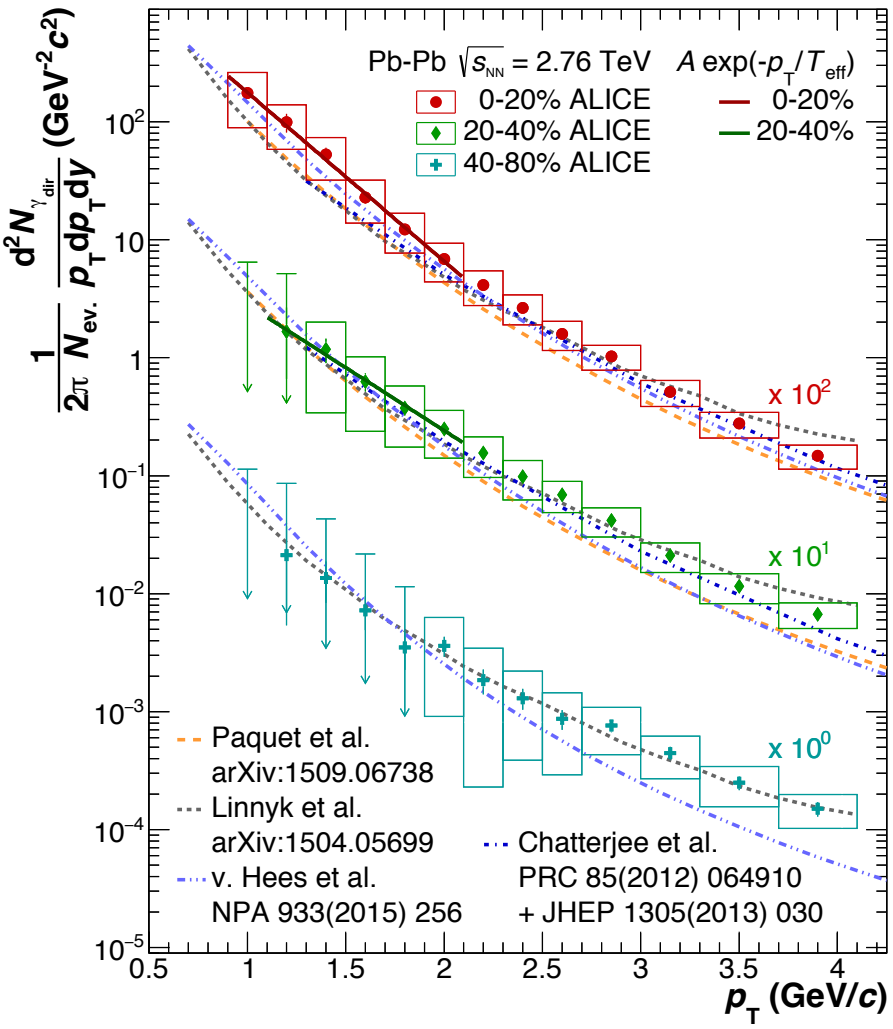

Figure 1.21: Direct photon spectra in Pb+Pb collisions at $\sqrt{s_{NN}} = 2.76$TeV measured by the ALICE experiment [45]. The spectra for three centrality classes, together with several theoretical models, are shown in the figure.

Figure 1.21 shows the direct photon spectra in Pb+Pb collisions at $\sqrt{s_{NN}} =$ 2.76 TeV. The spectra are measured in three centrality bins, and they are compared to several theoretical models from pQCD calculations with different parameterizations. The inverse slope of the exponential function gives the effective temperature, and the results are $T = 297$ MeV for 0–20% and

410 MeV for 20–40% centrality. The effective temperature measured in the LHC reaches higher than the RHIC collision energy of $\sqrt{s_{NN}} = 200$ GeV.

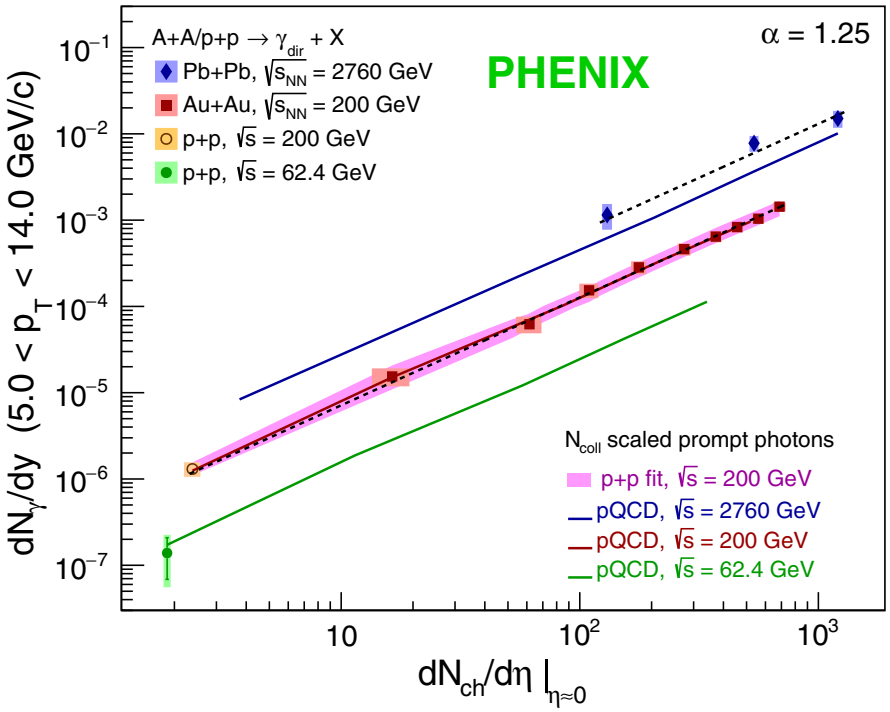

Figure 1.22: Integrated direct photon yields ($p_T > 5$ GeV/c) in several collision system together with pQCD calculations [44]

The integrated yields of direct photons are measured in several collision systems [44]. The integrated yield is calculated by the integral of the direct photon spectrum. Figure 1.22 shows the integrated yield as a function of $dN_{\rm ch}/d\eta$ in p+p, Au+Au, and Pb+Pb collisions. The yield dN_γ/dy has a scaling described as proportional to $(dN_{\rm ch}/d\eta)^\alpha$ with $\alpha \approx 1.25$. The integrated yields for several collision systems are compared to the expectation from pQCD calculations. The same scaling can describe the integrated yields for given collision energy, but an additional multiplicative factor is needed to explain the collision energy dependence.

1.7.5 Direct-photon collective flow

The elliptic flow of charged hadrons was first observed in Au+Au collisions at $\sqrt{s_{NN}}$ =130 GeV at the STAR experiment [14]. The elliptic flow is an asymmetry of the azimuthal distribution with respect to the reaction plane. The azimuthal anisotropy is supposed to be zero in the simple nucleus-nucleus collisions. However, the strong azimuthal anisotropy has been measured by experiments [15, 46, 47, 48]. Therefore, strong anisotropy is meant to be produced by particle interaction and space-time evolution. In the non-central collisions, the participant's shape is elliptical, and thus the shape leads to a pressure gradient. The particles inside the created matter move following the pressure gradient, and the matter expand over time. Relativistic viscous hydrodynamic calculations can describe the elliptic flow well [49, 50, 51]. The hydrodynamical calculations can describe the experimental results well. Comparing the experimental and theoretical results that the created medium behaves like a nearly perfect liquid [52]. The theoretical calculations suggest that the medium has early local thermalization [53].

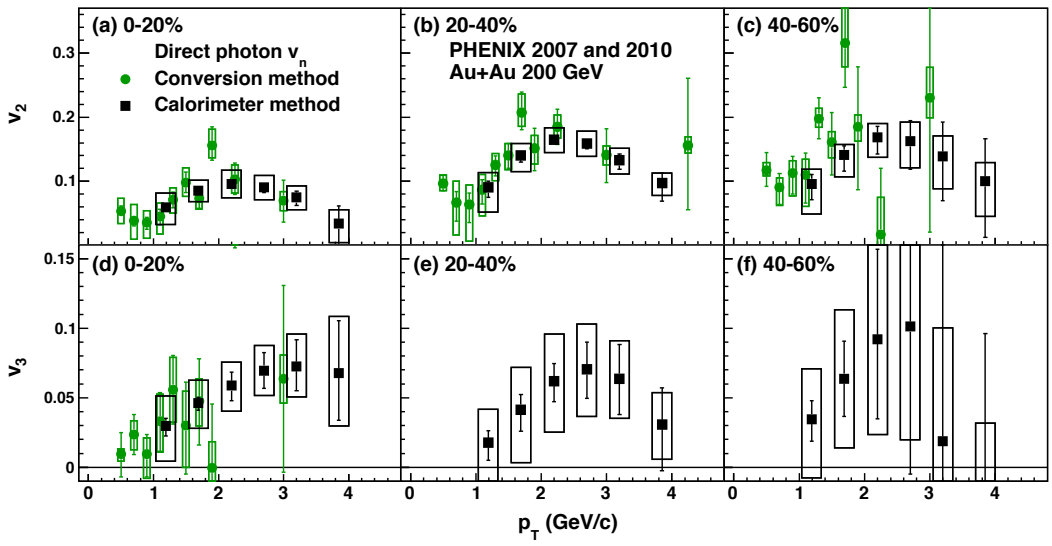

Figure 1.23: Direct photon elliptic flow v_2 and triangular flow v_3 in Au+Au collisions at $\sqrt{s_{NN}}$ = 200 GeV measured by the PHENIX experiment [54]

The PHENIX experiment reports the large azimuthal anisotropy for direct photons in Au+Au collisions at $\sqrt{s_{NN}}$ = 200 GeV [54, 55]. The mag-

nitude of the elliptic flow for direct photons is comparable to one observed for hadrons [56]. Figure 1.23 represents the results for the second and third-order Fourier components for several centralities in Au+Au collisions. Both measured Fourier components of direct photons are found to be of a large magnitude. The second-order Fourier coefficient has a centrality dependence, while the third-order Fourier coefficient has no centrality dependence. The ALICE experiment also reports the elliptic flow of inclusive and direct photon in Pb+Pb collisions at $\sqrt{s_{NN}} = 2760$ GeV [57]. The experiment measures the direct photon flow via the external conversion method, and the magnitude of the direct photon elliptic flow shows a similar to the PHENIX measurement.

1.7.6 Direct photon puzzle

Low transverse-momentum direct photons are expected to contain the thermal photons as a dominant contribution. The spectrum and yield of the direct photons are sensitive to the temperature. The slope of the spectrum is proportional to T_{eff}, and the yield is proportional to T^3. The azimuthal anisotropy has a sensitivity to the space-time evolution with collective motion. Therefore, direct photon measurements help us to understand the characteristics of the created matter and its evolution.

Figure 1.24 shows the results on the direct photon measurement of the yield and azimuthal anisotropy in Au+Au collisions at $\sqrt{s_{NN}} = 200$ GeV [54]. The direct photon spectrum measures the large yield of direct photons in the low transverse-momentum region. The result suggests that low momentum direct photons are emitted from the early stage, where the system temperature is high. The direst photon azimuthal anisotropy measures a large magnitude of v_2 comparable to hadron v_2. The v_2 result implies that low momentum direct photons are produced in the late stage, where the system collectivity is sufficiently built up.

Both experimental results are compared to several theoretical models simultaneously. The comparison shows a large deviation between the data and models in either the yield or anisotropies. Low momentum direct photons are thought to be dominantly contributed from thermal photons radiated by Quark-Gluon Plasma. However, theoretical models struggle to explain the direct photon production at the same time. This problem is called the direct photon puzzle.

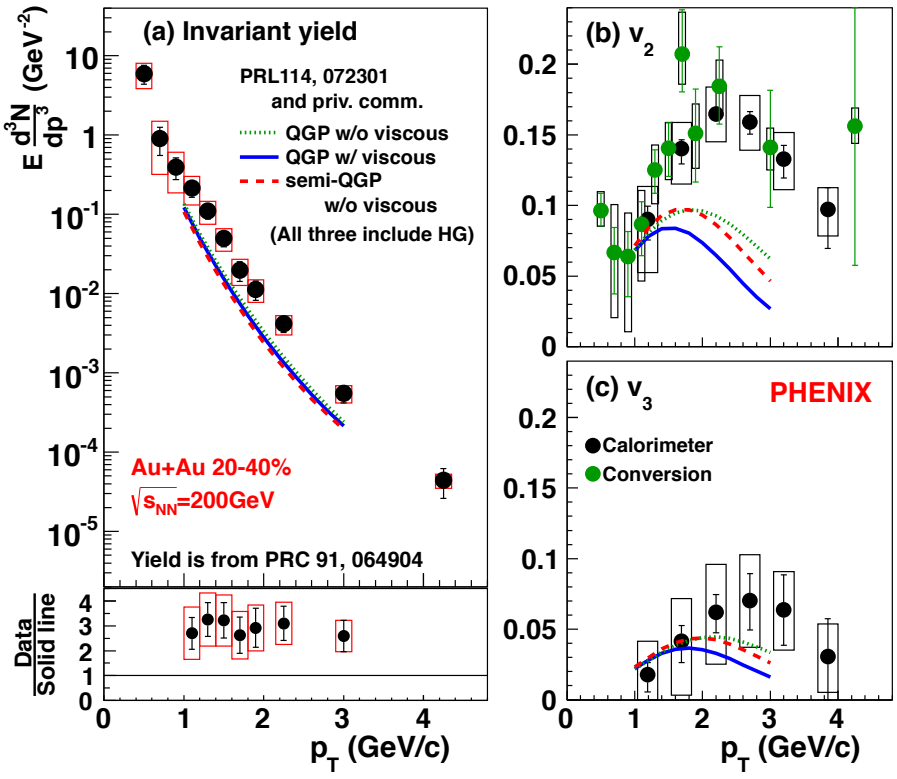

Figure 1.24: Direct photon spectrum and azimuthal anisotropies of the second and third Fourier components in Au+Au collisions at $\sqrt{s_{NN}} = 200$ GeV, together with several theoretical models. [54]

1.8 The thesis motivation

The thesis motivation is to study the production of low transverse-momentum direct-photons in ultra-relativistic heavy-ion collisions. Direct photons do not participate in the strong interaction; therefore, they are an excellent probe to study the properties and dynamics of the created matter. Direct photons are emitted in the entire stages of the collisions, and they carry pure information of the stage in which they were produced.

Direct photon production has been measured in various collision systems and energies in RHIC and the LHC experiments. The yields and anisotropy are measured, and the experimental results are compared to the theoretical models. However, any theoretical approaches do not exist to simultaneously

explain the observed data for both yields and anisotropies. The large thermal photon yield is expected to be produced at the early stage, whereas the large azimuthal anisotropy is supposed that the photons are originated in the later stage. The contradiction of the thermal photon production is known as "the direct photon puzzle".

The thesis presents the measurement of low transverse-momentum direct-photons in Cu+Cu collisions at $\sqrt{s_{NN}} = 200$ GeV. Direct photons are measured by the virtual photon method. The data was taken by the PHENIX experiment at the RHIC collider in Brookhaven National Laboratory. The PHENIX detector has an excellent ability to measure electrons and positrons with a wide range of transverse momentum.

Direct photon measurement in Cu+Cu collisions provides additional information on the collision system-size dependence of low transverse-momentum direct photon production. This thesis focuses on three centrality classes; minimum bias, 0–40% as central collisions, and 40–94% as peripheral collisions. These collisions are compatible with the Au+Au peripheral collisions.

We extract the virtual photon contribution as an excess over the known hadron decay contributions in the invariant mass distribution. The extracted contribution, the direct photon fraction, is converted into the direct photon spectra. The measured spectra for three centrality classes are compared to the Au+Au results, and the effective temperature is calculated from the inverse slope of the spectra. The direct photon rapidity density is also investigated as a function of the number of participants, $N_{\rm part}$. The Cu+Cu results provide the system-size dependence of the production, and we discuss the collision system dependence of the direct photon production.

The structure of this thesis is as follows. Chapter 2 describes the introduction of the experimental setup. Chapter 3 expresses the analysis method for direct photon measurement via virtual photons, including subtracting a large amount of background and signal extraction. The next chapter, Chapter 4, shows the measurement results, including the discussion about the direct photon spectra and rapidity density compared to results in other collision systems. Finally, Chapter 5 gives the conclusion of the thesis.

Chapter 2

Experimental setup

We measured nucleus-nucleus collisions by the Pioneering High Energy Nuclear Interactions eXperiment (PHENIX) at the Relativistic Heavy Ion Collider (RHIC) at Brookhaven National Laboratory (BNL). In this chapter, we introduce an overview of the RHIC complex and the PHENIX detector.

2.1 Relativistic Heavy Ion Collider

The Relativistic Heavy Ion Collider (RHIC) locates at Brookhaven National Laboratory (BNL) in Long Island, New York, the United States. The purpose of the collider experiment is to discover a new high-temperature and high-density matter and research the characteristics of the QGP state in ultra-relativistic nucleus-nucleus collisions.

RHIC can accelerate and collide various nuclei from light ions, protons to heavy ions, uranium. The maximum energy at RHIC is up to 100 GeV per nucleon for copper and gold, and that of a proton is 250 GeV. The collision energy of RHIC is one order of magnitude higher than that of the Alternating Gradient Synchrotron (AGS) at BNL and the Super Proton Synchrotron (SPS) at CERN.

Figure 2.1 shows the RHIC complex arrangement, including four experiments and pre-accelerators. The RHIC collider comprises two individual superconducting rings of 3.8 km in circumference, one for the clockwise ring, the Blue ring, the other for counter-clockwise, the Yellow ring. These two rings intersect at six points, and the four experimental facilities, PHENIX, STAR, BRAHMS, and PHOBOS, are initially located at each one of the in-

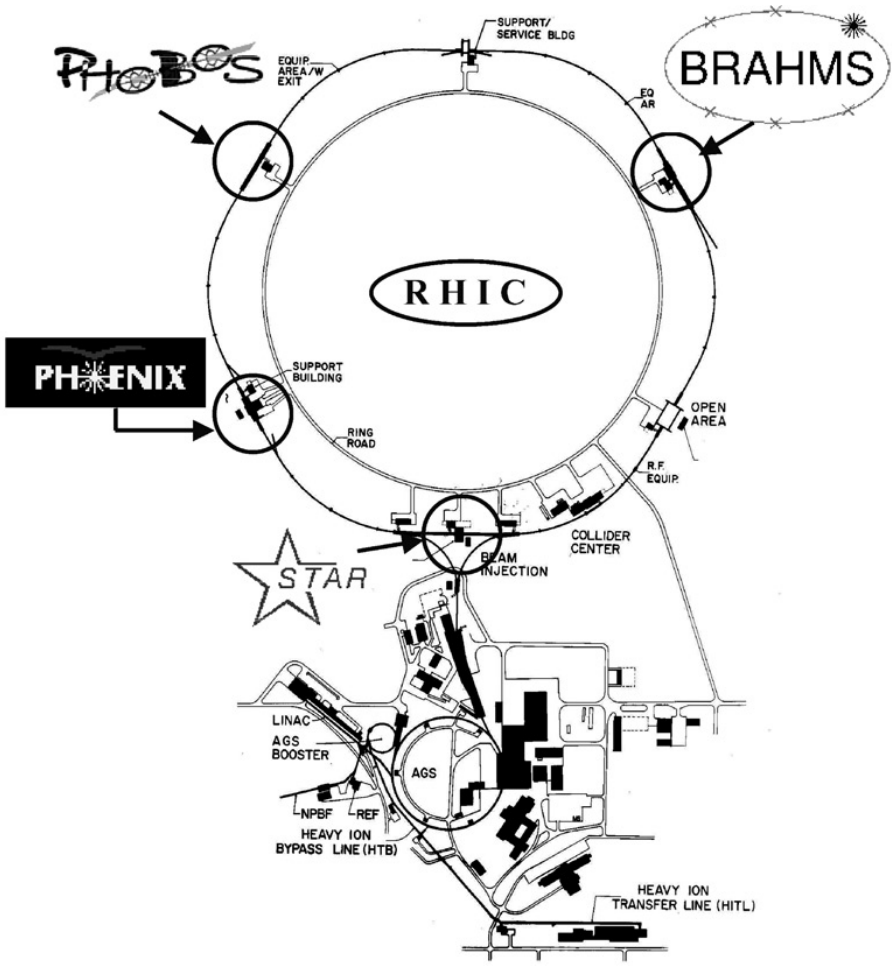

Figure 2.1: Relativistic Heavy Ion Collider (RHIC) complex arrangement, including the LINAC and the Tandem Van de Graaff as a pre-accelerator, and the Alternating Gradient Synchrotron (AGS). [58]

tersection points. Clock positions enumerate the points; the PHENIX facility locates at 8 o'clock and the STAR facility at 6 o'clock.

The LINAC and the Tandem Van de Graaff are the source of the ions and pre-accelerator for protons and heavy ions such as copper and gold, respectively. The injected atoms are partially stripped of electrons, and the accelerated ions send to the Booster Synchrotron. The ion beam is stripped again and reaches 37 % of the speed of light. After the booster, the ion beams

are injected into Alternating Gradient Synchrotron. The AGS accelerates the beams up to 28 GeV for proton and 10.8 GeV per nucleon for heavy ions. After that, the ion beams are delivered to RHIC through the AGS-to-RHIC Beam Transfer Line with stripping of electrons at the AGS exit. Finally, the beams are accelerated and stored in RHIC.

2.2 The PHENIX detector

The Pioneering High Energy Nuclear Interactions eXperiment (PHENIX) is designed to measure several fundamental probes in heavy-ion collisions, especially electromagnetic probes [59]. The PHENIX detector comprises three detector systems: the global detectors, the central arm spectrometers, and the muon arm spectrometers. Figure 2.2 shows the detector configuration on both the beam and side views in 2005. The PHENIX detector has an excellent particle identification capability in a broad transverse momentum range to measure photons, leptons, and hadrons simultaneously. The central arms placed on the east and west sides dedicate themselves to measure photons, electrons, and hadrons, whereas the muon arms located on both the north and south sides give muon measurements. Besides, the global detectors measure the start timing, collision vertex, centrality, and reaction plane. The central arms are employed in this study to measure low transverse-momentum direct photons, and it covers pseudo-rapidity, η, with ± 0.35 and azimuth with 90 degrees. In the following sections, we describe the details of the PHENIX detectors focusing on related to the thesis.

2.3 Global detectors

The global detectors characterize the collision events by measuring the collision vertex, particle multiplicity related to the centrality, and reaction plane. Once the collision occurs, the global detectors determine the start timing for time-of-flight measurement and give the start signal to spectrometers. The PHENIX experiment has two global detectors, the Beam-Beam Counters inside the central arm and the Zero-Degree-Counter located far from the detector center.

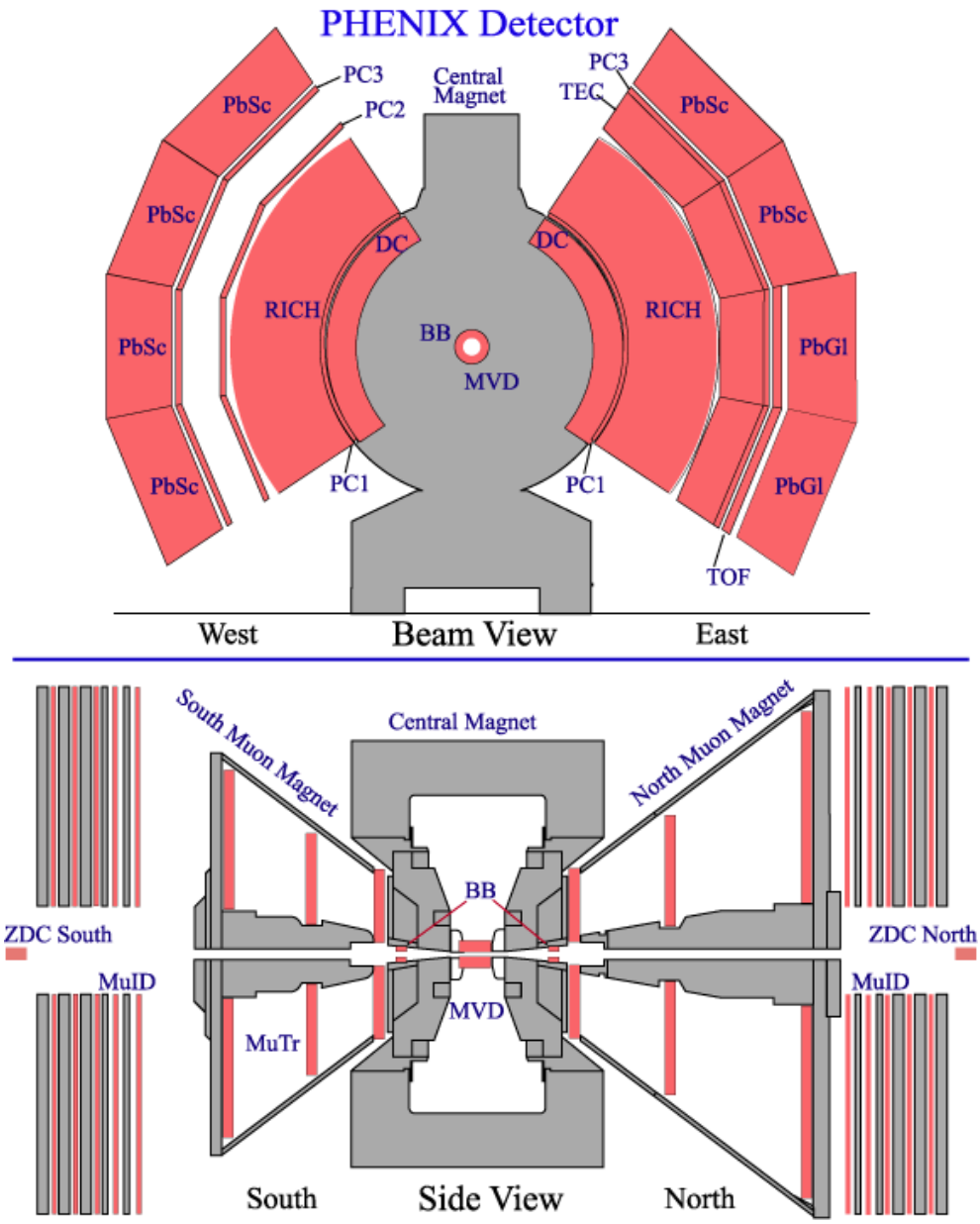

Figure 2.2: The configuration of the PHENIX detector in 2005. The drawing shows the beam view (Top) and side view (Bottom) of the detector. [60]

2.3.1 Beam-Beam Counters

The Beam-Beam Counters (BBCs) are a pair of Cherenkov detectors located on the north and south sides around the beam pipe at a distance of ± 144.35 cm from the nominal interaction point [61, 62]. Each of the BBC comprises 64 elements of a mesh-dynode type photomultiplier tube (PMT) with a quartz Cherenkov radiator. The BBC detector covers the range of 3.1< $|\eta|$ <3.9 in pseudo-rapidity and full azimuthal angle ($\Delta\phi = 2\pi$).

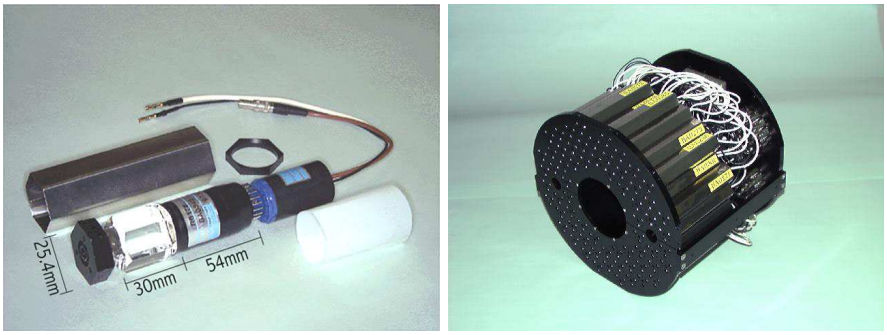

(a) **(b)**

Figure 2.3: The BBC detector. (a) shows a BBC element, a photomultiplier. (b) shows a BBC array. [63]

BBC has four essential roles: to trigger the PHENIX Minimum-Bias events, to determine collision vertex, centrality, and reaction plane. Besides, BBC measures the collision timing for the time-of-flight measurement together with the Time-of-Flight detector.

The BBCs determine the collision vertex and timing by the difference and average of hit time between the north and south side counters. The vertex z_{vtx} and the start timing t_0 are calculated by the following equations;

$$z_{vtx} = \frac{T_{\mathrm{South}} - T_{\mathrm{North}}}{2} \times c \tag{2.1}$$

$$t_0 = \frac{T_{\mathrm{South}} + T_{\mathrm{North}} - (2 \times L/c)}{2} \tag{2.2}$$

where L is the known distance from the center of the PHENIX detector to the BBC detector position, 144.35 cm, and c is the speed of light.

The collision centrality is measured by the BBC multiplicity along with the ZDC deposit energy, and the reaction plane is determined by the azimuthal distribution of the measured particles in the BBC described in detail in Sections 3.2.3 and 3.2.4, respectively.

2.3.2 Zero-Degree Counters

The Zero-Degree Counters (ZDCs) are a pair of hadron calorimeters located at a distance of 18 m downstream of the PHENIX north and south sides [64]. The ZDCs measure the energy of spectator neutrons, which does not participate in the collision interactions. Besides, the detectors are standard equipment in all experiments in the RHIC collider. Figure 2.4 shows the cutaway view related to the ZDC detectors. The Dipole Magnets are installed between the interaction point and the ZDC. Therefore, the charged particles in the spectators are deflected by the magnet, and the neutral particles, neutrons, only hit the ZDC and deposit the energies. The ZDC detectors provide the centrality determination.

2.4 The central arm detectors

The PHENIX Central Arms locates on the west and east sides. Each arm covers the pseudo-rapidity and azimuthal angle ranges of $|\eta| < 0.35$ and $|\phi| < \pi/2$, respectively. Several detectors are installed in the central arms to measure electrons, photons, and hadrons. The Drift Chambers (DCs) and Pad Chambers (PCs) determine the charged particle trajectories and measure their momenta. The electric charge signs of the particles are identified by the trajectory curvatures. The Ring Imaging Cherenkov counter (RICH) provides electron identification by energy-momentum matching. Electromagnetic calorimeters (EMCals) consists of eight separate sectors: two sectors located in the bottom of the east arm are lead-glass (PbGl), the other six sectors are lead-scintillator (PbSc). In the following subsections, we describe the detectors used in this study.

2.4.1 The Central Magnet

The PHENIX Central Magnet is comprised of the Central Magnet and the Muon Magnets [66]. The Central Magnet provides the magnetic field around

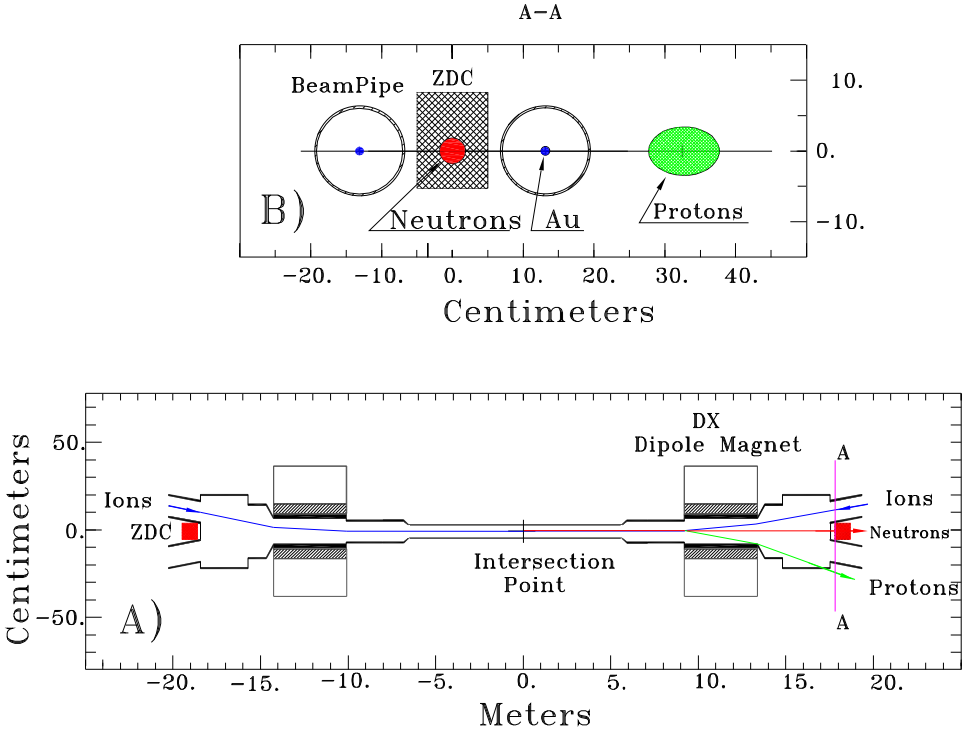

Figure 2.4: The cut-away view of the zero degree calorimeters. [64]

the collision vertex point, while the Muon Magnets provide the magnetic field for the forward and backward region of the PHENIX detector. The Central Magnet is used for charged particle measurement by the central arm detectors. The Central Magnet consists of two pairs of concentric Helmholtz coils; the inner and outer pair. The inner coils provide a magnetic field around the interaction point parallel to the beam direction with axial symmetry. In this thesis, electrons and positrons are measured by the central arm detectors, and they follow a curved path in the magnetic field. The Muon Magnets are utilized for muon measurement by the muon spectrometers.

Figure 2.5 shows a cut-away view for the PHENIX Central and Muon Magnets and their magnetic field lines in (++) configuration. The Helmholz coil can be operated with the same (++) or opposite (+−) polarity. The data we use in this study is collected with the same polarity configuration.

The coverage of the magnetic field is $70^\circ < \theta < 110^\circ$ and $|\eta| < 0.35$. The provided magnetic field allows charged particle tracking and momentum

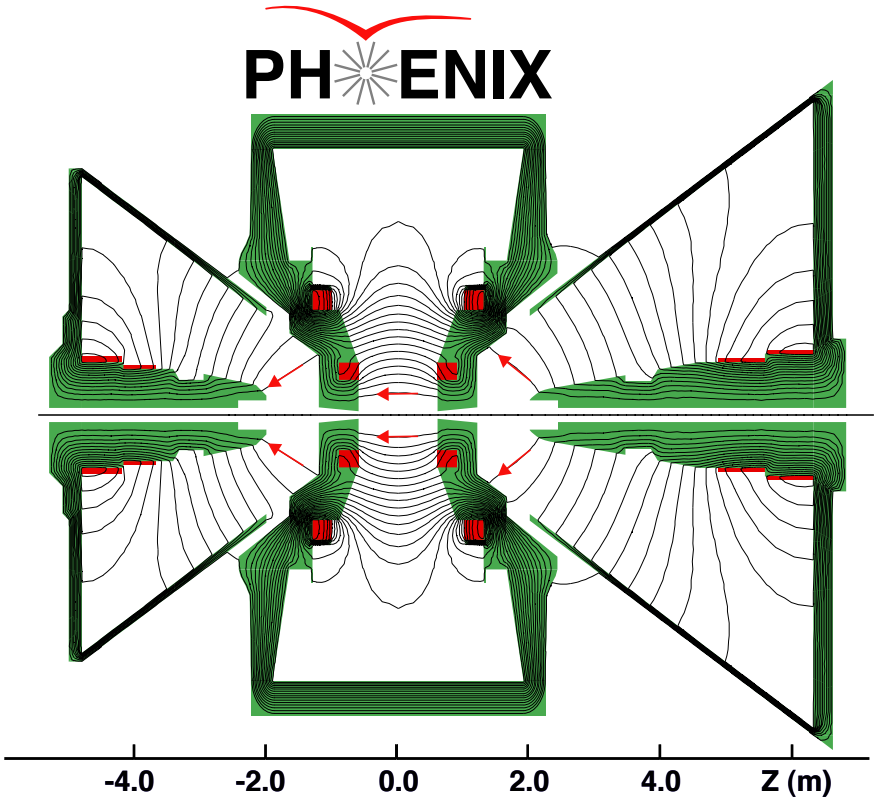

Figure 2.5: The PHENIX Central Magnet [65]

analysis. The magnitude of the magnetic field at R =0 cm is 0.5T, and it gradually decreases with approximately the Gaussian profile to zero at R > 250 cm. Then, charged particles pass straight through in the RICH detector due to the magnetic field's no effect.

2.4.2 Drift Chamber

The Drift Chambers (DCs) is the primary tracking detector in the PHENIX experiment for measuring charged particle trajectories [67]. The DCs are located between 2.02 and 2.48 meters in radius from the beam axis. The Drift Chamber is a cylindrical shape with the coverage of $|z| < 90$ cm and $\pi/2$ azimuthal angle.

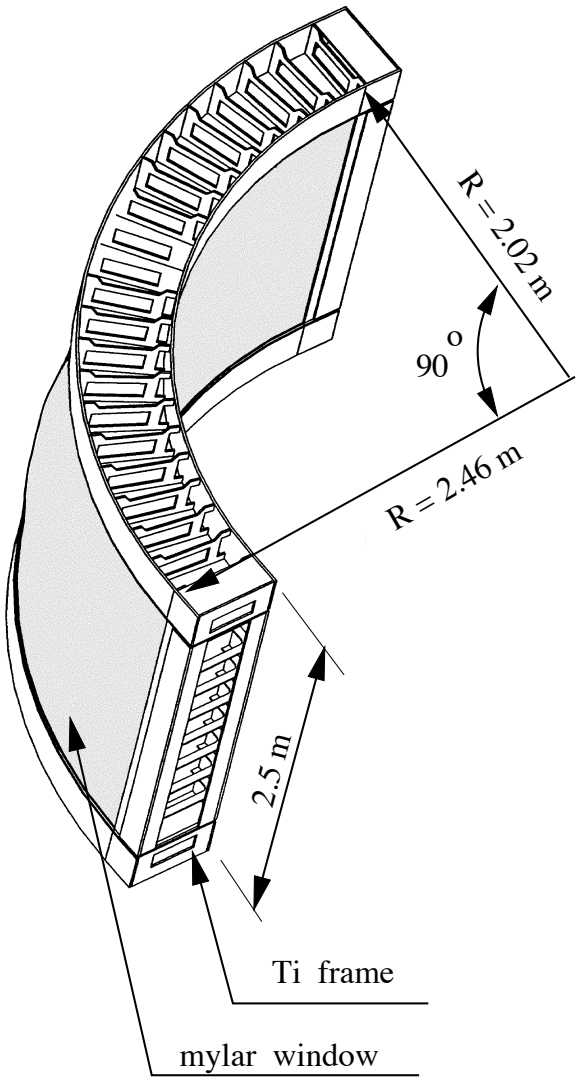

Figure 2.6: The construction of Drift chamber frame [67]

The inside of the DCs has filled a mixture gas of 50% Algon, 50% Ethane, and a small fraction of alcohol. The mixture gas randomly ionizes when the charged particles pass through. The ionized electrons from the primary ionization process are drifted towards an anode wire in an electrical field. The charged particle trajectories are reconstructed by hits in subsequent anodes.

Figure 2.7 shows a schematic view of a Drift Chamber. Mylar windows

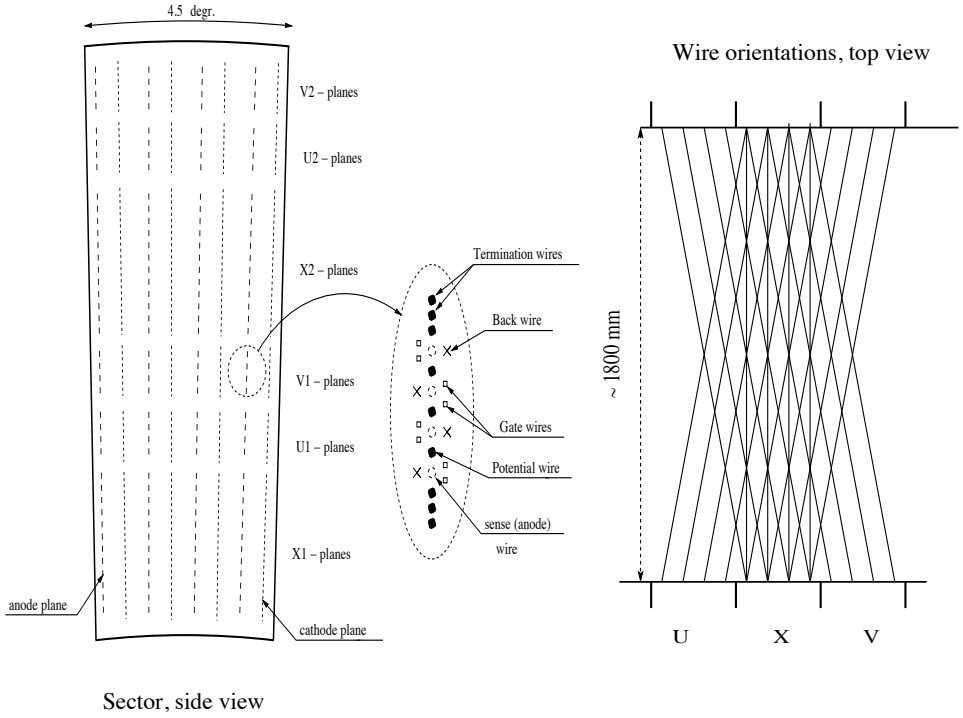

Figure 2.7: The wire position and the stereo wire orientation in Drift Chamber. Left: the wire position layout within one sector and inside the anode plane. Right: a schematic diagram of the stereo wire orientation. [67]

and titanium support frames enclose the drift zone of the gas-filled region. The DC is consists of 20 sectors covering 4.5 degrees in azimuth.

The Drift Chamber with the help of the Pad Chamber measures the trajectories for charged particles, and it determines transverse momentum down to 200 MeV/c. The curvature of the track determines the momentum since the curvature is in inverse proportion to the momentum.

2.4.3 Pad Chamber

The Pad Chambers (PCs) are multi-wire proportional chambers consisting of three individual layers, PC1, PC2, and PC3 [67]. Each PC has a single wire plane inside a gas volume bounded by two cathode planes. The PCs are operated with a mixed gas of 50% argon and 50% ethane. The PC1 is the

innermost layer between the DC and the RICH in both the East and the West arms. The PC2 is the middle layer installed behind the RICH only in the West arm. The PC3 is the outermost layer in front of the Electro-Magnetic Calorimeter (EMCal) in both arms.

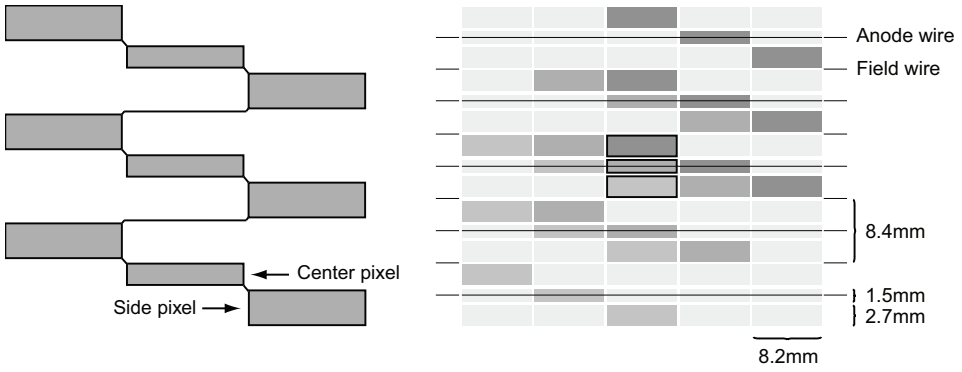

Figure 2.8: Left: The pad and pixel geometry. Right: Pad design [67]

The system of PCs provides three-dimensional space-points of charged particles outside the magnetic field. The PC1 also provide z-coordinate at the exit of the DCs that is essential for determining three-dimensional vector momentum of charged particles. The PC2 and PC3 are used to reject many background tracks produced by particle decays and particle-detector interactions outside the aperture of the DC.

2.4.4 Ring Imaging Cherenkov Counters

A Ring Imaging Cherenkov Counters (RICH) is a gas Cherenkov detector as a primary device to identify electrons and positrons among a large amount of charged pions in the PHENIX experiment [68]. The RICH is installed between the PC1 and PC2 in both the east and west arms.

The principle of Cherenkov detectors is that a charged particle traveling in a medium with a velocity βc emits the Cherenkov radiation with the angle $\cos\theta_c = 1/(n\beta)$ because the velocity is greater than the speed of light in that medium. The threshold of Cherenkov radiation for pions are at about 4.9 GeV/c, while electrons are at about 0.02 GeV/c. Therefore the RICH provides e/π discrimination below the pion threshold and a hadron rejection ratio of 10^4 to 1 below the threshold.

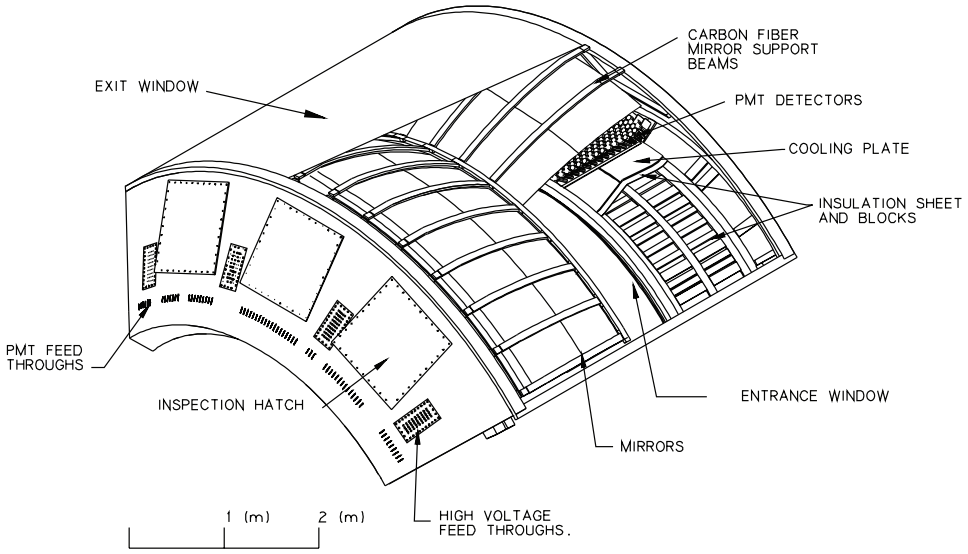

Figure 2.9: A cutaway view of one arm of the PHENIX RICH detector [68]

The schematic view of the RICH is shown in Fig. 2.9. The RICH is consists of three parts: a gas vessel, reflective mirrors, and photomultiplier tubes. The CO_2 gas as radiator gas is filled in 40 m^3 vessel between the entrance and exit windows. The 48 composite mirrors forming two intersecting spherical surfaces focus the Cherenkov ring onto the photomultiplier tubes with a total reflecting area of 20 m^2. One thousand two hundred eighty photomultiplier tubes are installed in two arrays located behind the central magnet; therefore, the particles originated from the collisions do not directly hit the tubes.

2.4.5 Electro-Magnetic Calorimeter

The Electro-Magnetic Calorimeter (EMCal) measures the spatial position and energy of electrons and photons [69]. Electrons and photons lose their energy in matter predominantly via Bremsstrahlung and electron pair production, respectively. The radiation length X_0 is defined as the length of the electron's energy reduced to 1/e.

The PHENIX EMCal is located at the most outside of the central arms covering the range of $70^\circ \leq \theta \leq 110^\circ$ subtending 90° in azimuth angle for

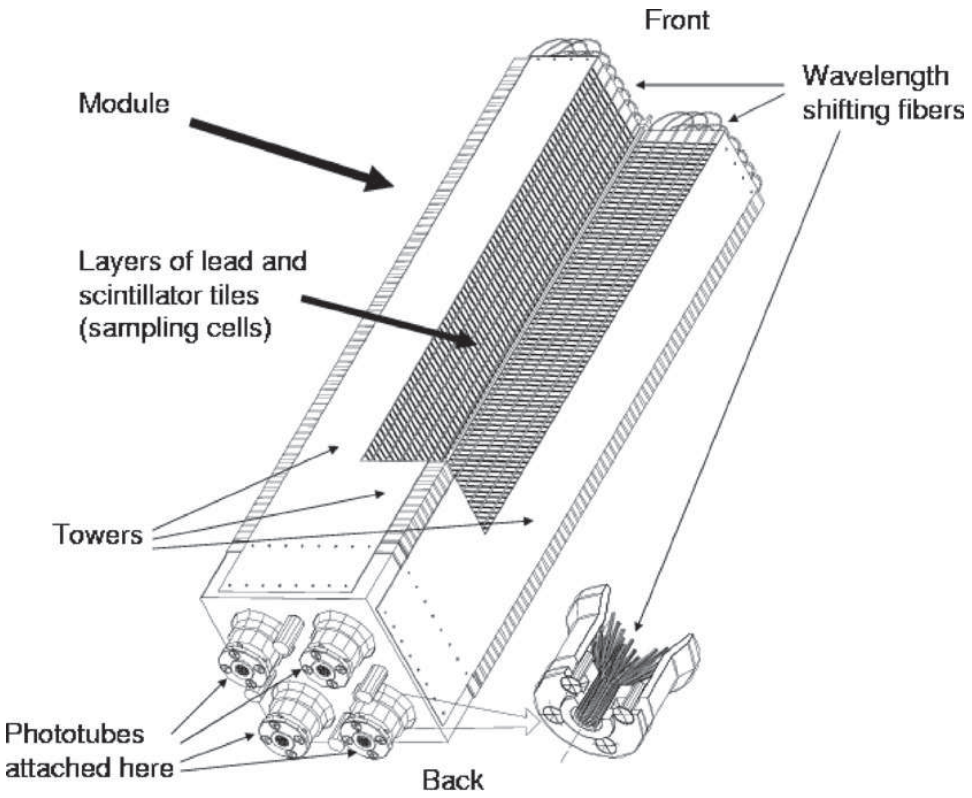

Figure 2.10: Interior view of a Pb-scintillator calorimeter module showing a stack of scintillator and lead plates, wavelength shifting fiber readout and leaky fiber inserted in the central hole. [69]

each arm. The PHENIX EMCal is installed in both east and west arms, and each arm comprises four sectors. In the east arm, the two top sectors are installed lead-scintillator calorimeter (PbSc), while the two bottom sectors are a lead-glass calorimeter (PbGl). In the west arm, all four sectors are lead-scintillator calorimeter.

The lead-scintillator calorimeter (PbSc) is a shashlik type sampling calorimeter. The PbSc calorimeter contains 15,552 individual towers, and each tower is made of 66 sampling cells with $18X_0$ and about 30 mm of Moliere radius. A module containing four towers is shown in Fig. 2.10. These four towers are optically isolated and connected to the wavelength shifting fiber. The photomultipliers are located on the backside of the tower. The energy and

position resolutions of the PbSc calorimeters are as follows, respectively.

$$\frac{\sigma_E}{E} = \frac{8.1\%}{\sqrt{E\,(\mathrm{GeV})}} \oplus 2.1\% \tag{2.3}$$

$$\sigma_x^{\mathrm{PbSc}}\,(E,\theta) = \left(1.55(\mathrm{mm}) \oplus \frac{5.7(\mathrm{mm})}{\sqrt{E\,(\mathrm{GeV})}}\right) \oplus \Delta \times \sin(\theta) \tag{2.4}$$

where θ is an impact angle of particle, and Δ is given by radiation length.

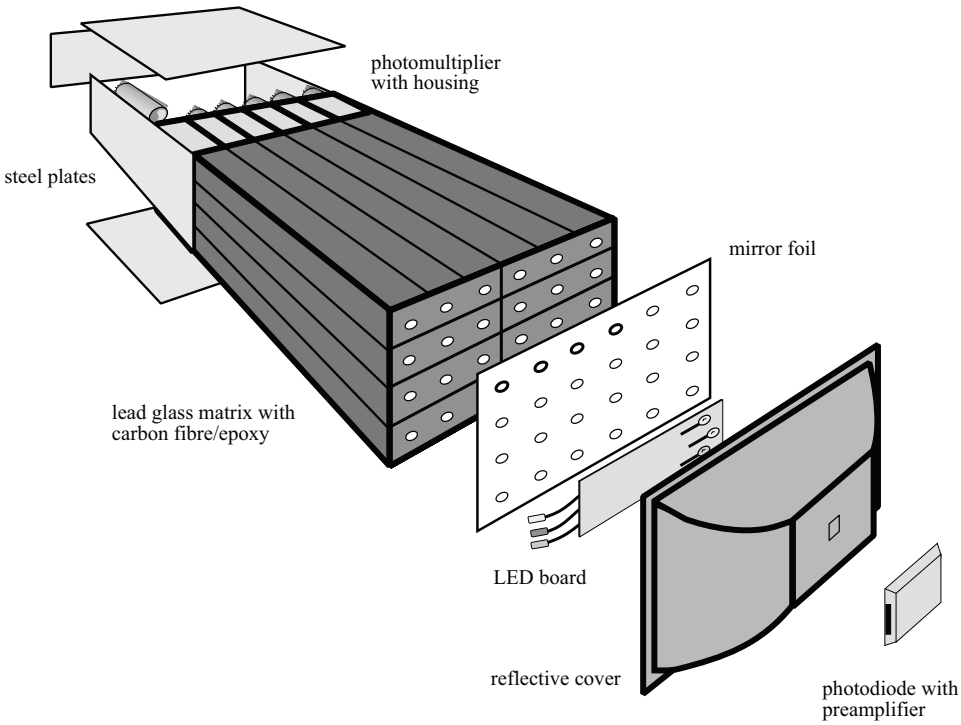

Figure 2.11: Exploded view of a lead-glass detector supermodule. [69]

The lead-glass calorimeter (PbGl) is a Cherenkov calorimeter which had been previously used in the WA98 experiment at the SPS collider at the CERN. The PbGl calorimeter contains 192 supermodules, and each supermodule consists of 24 modules. Figure 2.11 is shown the PbGl supermodule made of 6×4 modules. The module has $14.4X_0$ and 36 mm of Moliere radius and are individually wrapped with aluminized mylar foil to be optically

isolated. The energy and position resolutions of the PbGl calorimeters are obtained by the followings, respectively.

$$\frac{\sigma_E}{E} = \frac{5.9\%}{\sqrt{E\,(\mathrm{GeV})}} \oplus 0.8\%. \tag{2.5}$$

$$\sigma_x^{\mathrm{PbGl}}(E) = 0.2(\mathrm{mm}) \oplus \frac{8.4(\mathrm{mm})}{\sqrt{E\,(\mathrm{GeV})}} \tag{2.6}$$

2.5 Data Acquisition System

The overview of the Data Acquisition System (DAQ) in the PHENIX experiment is described in this section [70, 71]. The expected interaction rate provided by the RHIC collider varies from a few kHz for central Au+Au collisions to a few hundred kHz for p+p collisions. Furthermore, several hundred particles are passed through the detector in central Au+Au collisions, while a few particles in p+p collisions. The measured particles include various observables: hadrons, leptons, and photons. Therefore, the PHENIX DAQ is designed to handle various event sizes and rate seamlessly.

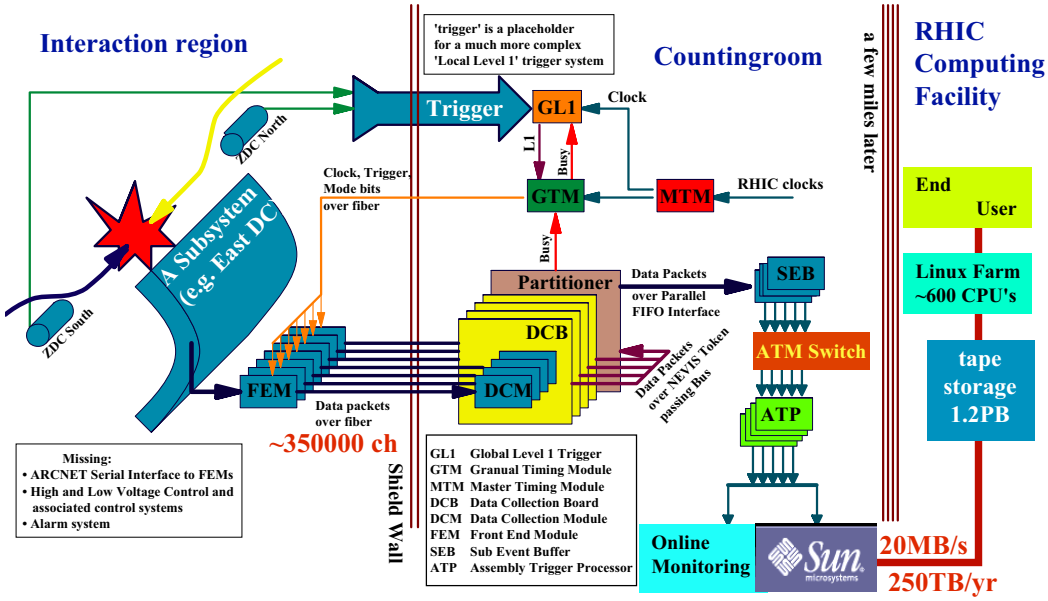

Figure 2.12: Schematic diagram of the PHENIX on-line system [71]

Figure 2.12 shows a schematic diagram of the PHENIX DAQ. The RHIC derivers the beam with the 9.4 MHz fundamental clocks corresponding to 106 ns of the time interval between beam crossing. All PHENIX Front-End Electronics Modules (FEMs) are synchronized to the RHIC clock. The RICH clocks are received by the Master Timing Module (MTM), and the master timings are transmitted to the FEMs via the Granual Timing Module (GTM). The FEMs are placed in the PHENIX Intersection Region (IR), and they convert the analog signals from the detectors into digital data. The Level-1 Trigger (LVL1) selects interesting events and rejects events due to limited DAQ rates. The LVL1 is triggered based on the logical combination of the Local Level-1 decisions generated by the trigger detector, such as the BBC and ZDC detectors. Once the LVL1 decision is generated, the FEMs transfer the buffered data to the Data Collection Module (DCM) located at the PHENIX Counting House. The data packets are sent to the Sub Event Buffers (SEB). Then they are transferred to the PHENIX Online Control System (ONCS) for online monitoring and logging and to the High-Performance Storage System (HPSS) at RHIC Computing Facility (RCF) for physics analysis.

Chapter 3

Analysis

This chapter describes the analysis for low transverse-momentum direct-photon measurement in Cu+Cu collisions at $\sqrt{s_{NN}} = 200$ GeV with the PHENIX experiment. We explain the analysis, including background reproductions, signal extraction, and estimation of the systematic uncertainties.

3.1 Overview

The PHENIX experiment collects the Cu+Cu collision data with a minimum bias trigger in 2005, the Run-5 of the RHIC operation. Low transverse-momentum direct photons are measured by the virtual photon method because the signal-to-background ratio can be improved compared to the real photon measurement. A virtual photon decay into an electron-positron pair. Accordingly, the virtual photon method measures e^+e^- pairs. The direct virtual photon contribution is statistically extracted as the remainder of the e^+e^- invariant mass distribution after subtracting extensive backgrounds and known hadronic contributions. The background contributions are evaluated from both well-tuned Monte Carlo simulations and the experimental data. Once the direct photon contribution is extracted, the direct photon spectra and the rapidity density are calculated.

Section 3.2 describes the data set used in this analysis. The event trigger and global variables for characterizing the collision events are explained. Sections 3.3 and 3.4 express the charged particle tracking and electron identification by the PHENIX central arm detectors, respectively. Section 3.5 explains the extraction of electron pairs. Section 3.7 shows the tuning for

the Monte Carlo simulations used for the background estimation. Sections 3.8 to 3.14 describe the background estimations and their subtraction. Section 3.15 describes the extraction of the direct photon fraction. At last, we describe the evaluation of systematic uncertainties in Section 3.16.

3.2 Event selection and global variables

3.2.1 Collected data and data set

The data of Cu+Cu collisions at the center-of-mass energy per nucleon pair of 200 GeV, $\sqrt{s_{NN}} = 200$ GeV, is taken in the PHENIX experiment at the RHIC collider in the year 2005. The collision system of Cu+Cu at $\sqrt{s_{NN}} =$ 200 GeV is only taken in 2005 at RHIC. This analysis is based on a minimum bias sample of 4.95×10^8 collision events with the z-vertex within 25 cm of the nominal interaction point equivalent to 0.44 nb^{-1}.

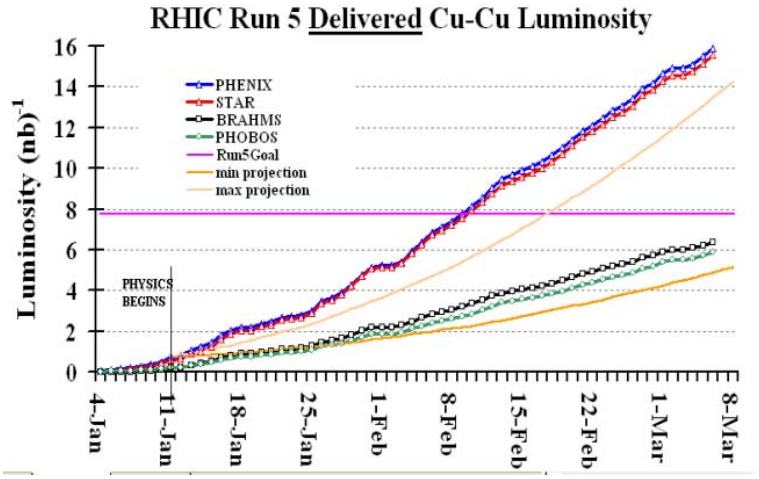

Figure 3.1: RHIC delivered Luminosity in Run-5 for Cu+Cu collisions at $\sqrt{s_{NN}}$ =200GeV [72]

3.2.2 Minimum Bias Trigger

The minimum bias trigger is defined by a signal coincidence of both the BBC and ZDC detector signals. The BBC has a sensitivity to both particles

from inelastic collisions and backgrounds from beam-gas and upstream interactions. At the same time, the ZDC is sensitive to inclusive interactions, including inelastic collisions and Coulomb dissociations. Therefore, requiring the coincidence can reduce the backgrounds.

3.2.3 Centrality determination

Centrality is an experimental variable in heavy ion collisions related to the impact parameter. Two heavy-ions collide with the impact parameter b shown in Fig. 1.5. The impact parameter describes the geometry of the collisions. However, the parameter can not be measured in experiments. Consequently, to characterize the collision geometry, the centrality is defined by corresponding the BBC multiplicity and the ZDC energy deposit.

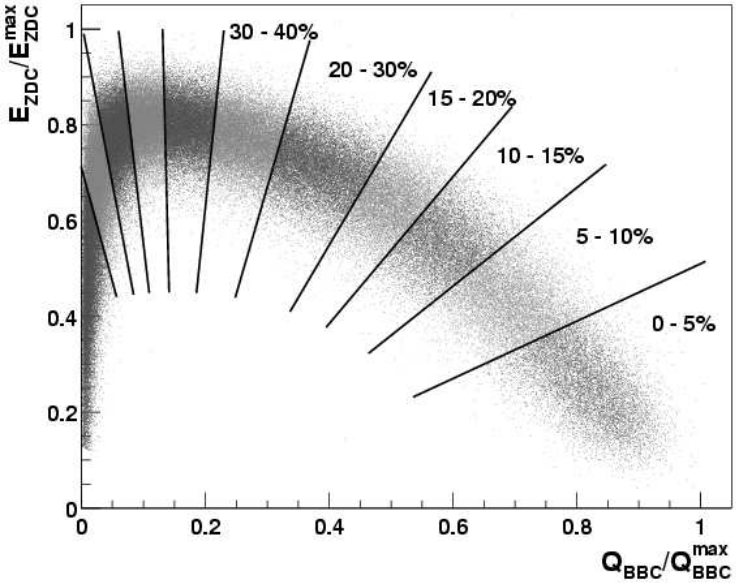

Figure 3.2: The correlation between BBC multiplicity and and ZDC energy deposit to determine centrality in the PHENIC experiment [73]

Figure 3.2 shows the correlation between the BBC multiplicity and ZDC energy deposit representing centrality boundaries. The multiplicity measured by the BBC increases proportionally to the number of participants, N_{part}, while the deposit energy in ZDC decreases. Therefore, the anti-correlation

appears between the BBC and ZDC measurements. The boundary of the centrality is determined by the clock method expressed as

$$\phi_{\text{centrality}} = \tan^{-1}\left(\frac{(Q_{\text{BBC}-Q_0}/Q^{\text{max}}_{\text{BBC}})}{E_{\text{ZDC}}/E^{\text{max}}_{\text{ZDC}}}\right), \tag{3.1}$$

where $Q^{\text{max}}_{\text{BBC}}$ and $E^{\text{max}}_{\text{ZDC}}$ is the maximum values of the BBC measured multiplicity and ZDC deposit energy, respectively. The available range of the centrality in the PHENIX experiment is from 0 to 94% due to the trigger efficiency. Moreover, the measured centrality can be related to the impact parameters using the Monte Carlo simulation with the Glauber model, including the detector response. In this analysis, we measure the direct photons with the three centrality classes; minimum bias, 0–40%, and 40–94%.

3.2.4 Reaction plane determination

A reaction plane is a geometrical plane defined by the impact parameter and the beam direction shown in Fig. 3.3. The reaction plane is used for azimuthal anisotropy measurements of produced particles. The angle of the reaction plane is measured from the azimuthal angles of produced particles described as

$$\Psi = \frac{1}{n}\tan^{-1}\left(\frac{Y_n = \sum_i \omega_i \sin(n\phi_i)}{X_n = \sum_i \omega_i \cos(n\phi_i)}\right) \tag{3.2}$$

where X_n and Y_n are the n-th harmonic event flow vectors, and ϕ_i is the particle azimuthal angle.

In the PHENIX experiment, the reaction plane is measured by the BBC detector located in the mid-rapidity $3.1 < \eta < 3.9$. The reaction plane resolution is around 15% in Cu+Cu collisions at $\sqrt{s_{NN}}$ =200 GeV and depends on the centrality. In this analysis, we use the reaction plane information to measure single electron azimuthal anisotropy to correct the combinatorial background shape described in Sec. 3.7.

3.3 Charged particle tracking

We explain the method for the reconstruction of charged-particle tracks and their momentum measurement in this section. Tracks and momenta for charged particles, including electrons and positrons, are reconstructed by

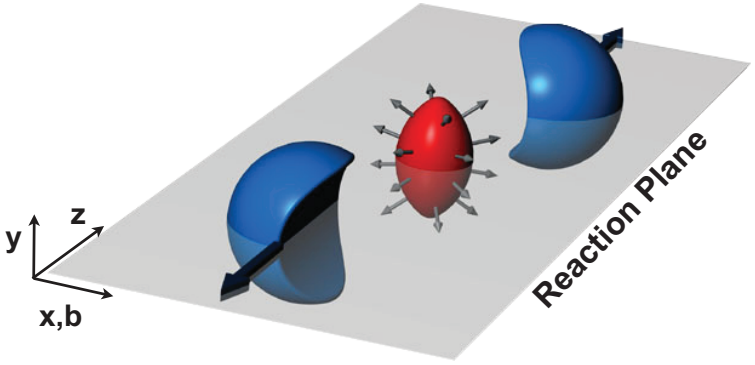

Figure 3.3: The schematic image of reaction plane in heavy-ion collisions. The reaction plane is defined by the impact parameter and the beam direction. [17]

the Drift Chambers and Pad Chambers. Once nucleus-nucleus collision occurs, charged particles are emitted and passed through the magnetic field forced by the PHENIX central magnet. They are bent to the perpendicular direction with respect to the beam pipes until they arrive at the DC. When charged particles reach the DC, they travel straight out due to almost no magnetic field outside the DC.

Charged particle tracks are reconstructed in a two-dimensional space coordinated by ϕ and α. ϕ is the azimuthal angle of a track, and α is an inclination angle of a track with respect to the straight line connecting to the vertex point. Figure 3.4 shows the schematic view of the two-dimensional space for the track reconstruction. The ϕ angle depends on a particle's momentum, and the angle is inverse proportional to the momentum. The curvature sign depends on the particle's charge. The α angle allows the determination of the transverse momentum p_T, and the relation between α and p_T is approximately expressed as:

$$\alpha \simeq \frac{K}{p_T} \tag{3.3}$$

where K is the effective magnetic field integral from the vertex point to the DC.

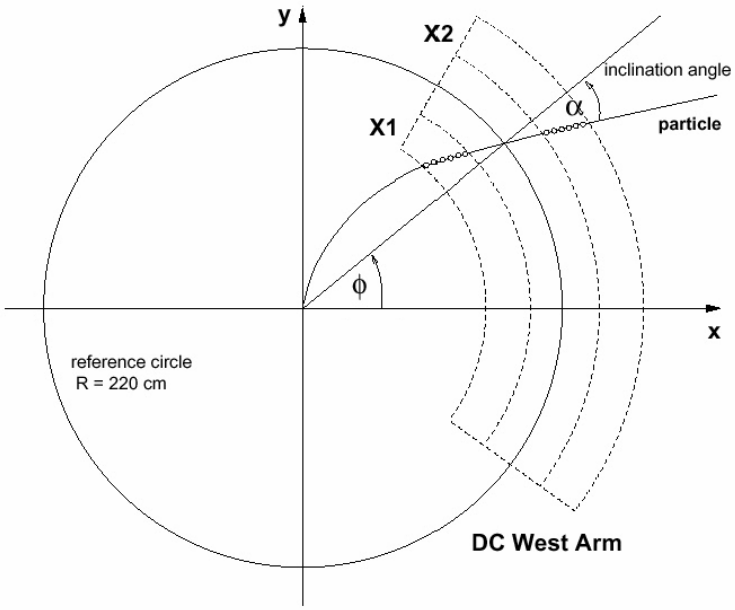

Figure 3.4: The schematic view of a track reconstruction by the Drift Chamber in x-y plane [63]

3.4 Electron and positron identification

We describe the electron identification that is called eID in this section. Several variables from RICH and EMCal measurements are employed for the eID. The eID is applied to the charged particle tracks. We consider the following variables for the eID summarized in Table 3.1.

The electron identification variables in the RICH are n0, chi2/npe0, and disp, while the variables in the EMCal are emcsdphi_e, emcsdz_e, and dep.

n0

The n0 variable is the number of hit RICH photomultipliers. The variable counts the hits within an annular region with a radius between 3.4 and 8.4 cm around the track projection. In comparison, a Cherenkov ring emitted by an electron is expected 5.9 cm radius in the RICH detector. We require the cut with n0$\geq$1.

Table 3.1: The summary of electron identification cuts used in this study

eID cuts	condition
n0	≥ 1
chi2/npe0	≤ 15
disp	≤ 7.5
$\sqrt{\sigma^2_{\Delta\phi} + \sigma^2_{\Delta z}}$	≤ 3
dep	$\leq$ -2σ
p_T	$\geq$ 0.3 GeV/c

disp

The disp variable is displacement which is the distance between the ring center and the track projection. We define the npe0 variable as npe0 $= \sum_i \mathrm{npe}_i$. The npe0 means the number of photo-electrons within the association radius. The ring center is reconstructed using npe0 as

$$r_{\mathrm{center}} \equiv \frac{\sum R_i \times N^i_{\mathrm{pe}}}{\mathrm{npe0}} \tag{3.4}$$

The disp variable is calculated as

$$\mathrm{disp} \equiv \sqrt{(z_{\mathrm{cross}} - z_{\mathrm{center}})^2 - (R_{\mathrm{cross}} - R_{\mathrm{center}})^2} \tag{3.5}$$

where $R_{\mathrm{center}} = (r_{\mathrm{center}}, z_{\mathrm{center}})$ and $(r_{\mathrm{cross}}, z_{\mathrm{cross}})$ is the coordinate which is the track projection onto the PMT plane.

chi2/npe0

The chi2 variable is a χ^2-like variable of the Cherenkov ring shape between the expected and measured rings. The npe0 variable is the number of photo-electrons measured in a given RICH ring. The chi2/npe0 is defined as

$$\mathrm{chi2/npe0} \equiv \frac{\sum_{\mathrm{r_{asso}}} (R_i - R_0)^2 \times N^i_{\mathrm{pe}}}{\mathrm{npe0}} \tag{3.6}$$

where r_i is the hit PMT position, r_0 is the projection point of an associated track, and N^i_{pe} is the number of photo-electrons.

emcsdphi_e and emcsdz_e

The emcsdphi_e and emcsdz_e are the distance between the track projection position and hit position in the EMCal divided by the standard deviation. The hit position is the center of the energy cluster at the surface of the EMCal in azimuthal emcdphi and z-direction emcdz, while the coordinate of the track projection in pemcdphi and pemcdz. The emcsdphi_e and emcsdz_e are expressed as follows:

$$\text{emcsdphi} \equiv \frac{\text{emcdphi} - \text{pemcdphi}}{\sigma_{\text{emcdphi}}(p)} \tag{3.7}$$

$$\text{emcsdz} \equiv \frac{\text{emcdz} - \text{pemcdz}}{\sigma_{\text{emcdz}}(p)}. \tag{3.8}$$

dep

The dep variable is a quantification of an energy-momentum matching. For electrons with momentum above 200 MeV, their mass ($m_e = 511\text{keV}/c^2$) can be negligible. Consequently, the energy deposited in the EMCal must match the momentum. The variable is calculated as

$$\text{dep} \equiv \frac{(E/p - 1)}{\sigma_{E/p}} \tag{3.9}$$

where E and p is a measured energy in the EMCal and track momentum, respectively. $\sigma_{E/p}$ denotes the standard deviation of the E/p distribution.

Summary of electron identification

The RICH related variables n0 and npe0 express the association quality between the track and the hits. In contrast, the disp and chi2/npe0 represent the ring shape reconstruction quality in the RICH. The combination of emcsdphi and emcsdz in the EMCal variables indicate the normalized distance between track projection position and hit position. The variable dep represents the matching with energy and momentum.

3.5 Electron pair selection

Reconstructed electron pairs are applied to several pair cuts to reject the background electron pairs: fake electron pairs from detector ghosts and photon conversion pairs.

The source of any electrons or positrons is unknown; therefore, all electrons and positrons are combined for composing foreground electron pairs. Before employing the foreground pairs in this analysis, the pair cuts are applied to the composed electron pairs.

3.5.1 Detector ghost pair cuts

The first pair cut removes the detector ghost pairs arising if two-electron candidates share the detector information. These electron pairs correlate and can be the background. There are two kinds of origins for ghost pairs: one ghost pairs arise if two electrons have an overlapped RHIC ring, while another produces if two electrons have an overlapping cluster in the EMCal. The ghost pairs do not appear in the mixed events used to estimate the combinatorial background described below section, while only appear in the real events. Therefore, we need to remove the ghost pairs, and then we apply the following two pair cuts for the foreground electron pairs.

RICH ring-share rejection

$$|\Delta dc_{\phi}| < 0.02 \wedge |\Delta dc_{zed}| < 0.5 \tag{3.10}$$

DC ghost-tracks rejection

$$|\Delta cross_{\phi}| < 0.01 \wedge |\Delta cross_{z}| < 25 \tag{3.11}$$

3.5.2 Photon conversion cut

Photon conversions are created by the interaction between photons and the detector material. Real photons from the collisions interact within the beam pipe made of Beryllium ($0.3\ X_0$) with a radius of 4 cm. These photons convert to electron pairs with a probability of about 0.2%. These off-vertex electron pairs are passed through a less magnetic field than the PHENIX tracking algorithm assumes; therefore, it leads to an incorrect reconstruction of the particle momentum and the pair's opening angle. These miss

reconstructed pairs have an invariant mass up to $m_{ee} \sim 0.3$ GeV/c^2. Hence, photon conversion must be removed from the analysis.

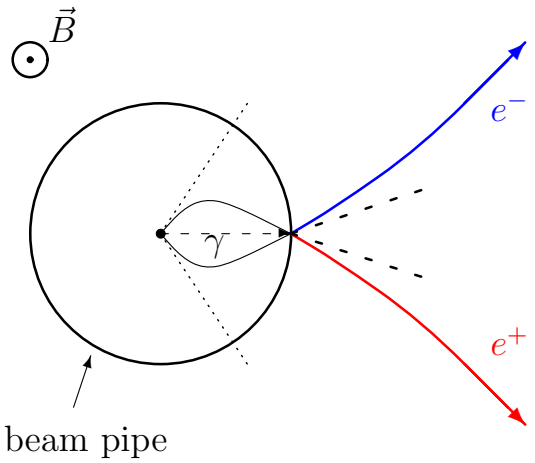

Figure 3.5: A schematic image of the production of photon conversion electron pair at the beam pipe [63]

Figure 3.5 shows the schematic image of a photon conversion. A photon originated from the collision interacts with the beam pipe, and it converts into an electron pair. Blue and red lines represent the reconstructed tracks assuming the PHENIX algorithms, while dashed lines are real tracks. The real opening angle of the pair is much smaller than the reconstructed angle. This incorrect reconstruction causes having an apparent mass that increases with the distance from the collisions vertex. Therefore, photon conversion electron pairs occur in the specific regions in the invariant mass distribution. Corresponding the beam pipe origin pairs appear at $m_{ee} \approx 20$ MeV/c^2, while the detector material origin appears at $m_{ee} \approx 80$ MeV/c^2 and $m_{ee} \approx 125$ MeV/c^2. Moreover, the Helium bag contributes the conversion peak $m_{ee} \leq 300$ MeV/c^2.

To reject the conversion electron pairs, we apply the ϕ_v cut on the pairs' orientation in the magnetic field. The ϕ_v is defined as

$$\boldsymbol{u} = \frac{\boldsymbol{p_1} + \boldsymbol{p_2}}{|\boldsymbol{p_1} + \boldsymbol{p_2}|} \tag{3.12}$$

$$\boldsymbol{v} = \boldsymbol{p_1} \times \boldsymbol{p_2} \tag{3.13}$$

$$\boldsymbol{\omega} = \boldsymbol{u} \times \boldsymbol{v} \tag{3.14}$$

$$\boldsymbol{u_a} = \frac{\boldsymbol{u} \times \hat{\boldsymbol{z}}}{|\boldsymbol{u} \times \hat{\boldsymbol{z}}|} \tag{3.15}$$

$$\phi_v = \arccos\left(\frac{\boldsymbol{\omega} \cdot \boldsymbol{u_a}}{|\boldsymbol{\omega}||\boldsymbol{u_a}|}\right) \tag{3.16}$$

where $\boldsymbol{p}$ is a momentum vector of electrons, and z is a unit vector of z-direction.

3.6 Electron pair invariant mass

Identified electrons and positrons reconstruct their pair invariant-mass. The invariant mass of electron pairs are calculated as follows:

$$m_{ee} = \sqrt{(E_{e^+} + E_{e^-})^2 - (\boldsymbol{p}_{e^+} + \boldsymbol{p}_{e^-})^2} \tag{3.17}$$

where E is an energy, and $\boldsymbol{p}$ is a momentum vector of electron and positron.

The square of the energies are calculated from the electron mass and momentum as:

$$(E_{e^+} + E_{e^-})^2 = \left(\sqrt{m_{e^+}^2 + \boldsymbol{p}_{e^+}^2} + \sqrt{m_{e^-}^2 + \boldsymbol{p}_{e^-}^2}\right)^2 \tag{3.18}$$

where m_e is the electron mass = 511 keV/c^2.

The transverse momentum of the pair is calculated as:

$$p_T = \sqrt{(p_{x,+} + p_{y,+})^2 + (p_{x,-} + p_{y,-})^2}. \tag{3.19}$$

3.7 Detector response in simulations

This section describes the tuning of electron identification variables and detector response, including the acceptance in the simulation. The PHENIX detectors include a mix of good and bad areas. To stabilize the acceptance, we remove the lousy acceptance areas from the analysis and discrepancy between the data and the simulations. To evaluate background contributions

and known hadronic components, we use Monte Carlo simulations; one simulation is for particle decays. Another is for reproducing detector response, including geometrical acceptance and electron identification efficiencies. The detector response in simulations must match with the experimental data due to reproducing background distributions precisely. Therefore, we tune the detector response in the simulations to replicate the experimental data and confirm their agreement.

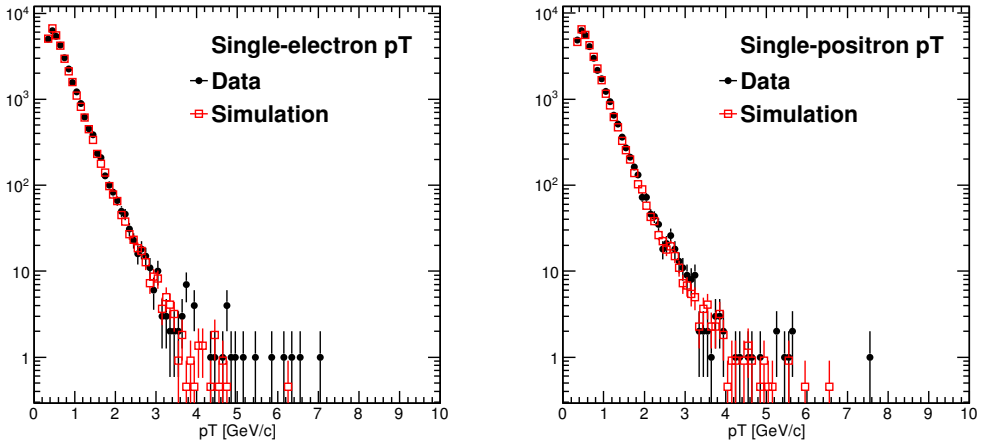

Figure 3.6: Single electron p_T compare with the data and the simulation

At first, we describe the distribution tuning of single-electron transverse momentum. EXODUS is a fast Monte Carlo simulation of hadron decays, and it simulates the particle generations and decays. It can reproduce given decay modes for a given particle. The input shape of transverse momentum in the EXODUS simulation is the modified Hagedorn function described in Sec. 3.9.3. Generated particles in EXODUS are passed through the PISA simulation. PHENIX Integrated Simulation Application, named PISA, is a GEANT3-based Monte Carlo simulation [74], and it simulates a detector response, including reconstruction efficiencies, detector smearing, material effects, and detector oriented backgrounds [75].

Figure 3.6 shows the transverse-momentum distribution comparison between the data and the simulation for electrons and positrons. In order to compare the distribution, electron pairs in the experimental data are selected with the invariant mass $m_{ee} < 0.03$ GeV/c^2 where π^0 Dalitz decay electrons

are dominant region. In the simulation, π^0 Dalitz decays are simulated, and the generated electrons and positrons are passed through the PISA to simulate the PHENIX detector response. The black and red markers in the figure denote the experimental data and simulation results, respectively. The reproduced distributions by the simulation are compatible with the experimental data.

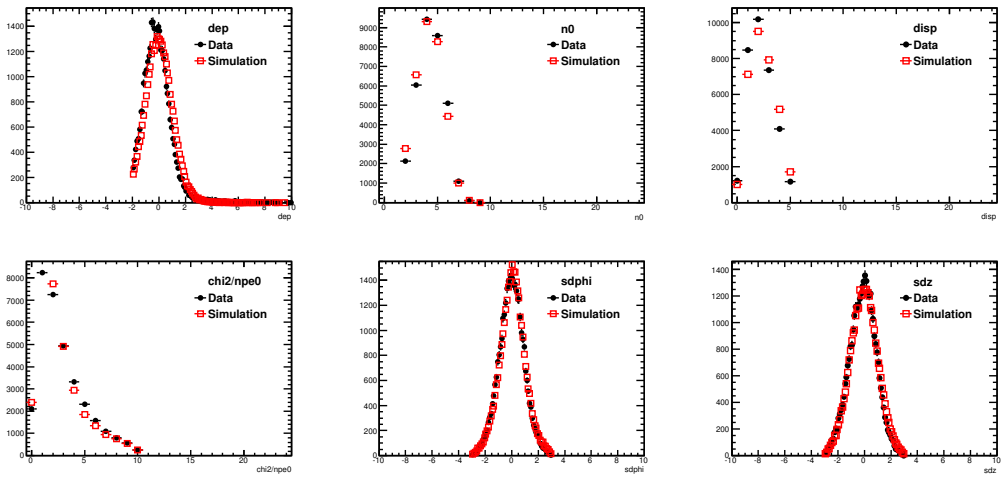

Figure 3.7: The elD variable comparison between the data and the simulation for electrons.

Next, we explain the tuning of electron identification (eID) variables in the simulation. Generated particles by the simulation are applied eID cuts, which are the same as the experimental data analysis. We check the response of eID variables in the simulation and compare the variable distributions.

Figures 3.7 and 3.8 show the tuning results of eID variable for both electrons and positrons. The invariant mass of electron pairs in the data is selected below 0.03 GeV/c^2 similar to the transverse momentum comparison. In the simulation, π^0 Dalitz decay electrons are employed for this comparison. The black and red markers denote the eID variable distributions of the real data and simulation results, respectively. The tuned eID variables in the simulation are agreeable with the data.

Lastly, we apply the fiducial cuts to reject the unstable or dead areas in the detectors. The PHENIX detector contains unstable and dead areas, and these regions are rejected in the experimental data analysis. In the simula-

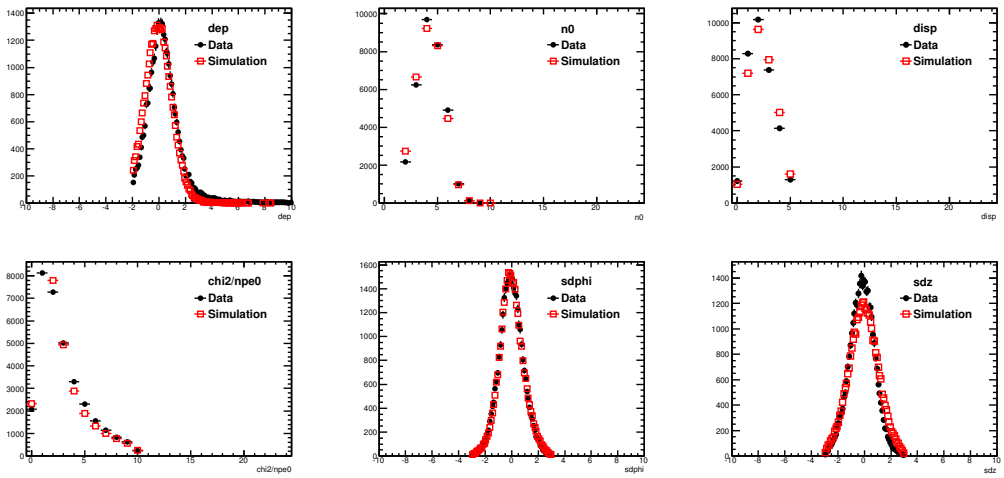

Figure 3.8: The elD variable comparison between the data and the simulation for positrons.

tion, we apply the same fiducial cuts in the experimental data to reproduce the insufficient areas. We consider the two main detectors, the Drift Chambers and the EMCal, for this tuning.

Figure 3.9 represents the Drift Chamber's hit maps of single electrons and positrons in the data and the simulation. The map is broadly divided into four segments; In a clockwise direction, North-West, North-East, South-West, and South-East are located. The horizontal axis represents *zed*, while the vertical axis is *dcphi*. The zed parameter is the z coordinate at which the particle track crosses the PC1. The dcphi is the coordinate of azimuth angle ϕ at which the particle track crosses the DC reference radius. The low-efficiency areas are rejected, and the hit map on the simulation is compatible with the data.

Figure 3.10 shows the EMCal's hit maps for both the data and the simulation. The hit maps consist of four segments as well as the DC's. The horizontal axis represents *emc-z*. Meanwhile, the vertical axis denotes the *emc phi*. These variables represent z and ϕ coordinate, respectively. The low-efficiency areas indicated the box-shape are removed from both the data and the simulation.

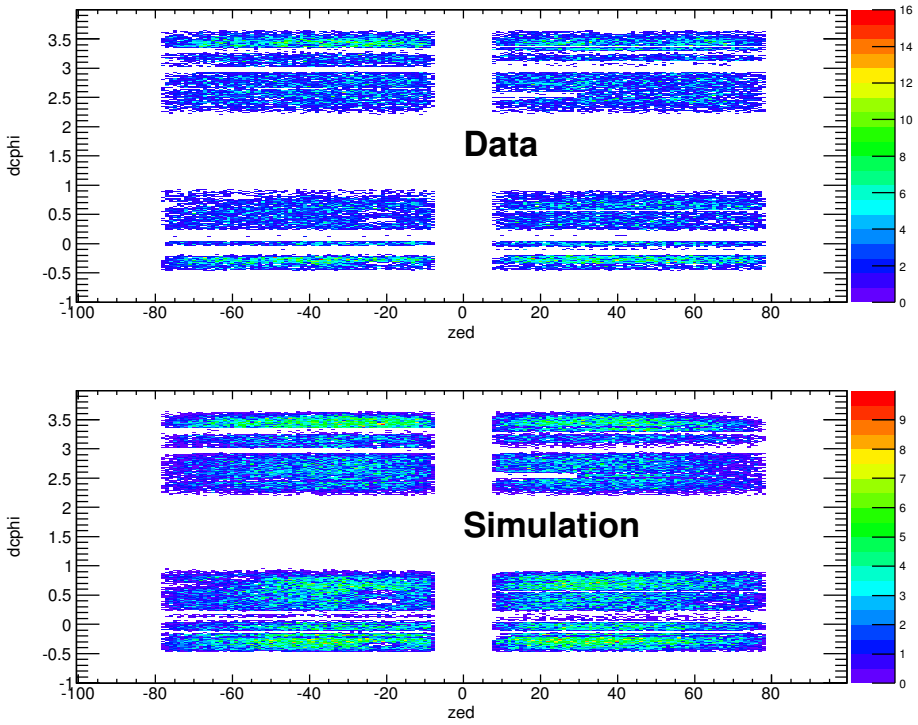

Figure 3.9: Hit map for dcphi and zed

3.8 Overview of background subtraction

Direct virtual photon contribution is extracted as an excess over the known significant component from hadron decays after subtracting extensive backgrounds. The signal-to-background ratio (S/B) is only a few percent in p+p and d+Au collisions, whereas the S/B reaches 15% in Au+Au collisions. Therefore, precise background estimation plays an essential role in this analysis.

We employ a simulation-based approach to background estimation and subtraction in this analysis. This approach employs well-tuned Monte Carlo simulations to estimate correlated backgrounds, together with the data for the uncorrelated background estimation. The advantage of the approach is that it realizes a smaller statistical error than a data-driven approach. The data-driven approach is a background estimation method using the foreground like-sign electron pairs. The reproduced total background by the

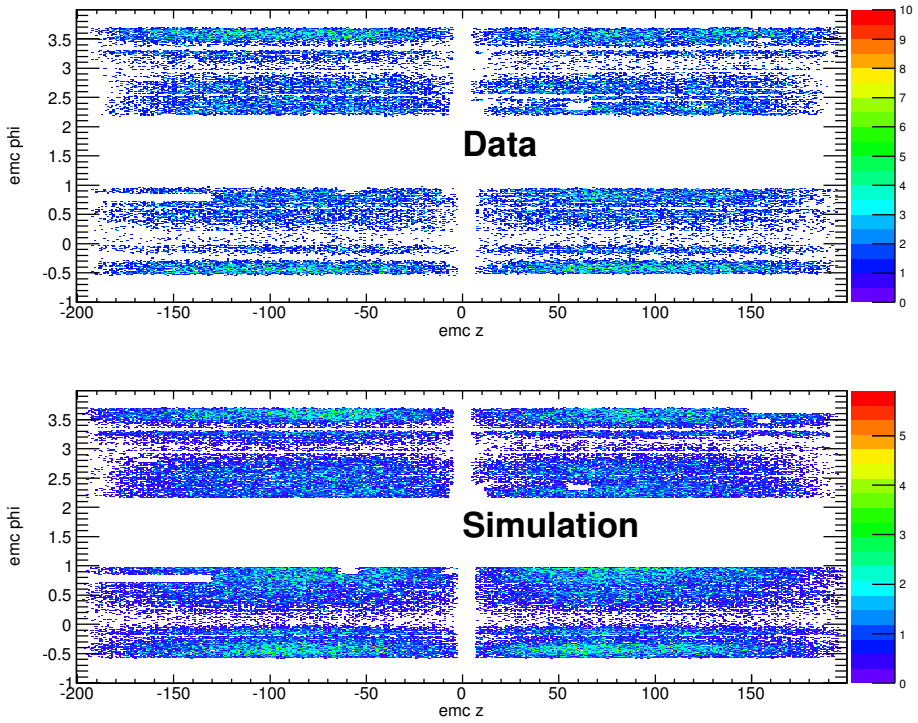

Figure 3.10: Hit map for emcphi and emc-z

simulation-based approach is compared to the data-driven approach as a cross-check.

We explain the simulation-based approach first and then describe the data-driven approach and a cross-check for the background estimation in the following sections.

3.9 Simulation-based approach

In the simulation-based approach, background contributions are estimated by both the experimental data and the well-tuned Monte Carlo simulations.

After removing detector-oriented fake pairs and conversion pairs, the foreground distributions for unlike-sign (FG_{+-}) and like-sign (FG_{++} and FG_{--}) pairs can be expressed as

$$\mathrm{FG}_{--} = \mathrm{BG}^{\mathrm{CM}}_{--} + \mathrm{BG}^{\mathrm{XC}}_{--} + \mathrm{BG}^{\mathrm{JP}}_{--} = \mathrm{BG}^{\mathrm{SUM}}_{--} \quad (3.20)$$

$$\mathrm{FG}_{++} = \mathrm{BG}^{\mathrm{CM}}_{++} + \mathrm{BG}^{\mathrm{XC}}_{++} + \mathrm{BG}^{\mathrm{JP}}_{++} = \mathrm{BG}^{\mathrm{SUM}}_{++} \quad (3.21)$$

$$\mathrm{FG}_{+-} = \mathrm{S} + \mathrm{BG}^{\mathrm{SUM}}_{+-} + \mathrm{HD}_{+-}. \quad (3.22)$$

The foregrounds (FG) for like-sign pairs are consisted of three kinds of backgrounds; combinatorial background (CM), jet-induced electron pairs (JT), and correlated cross pairs from Dalitz and double Dalitz decays (XC), while the foreground for unlike-sign structured the backgrounds, correlated electron pairs from hadron decays, and the signal arising from the virtual photons. It is notable that the like-sign foregrounds are composed of only backgrounds, while the unlike-sign foreground includes hadronic and virtual photon contributions.

The signal component is extracted by subtracting backgrounds from the foreground in unlike-sign pairs. The foreground shapes are reproduced by the data, while the background shapes are calculated by both the data and the well-tuned Monte Carlo simulations. The total background distribution is obtained from the foreground simultaneous fit by all background components in the like-sign pairs. The scaling factors calculated by the fit can be diverted into the background scaling for unlike-sign pairs.

Table 3.2 is the summary of the components in foregrounds. Each background estimation are described in the below sections.

Table 3.2: Signal and background contributions in low mass electron pairs.

Component	Source	Symbol
Signal	Direct virtual photons	S
Combinatorial background	Uncorrelated origin	$\mathrm{BG}^{\mathrm{CM}}$
Jet-induced pair	Near and away sides jets	$\mathrm{BG}^{\mathrm{JP}}$
Correlated cross pair	Dalitz and double Dalitz decays	$\mathrm{BG}^{\mathrm{XC}}$
Hadron cocktail	Hadron decays	HD

3.9.1 Combinatorial backgroud

The combinatorial background is arising from a random combination of uncorrelated electron and positron pairs. Electron pairs are reconstructed with all combinations because we can not identify the correct pairs which are originated from the same parent particle. Therefore, we estimate the distribution of the uncorrelated pairs and subtract them.

The event mixing technique is widely used to reproduce the combinatorial background. This technique uses different collision events with similar event topology, and electron pairs are created from two different events. Similar topology events are selected by using z-vertex position, centrality, and reaction plane. The electron pairs created by the technique can reproduce uncorrelated pairs because two different collisions are completely uncorrelated. The event mixing technique has a benefit to reduce the statistical error due to increasing the statistics by deepening accumulating in a buffer.

As reported in the previous study [27], the traditional event-mixing technique does not fully replicate the foreground combinatorial background. The elliptic flow leads to the modulation of the foreground combinatorial background distribution. Elliptic flow is an azimuthal anisotropy of particle emission. In non-central heavy-ion collisions, the participant region's shape is elliptical; in other words, created particles distribute are not uniformly distributed to the reaction plane. The pressure gradient of the hot-and-dense matter depends on the direction, and particles in the matter expand according to the pressure gradient. This fluid flow leads to elliptic flow, and particles are observed with non-uniform distribution on momentum space. The electron pairs reproduced by the event-mixing method are randomly picked-up pairs from the different events; therefore, they do not have any flow effect on average. However, in the foreground combinatorial pairs, they are inherently affected by the flow.

The modulation between the foreground combinatorial background and the event-mixing background is to be solved if the reaction plane is measured with perfect resolution. The standard event-mixing technique reproduces the combinatorial background shape using the same topology events with selecting reaction plane, centrality, and z-vertex. The resolution of the reaction plane measured by the PHENIX detector has a limitation. Consequently, the event mixing can not adequately reproduce the uncorrelated combinatorial background shape. To consider the elliptic flow effect on the event-mixing method, we employ a weighting method that the flow effect weights the re-

produced shapes.

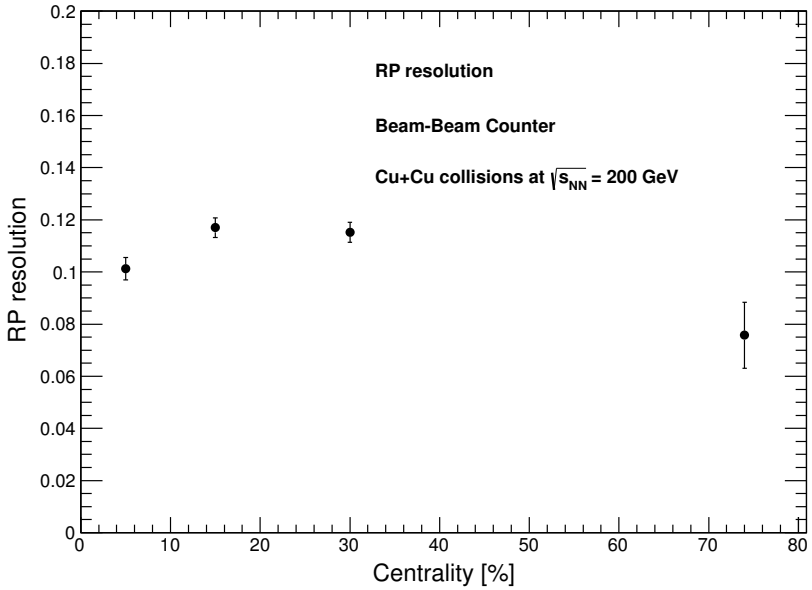

Figure 3.11: Reaction plane resolution as a function of centrality measured with the BBC detector in Cu+Cu collisions at $\sqrt{s_{NN}} = 200$ GeV

The elliptic flow can be expressed as the following equation:

$$\frac{dN\left(\phi\right)}{d\phi} \propto 1 + 2v_2 \cos 2\phi. \tag{3.23}$$

where v_2 is the second-order Fourier coefficient, and the ϕ is the azimuthal angle [27]. Hence, the random combination of the anisotropy affected particles distributes as

$$w\left(\phi_a - \phi_b\right) = 1 + 2v_{2,a}v_{2,b} \cos 2\left(\phi_a - \phi_b\right) \tag{3.24}$$

where $\phi_{a(b)}$ and $v_{2,a(b)}$ are the pair opening angle and azimuthal anisotropy of each electron in a pair, respectively. The combinatorial background pairs reproduced by the event-mixing method, the mixed background pairs, are weighted by the w. To evaluate the w, we measure single electron elliptic flow, v_2 as a function of transverse momentum for each centrality class.

Single electron v_2 is measured by the event plane method [76]. The event plane method is a widely used technique to measure the anisotropy in heavy ion collisions. Single electron v_2 is measured with the equation

$$v_2 = \frac{\langle \cos\left(2\left[\phi - \Psi_2\right]\right)\rangle}{\sqrt{\langle \cos\left(2\left[\Psi_{2,\mathrm{BBCNorth}} - \Psi_{2,\mathrm{BBCSouth}}\right]\right)\rangle}} \tag{3.25}$$

where ϕ is the azimuthal angle of an electron, Ψ_2 is the reaction plane angle measured by both BBC North and South, and the denominator represents the reaction plane resolution caused by the finite multiplicity. The reaction plane angle Ψ is determined by

$$\Psi_2 = \frac{1}{2}\left(\tan^{-1}\frac{\sum_i w_i \sin\left(2\phi_i\right)}{\sum_i w_i \cos\left(2\phi_i\right)}\right). \tag{3.26}$$

Figure 3.11 shows the reaction plane resolution as a function of centrality measured by the BBC detector. The evaluated results are used as the denominator in Equation 3.25.

Figure 3.12 shows the results of the single-electron elliptic flow, v_2, as a function of transverse momentum. We measure the elliptic flow with four centrality bins: 0–10, 10–20, 20–40, and 40–94%. We apply a simple exponential function fit to the measured v_2. The fit function is expressed by $A/\exp\left(B/p_T\right)$, where A and B are the free parameters, and they are calculated by the least-squares method. The best-fit results are listed in Table 3.3, and they are used for the weight calculation in Eq. 3.24.

Table 3.3: The best-fit parameter values in $A/\exp\left(B/p_T\right)$ for single-electron elliptic flow in Cu+Cu collisions at $\sqrt{s_{NN}} = 200$ GeV

Centrality	A	B
0–10%	0.123	0.243
10–20%	0.163	0.326
20–30%	0.165	0.251
30–40%	0.256	0.593
40–94%	0.154	0.291

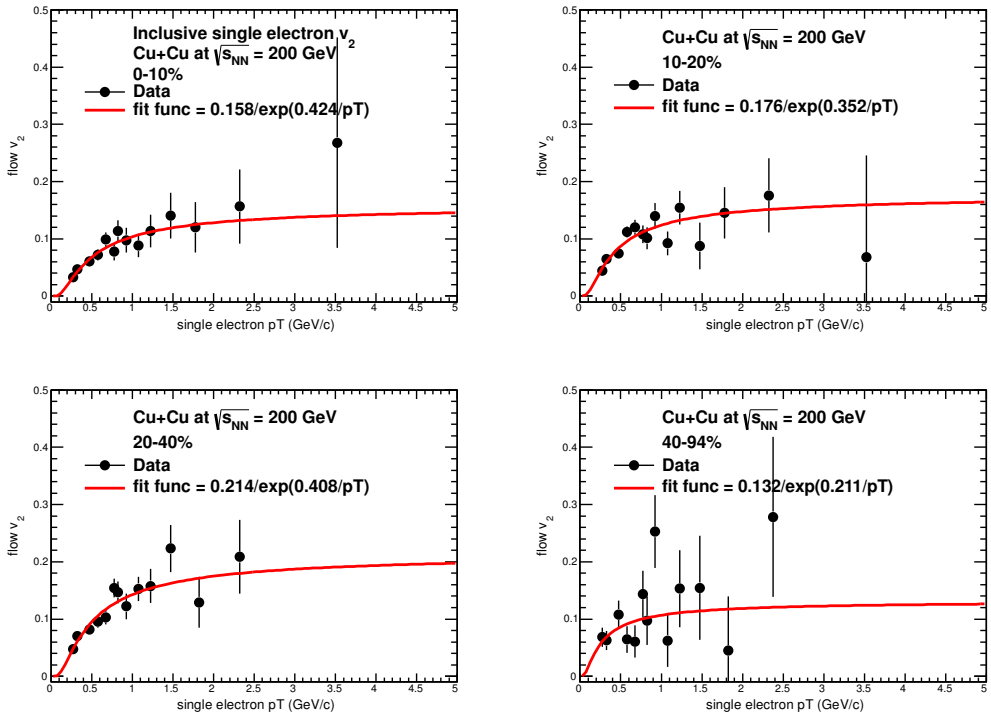

Figure 3.12: Single-electron elliptic flow v_2 as a function of transverse momentum with the best-fit result in Cu+Cu collisions at $\sqrt{s_{NN}} = 200$ GeV

3.9.2 Jet-induced correlated pairs

Jet-induced correlated pairs are a background that is produced by two electrons originated from the same jet or back-to-back jets. A jet is a phenomenon that particles are generated concentratedly at a narrow angle. The initial hard scattering of partons generates the jets. The scattered partons traversing the medium lose their energy through bremsstrahlung and collisional energy loss and then fragment into collimated particles called jets. The event mixing technique can not remove the jet-induced electron pairs due to their correlation. Thus, the invariant mass shape of the jet-induced pairs is evaluated by Monte Carlo simulations.

PYTHIA8 with CTEQ5L parton distribution function simulates jet events to produce the correlated electron pairs [77, 78, 79]. PYTHIA is a Monte Carlo simulation widely used in high-energy particle physics for the particle

Table 3.4: Considered QCD processes in PYTHA simulation. g denotes a gluon, $f_{i,j,k}$ are fermions with flavor i, j, and k, and $\bar{f}_{i,j,k}$ are the corresponding antiparticles.

MSUB 11	$f_i f_j \to f_i f_j$
MSUB 12	$f_i \bar{f}_i \to f_k \bar{f}_k$
MSUB 13	$f_i g \to gg$
MSUB 28	$f_i g \to f_i g$
MSUB 53	$gg \to f_k \bar{f}_k$
MSUB 68	$gg \to gg$

generation from a hard process to a multihadronic final state. We consider hard quantum-chromodynamics (QCD) processes tabulated in Table 3.9.2. The evaluation procedure is the same as Reference [27], but PYTHIA8 is used in this work. Generated particles in the final state in the PYTHIA8 simulation are passed through a GEANT3-based simulation PISA of the PHENIX detector to consider the detector acceptance and efficiencies.

The foreground electron pairs from the PYTHIA events consist of jet-induced pairs that we are interested in, physical pairs, cross pairs, and combinatorial pairs expressed as

$$\mathrm{FG_{sim}} = \mathrm{BG^{PP}_{sim}} + \mathrm{BG^{CM}_{sim}} + \mathrm{BG^{XC}_{sim}} + \mathrm{BG^{JT}_{sim}} \tag{3.27}$$

where $\mathrm{BG^{PP}_{sim}}$ denotes the physical pair. Therefore, the jet-induced pairs are extracted from the foreground pairs from the simulation.

The event-mixing technique evaluates uncorrelated combinatorial backgrounds in the simulated events. It is found that the shape of the like-sign invariant mass distribution for mixed pairs is consistent with that for the foreground pairs in $0.6 < m_{ee} < 1.1$ GeV/c^2. The specific invariant mass region is employed for the normalization of the mixed pairs. The physical pairs and cross pairs are excluded from the foreground by requiring that the pair's two electrons do not share the same particle in their history. After subtraction and rejection of combinatorial pairs, physical pairs, and cross pairs, the remaining pairs expresses the jet-induced correlated electron pairs.

The invariant mass shapes for jet-induced electron pairs evaluated by the simulation are shown in Fig. 3.13. It is known that jets passing through a medium lose energy, and the phenomenon is called jet-quenching. Ac-

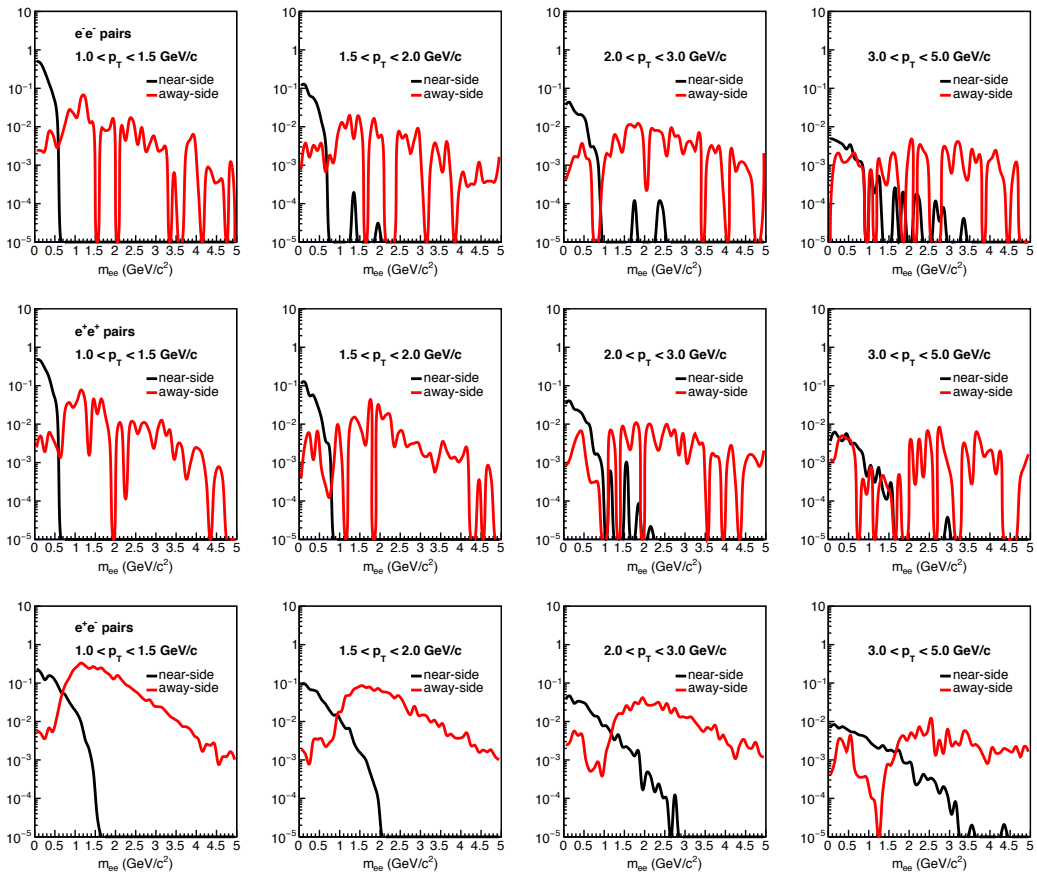

Figure 3.13: Invariant mass distributions for near-side jet and back-to-back jets evaluated by the PYTHIA8 and PISA simulations.

cordingly, the scaling factors of near- and away-side jets are supposed to be different in heavy ion collisions. Therefore, the electron pairs from the same jet and the back-to-back jet are separately plotted. The opening angle $\Delta\phi_0^{prim}$ of the two electrons defines the origin of the correlated pair: if $\Delta\phi_0^{prim} < \pi/2$, the pairs are originated by the same jet. if $\Delta\phi_0^{prim} > \pi/2$, the pairs are produced by the back-to-back jet.

3.9.3 Correlated cross pairs

Another non-negligible background arises from double Dalitz decays of the π^0 and η mesons:

$$\begin{aligned} \pi^0 &\rightarrow e_1^+ e_1^- \gamma^* \rightarrow e_1^+ e_1^- + e_2^+ e_2^- \\ \eta &\rightarrow e_1^+ e_1^- \gamma^* \rightarrow e_1^+ e_1^- + e_2^+ e_2^- . \end{aligned} \tag{3.28}$$

Dalitz decay is a meson decay, and it creates two leptons and a photon in the final state. Double Dalitz decay is also a meson decay that involved a virtual photon, and it produces four particles in the final state. The cross combination of electrons from double Dalitz decays give rise to two unlike-sign pairs ($e_1^+ e_2^-$ and $e_2^+ e_1^-$) and two like-sign pairs ($e_1^+ e_2^+$ and $e_1^- e_2^-$). These electron pairs are not a thoroughly combinatorial background, but they are associated with the π^0 or η invariant mass and momentum. Therefore, the contribution can not be reproduced by the event-mixing method, and it is needed to evaluate independently.

The Dalitz decay of the π^0 and η mesons also lead to the correlated cross pairs if a photon converts into electron pairs via external conversion. A real photon interacts with detector matters, and it probabilistically decays into an electron pair. The decays express as:

$$\begin{aligned} \pi^0 &\rightarrow e_1^+ e_1^- \gamma \rightarrow e_1^+ e_1^- + e_2^+ e_2^- \\ \eta &\rightarrow e_1^+ e_1^- \gamma \rightarrow e_1^+ e_1^- + e_2^+ e_2^- . \end{aligned} \tag{3.29}$$

The Dalitz decays with the external conversion have four-electrons in the final state, and then these are taken into account in reproducing the cross-pair invariant-mass shape. The contribution from Dalitz decays with the external conversion is considered in Reference [27].

The correlated cross pairs themselves can not be reconstructed individually by the data. We employ the Monte Carlo simulations of EXODUS and PISA to calculate the shape of cross pair invariant-mass. The key input to EXODUS is the momentum distributions. The π^0 momentum distribution in Cu+Cu collisions at $\sqrt{s_{NN}} = 200$ GeV measured by the PHENIX experiment

is successfully parameterized by a modified Hagedorn function [80, 81]:

$$E\frac{d^3\sigma}{dp^3} = A\left(e^{-\left(ap_T+bp_T^2\right)} + p_T/p_0\right)^{-n}. \tag{3.30}$$

The parameters in the function for three centrality bins are summarized in Table 3.9.3. The momentum distribution of the η meson is obtained from the transverse invariant-mass scaling, called m_T scaling [82]. The parameterized spectra by the m_T scaling are calculated with replacement p_T by

$$\sqrt{p_T^2 - m_{\pi^0}^2 + m_h^2} \tag{3.31}$$

where m_{π^0} is invariant mass of the π^0 meson, and m_h denotes the invariant mass of hadrons.

Table 3.5: The parameters in the modified Hagedorn function for the π^0 meson for 0–40%, 40–94%, and minimum bias centrality bins in Cu+Cu collisions at $\sqrt{s_{NN}} = 200$ GeV

Fit parameter	0–40%	40–94%	Minibum Bias
$A\,[\mathrm{mbGeV}^{-2}c^3]$	$(3.5 \pm 2.8) \times 10^2$	$(3.5 \pm 3.7) \times 10$	$(1.8 \pm 0.6) \times 10^2$
$a\,[(\mathrm{GeV/c})^{-1}]$	0.41 ± 0.22	0.49 ± 0.54	0.42 ± 0.09
$b\,[(\mathrm{GeV/c})^{-2}]$	0.22 ± 0.16	$6.4 \times 10^{-3} \pm 0.46$	0.20 ± 0.07
$p_0\,[\mathrm{GeV}/c]$	0.70 ± 0.09	0.80 ± 0.76	0.69 ± 0.04
n	8.02 ± 0.15	8.28 ± 2.58	8.01 ± 0.07

The EXODUS and PISA simulation procedure is as follows: First, Dalitz and double Dalitz decays of the π^0 and η mesons are produced by EXODUS. The particle generations follow with the flat vertex distribution with $|z| <$ 30 cm, flat pseudorapidity distribution within $|\eta| < 0.6$, and the uniform azimuthal distribution within $0 < \phi < 2\pi$. The modified Hagedorn function weights the transverse momentum distributions. Second, generated electrons and positrons are passed through the PISA simulation to consider detector reconstruction efficiencies, smearing, and material effects. Third, we apply the electron identification and the pair cuts procedures, which are the same as the experimental data analysis. After the selections, we reproduce the

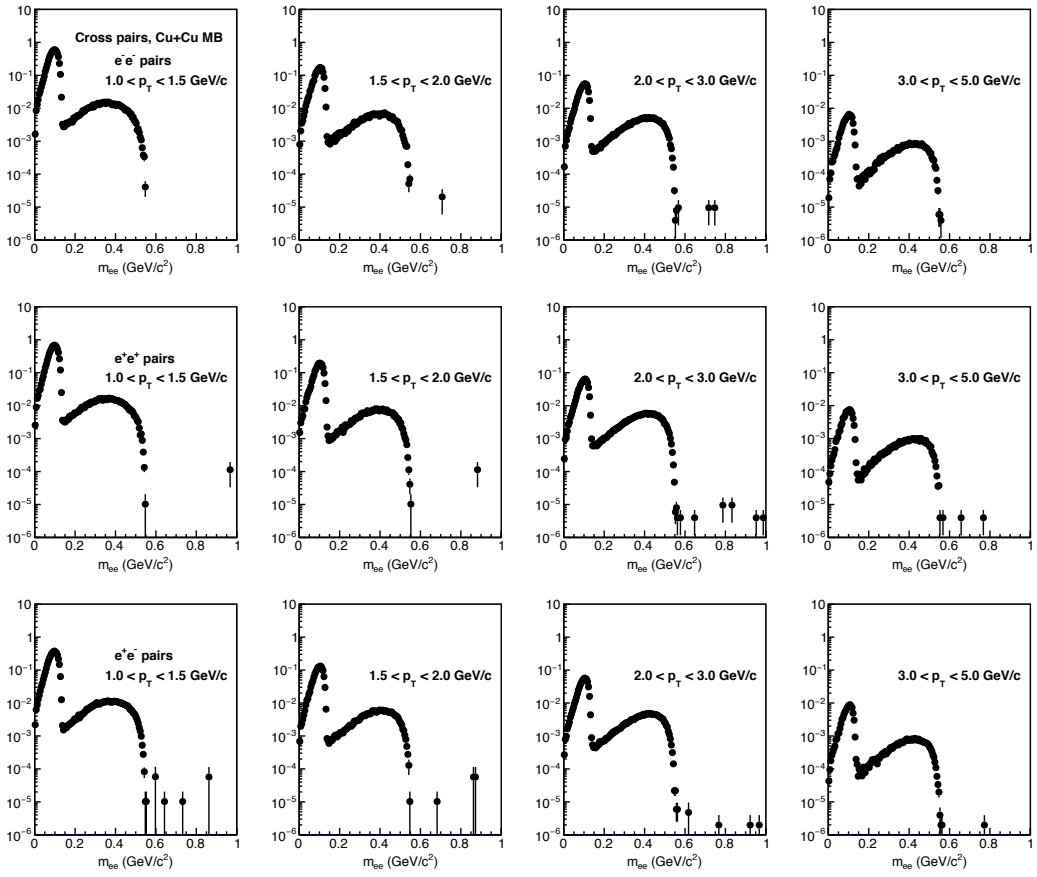

Figure 3.14: The invariant mass shapes for π^0 and η cross pairs produced by the EXODUS and PISA simulation with the configuration of $\sqrt{s_{NN}} = 200$ GeV Cu+Cu collisions.

invariant mass distribution of the cross pairs from the Dalitz and double Dalitz decays. The relative scale between π^0 and η is normalized by the π^0 to meson ratios measured by the PHENIX experiment. Further, each decay modes are weighted by their branching ratios.

Reproduced invariant mass shapes of the π^0 and η cross pairs for minimum bias events are shown in Fig. 3.14. The lower side peak is produced from π^0 decays, while the higher side peak arises from η decays. The invariant mass distributions are produced for each centrality bin with four transverse momentum region for like- and unlike-sign pairs.

3.10 Background normalization

We explain the background normalization in this section. The background shapes evaluated in the previous sections are normalized to the foreground distribution. The normalization is done by a four-component fit, which is simultaneously fit to the foreground distribution FG by the background components, $\mathrm{BG}^{\mathrm{CM}}$, $\mathrm{BG}^{\mathrm{JT}}_{\mathrm{near}}$, $\mathrm{BG}^{\mathrm{JT}}_{\mathrm{away}}$, and $\mathrm{BG}^{\mathrm{XC}}$.

$$\begin{aligned}\mathrm{FG}_{++,--} =& n_{\mathrm{CM}}\mathrm{BG}^{\mathrm{CM}}_{++,--} + n_{\mathrm{JP}_{\mathrm{near}}}\mathrm{BG}^{\mathrm{JP}_{\mathrm{near}}}_{++,--} \\ &+ n_{\mathrm{JP}_{\mathrm{away}}}\mathrm{BG}^{\mathrm{JP}_{\mathrm{away}}}_{++,--} + n_{\mathrm{XC}}\mathrm{BG}^{\mathrm{XC}}_{++,--} = \mathrm{BG}^{\mathrm{SUM}}_{++,--}\end{aligned} \tag{3.32}$$

where n_{CM}, $n_{\mathrm{JP}_{\mathrm{near}}}$, $n_{\mathrm{JP}_{\mathrm{away}}}$, and n_{XC} are the normalization factor to be evaluated by the fit. In the fit, jet-induced pairs from the same-jet (near-side) and the back-to-back jet (away-side) are treated separately because the effect of jet quenching is assumed to be different. If partons pass-through created hot-and-dense matter in the heavy-ion collision, they might lose their energy, called the jet quenching phenomenon. Therefore, it is reasonable to assume that the same- and back-to-back jets' normalization factor is different. The fit is applied to both like-sign BG_{--} and BG_{++} distributions simultaneously.

The four-component fit is done with the transverse momentum $1 < p_T < 5$ GeV/c for each centrality bin. Figure 3.15 shows the like-sign and unlike-sign invariant mass distributions of the foreground FG together with the normalized background $\mathrm{BG}^{\mathrm{SUM}}$ for minimum bias events. The normalized $\mathrm{BG}^{\mathrm{SUM}}$ has a good agreement to the data for like-sign pairs. Meanwhile, there is a significant deviation between the $\mathrm{BG}^{\mathrm{SUM}}_{+-}$ and the foreground distribution of unlike-sign pairs below the 0.3 GeV/c^2 region. This deviation contributes from the signal and the known hadron decays described in Sec. 3.13.

The calculated normalization factors are applied to the normalization for each transverse-momentum range. Further, the calculated normalization factors in like-sign distributions are employed for the scaling of unlike-sign background distributions. Figures 3.16, 3.17, and 3.18 show the results on the fits for minimum bias, 0–40%, and 40–94% centrality events, respectively. The top panels in each figure represent the like-sign invariant mass distributions of the data together with the normalized background components, and the bottom panels express the unlike-sign distributions. The total evaluated backgrounds $\mathrm{BG}^{\mathrm{SUM}}$ are compatible with the foreground distributions FG for like-sign electron pairs.

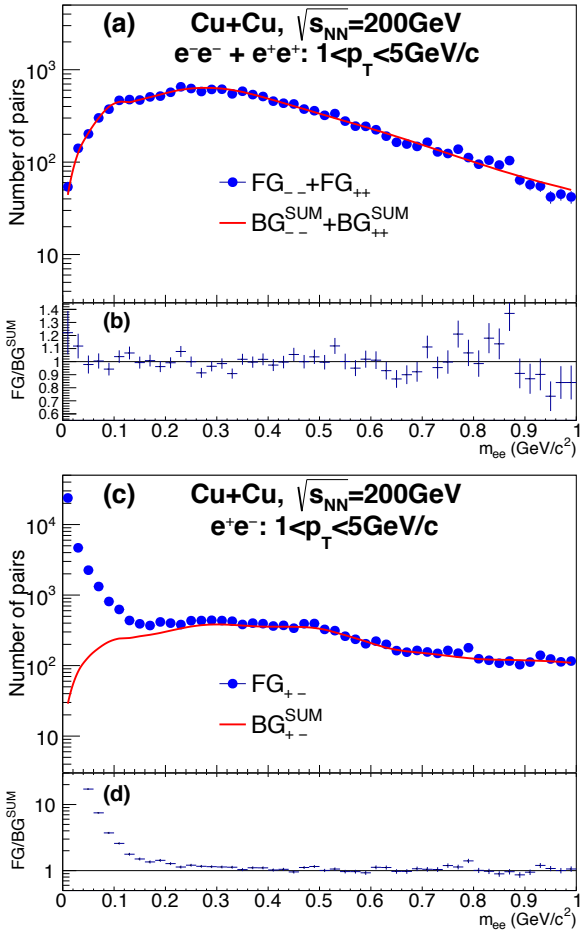

Figure 3.15: Like-sign and unlike-sign electron-pair invariant-mass distributions of the data together with evaluated backgrounds for Cu+Cu minimum bias events.

3.11 Data-driven approach

We explain the data-driven approach, which is another method for background estimation in this section. This method is mainly applied for a cross-check of the background estimation in this study. The data-driven approach is a well-known technique as the like-sign subtraction method [83]. The method demonstrates the background distribution by the foreground-like-sign electron pairs corrected the acceptance effect. The like-sign foreground

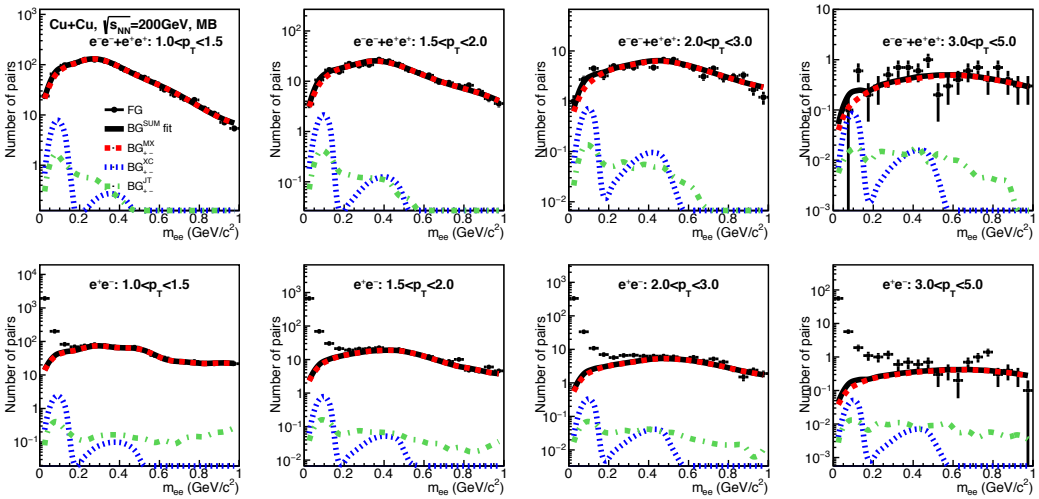

Figure 3.16: Like-sign and unlike-sign electron-pair invariant-mass distributions of the data together with evaluated backgrounds for Cu+Cu minimum bias events.

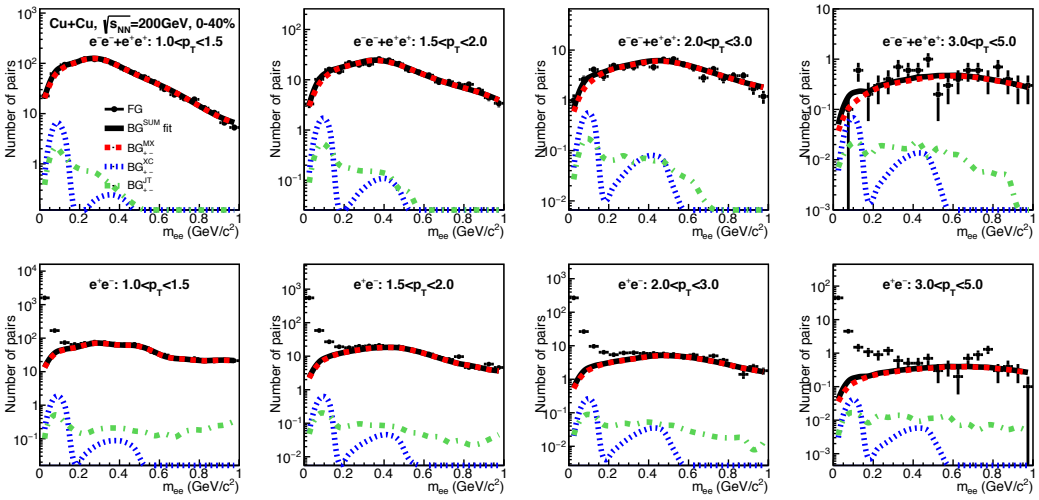

Figure 3.17: Like-sign and unlike-sign electron-pair invariant-mass distributions of the data together with evaluated backgrounds for Cu+Cu 0–40% centrality events.

pairs are only composed of background components, and the like-sign and

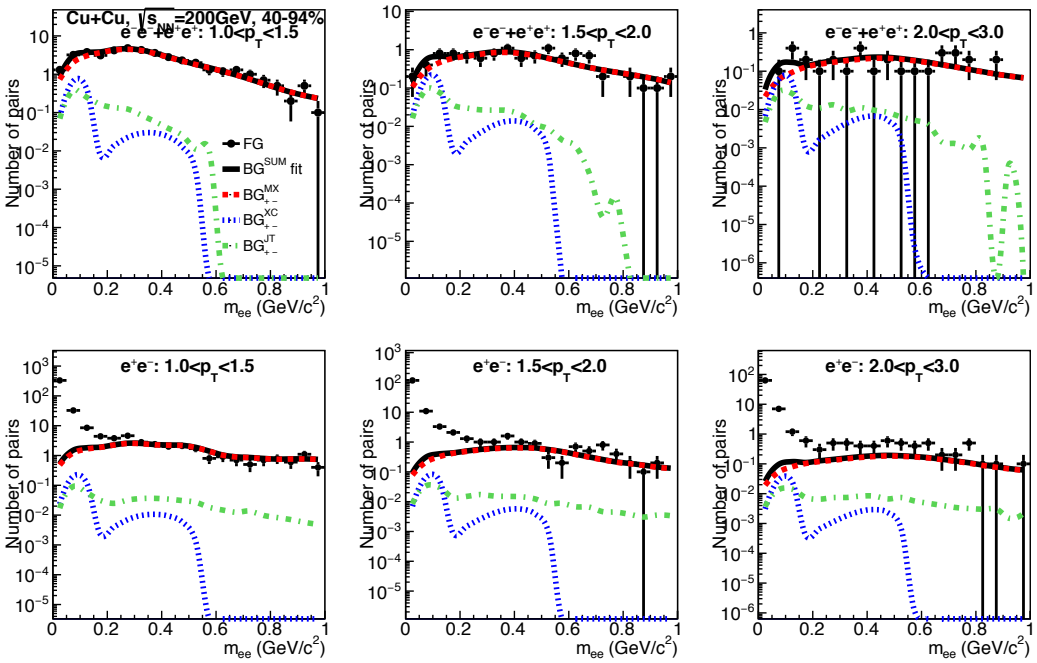

Figure 3.18: Like-sign and unlike-sign electron-pair invariant-mass distributions of the data together with evaluated backgrounds for Cu+Cu 40–94% centrality events.

unlike-sign pairs have different detector acceptance. Therefore, the like-sign foreground distribution corrected with the detector acceptance can reproduce the unlike-sign background distribution completely. However, this approach has a statistical limitation that occurs by the experimental data statistics; hence, we employ the method as a cross-check for the background estimation. We compare the reproduced background shape for unlike-sign electron pairs, $\mathrm{BG}_{+-}^{\mathrm{sum}}$, from the simulation-based approach to the background reproduced by the data-driven approach.

The unlike-sign background can be made inferences from the like-sign foreground pairs. The relative detector acceptance is different between the combination of electric-charge sign pairs because the particle trajectory's curvature depends on their charge. Therefore, the acceptance correction must be considered to reproduce the unlike-sign background from the like-

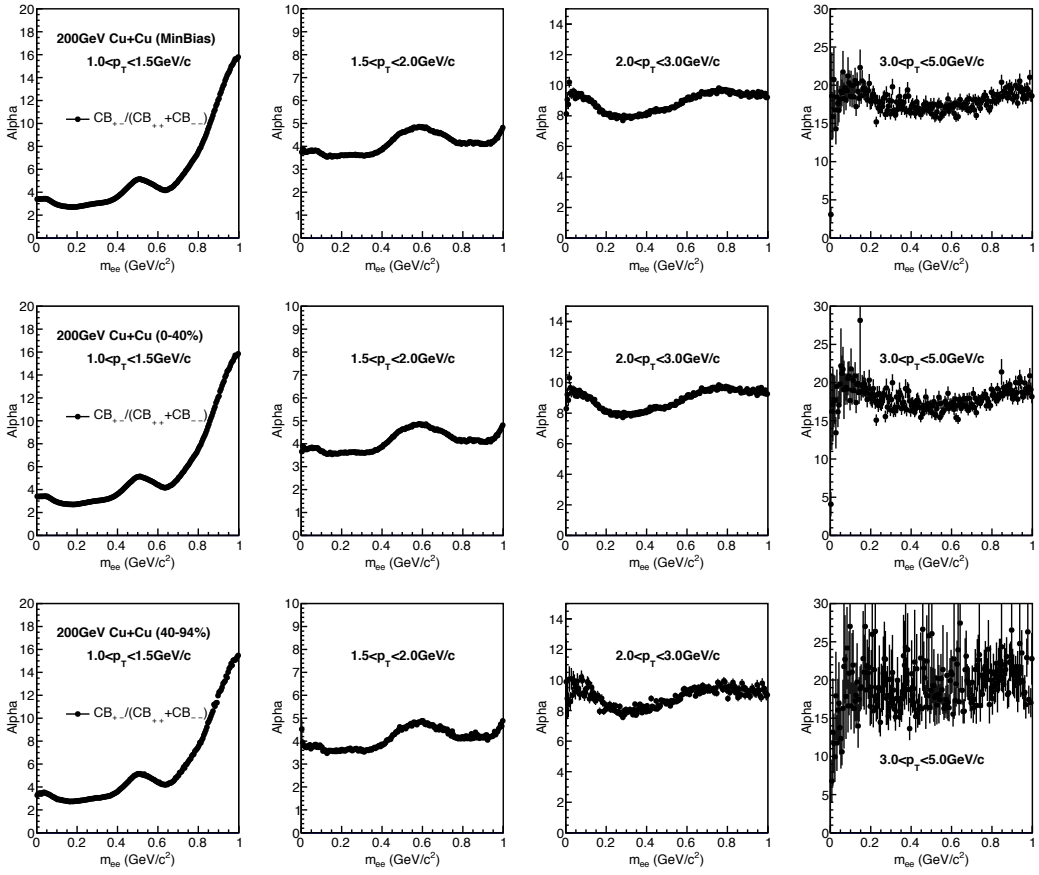

Figure 3.19: Acceptance correction factor α as a function of electron-pair invariant mass for each transverse momentum and centrality

sign pairs. The correction factor α is express as

$$\mathrm{BG}^{\mathrm{sum}}_{+-} = \alpha_{\mathrm{acc.}} \left(\mathrm{FG}_{++} + \mathrm{FG}_{--}\right). \tag{3.33}$$

The background in unlike-sign pairs is reproduced by multiplying the sum of like-sign foregrounds by the acceptance-correction factor. The α factor is calculated as the ratio of like- and unlike-sign pairs in mixed pairs evaluated in Sec. 3.9.1, and it is represented as

$$\alpha_{\mathrm{acc}} = \frac{\mathrm{BG}^{\mathrm{CM}}{}_{+-}}{\mathrm{BG}^{\mathrm{CM}}{}_{++} + \mathrm{BG}^{\mathrm{CM}}{}_{--}}. \tag{3.34}$$

The acceptance-correction factors, α, for each transverse momentum range are evaluated as a function of electron-pair invariant mass. The factors are calculated as a function of the invariant mass in this analysis, although the detector acceptance naturally depends on both invariant mass and transverse momentum. We confirm that $\alpha(m_{ee})$ is enough for the acceptance correction, not $\alpha(m_{ee}, p_T)$ with the simulation. To confirm the $\alpha(m_{ee})$ factor works well, the Dalitz decay simulation for π^0 and η is adopted. We compare the invariant mass distributions produced in the simulation with the acceptance-corrected foreground, $\alpha(m_{ee})$FG, in like-sign pairs and the cross pairs, $\mathrm{BG}^{\mathrm{XC}}$. The $\alpha(m_{ee})$FG distribution reproduces the $\mathrm{BG}^{\mathrm{XC}}$ well. Therefore, we employ $\alpha(m_{ee})$ as the correction factor. Figure 3.19 shows the acceptance-correction factors for three centrality classes independently; minimum bias, 0–40%, and 40–94%. Figure 3.20 shows the invariant mass distributions for both like-sign and acceptance-corrected like-sign foreground pairs with three centrality classes. The acceptance-corrected distributions have been seen the shape modification around the 1 GeV/c^2 in $1.0 < p_T < 1.5$ GeV/c, as well as other transverse momentum ranges. These corrected distributions are employed for the cross-check described in the next section.

The background-subtracted distributions are obtained from the subtraction of acceptance-corrected like-sign distribution from the unlike-sign foreground distribution. Figure 3.21 shows the subtracted invariant-mass distribution, together with the unlike-sign foreground FG_{+-} and $\alpha(m_{ee})\mathrm{FG}_{++,--}$ for three centrality classes.

3.12 Cross-check for background evaluation

We validate the background distributions reproduced by the simulation-based approach using the data-driven approach as a cross-check. The evaluated background $\mathrm{BG}_{+-}^{\mathrm{SUM}}$ are compared with the acceptance-corrected like-sign foreground distributions, FG_{--} and FG_{++}.

The comparisons are shown in Figs. 3.22, 3.23, and 3.24 for minimum bias, 0–40%, 40–94% centrality events, respectively. The invariant mass distributions by both the simulation-based and the data-driven approaches are consistent within the statistical errors. The simulation-based approach yields a smaller statistical uncertainty than another one, especially at high transverse-momentum. Therefore, we employ the simulation-based approach to the background estimation in this study.

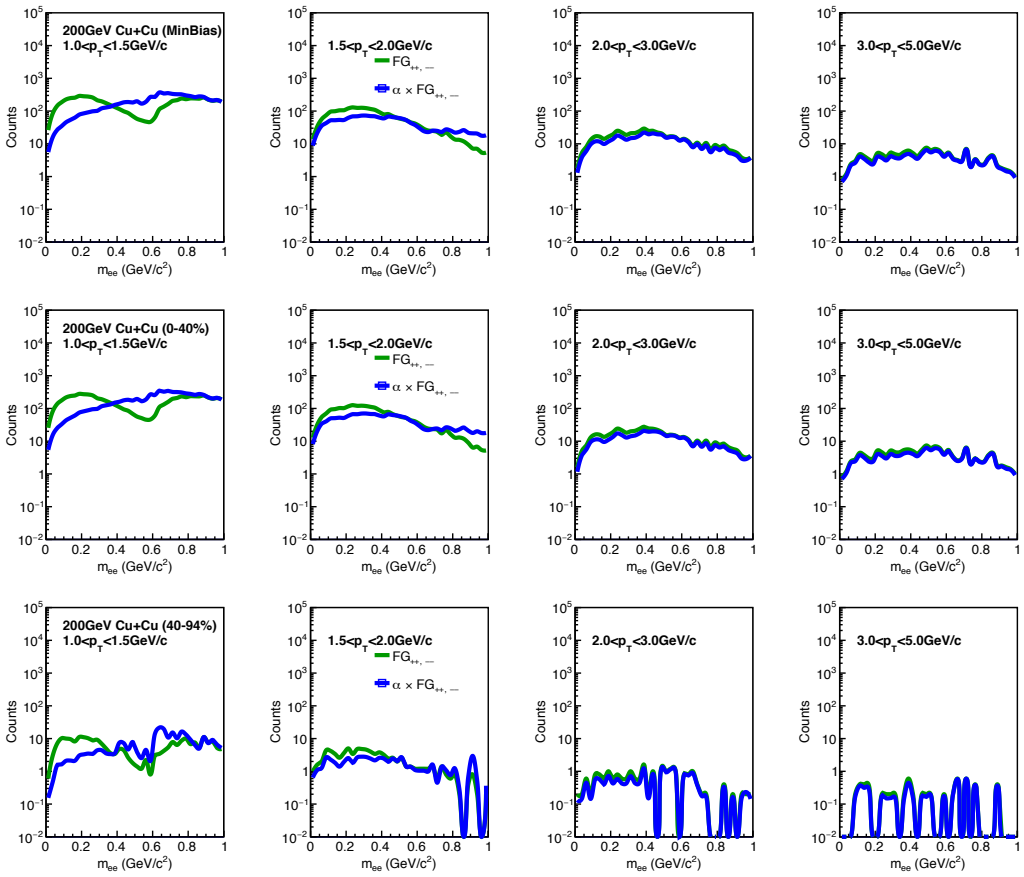

Figure 3.20: The invariant mass distributions for the like-sign foregrounds and their acceptance-corrected distributions in three centrality bins: (top) minimum bias, (middle) 0–40%, and (bottom) 40–94%.

3.13 Correlated pairs from hadronic decay

The hadron decay electron-pairs are the remaining background after subtracting the above combinatorial, jet-induced, and correlated cross pair backgrounds. The virtual photon signal is extracted as excess over the hadron decay pairs. This background source is the known hadron decays electron-pairs, which are correlated. The pairs are called hadronic cocktail or continuum. The cross pairs described in Sec. 3.9.3 are also originated from the hadron decays, but they are not physical pair, whereas the hadronic cocktail

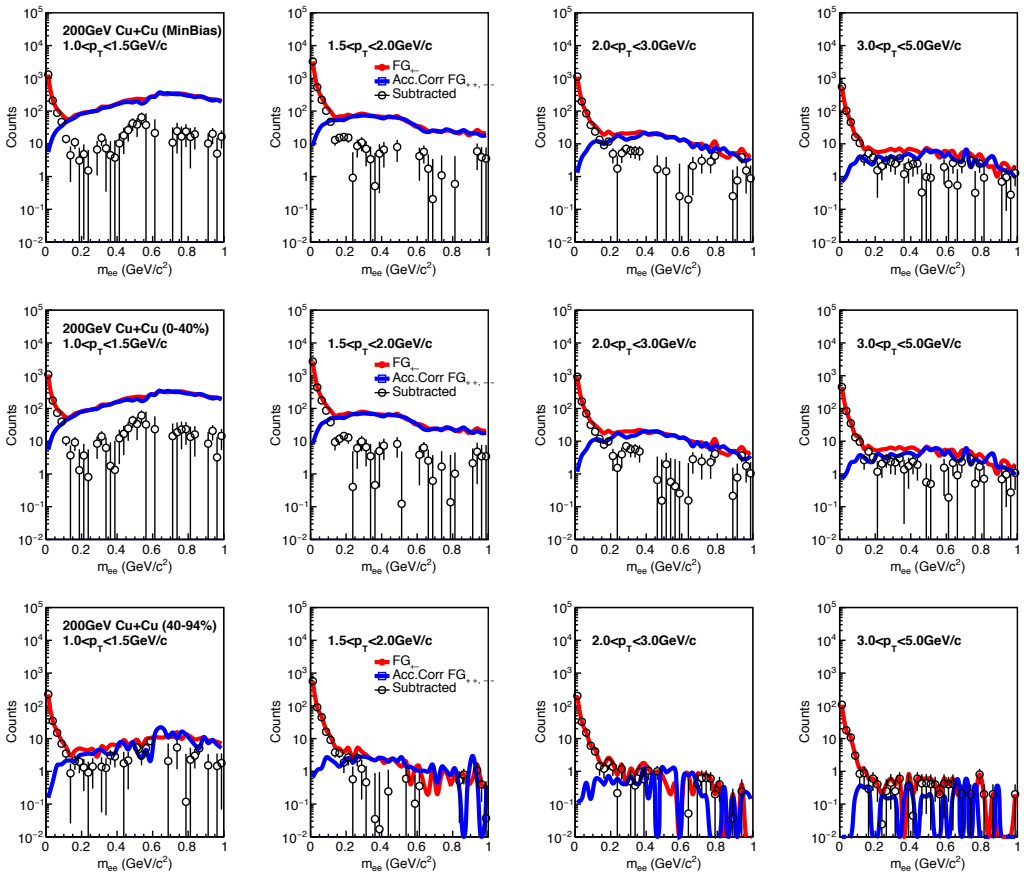

Figure 3.21: The invariant mass distribution of electron pairs for the unlike-sign foregrounds, the acceptance-corrected like-sign pairs, and the data after subtracting background by the data-driven approach with three centrality bins: (top) minimum bias, (middle) 0–40%, and (bottom) 40–94%.

is a physical pair.

The hadronic cocktail components are reproduced by EXODUS and PISA simulations, which are the same Monte Carlo simulation for evaluating the correlated cross-pair background in Sec. 3.9.3. The considered hadron decay modes are summarized in Table 3.6.

The PHENIX experiment has successfully reproduced the invariant yield of π^0 meson in 200 GeV Cu+Cu collisions. The modified Hagedorn function

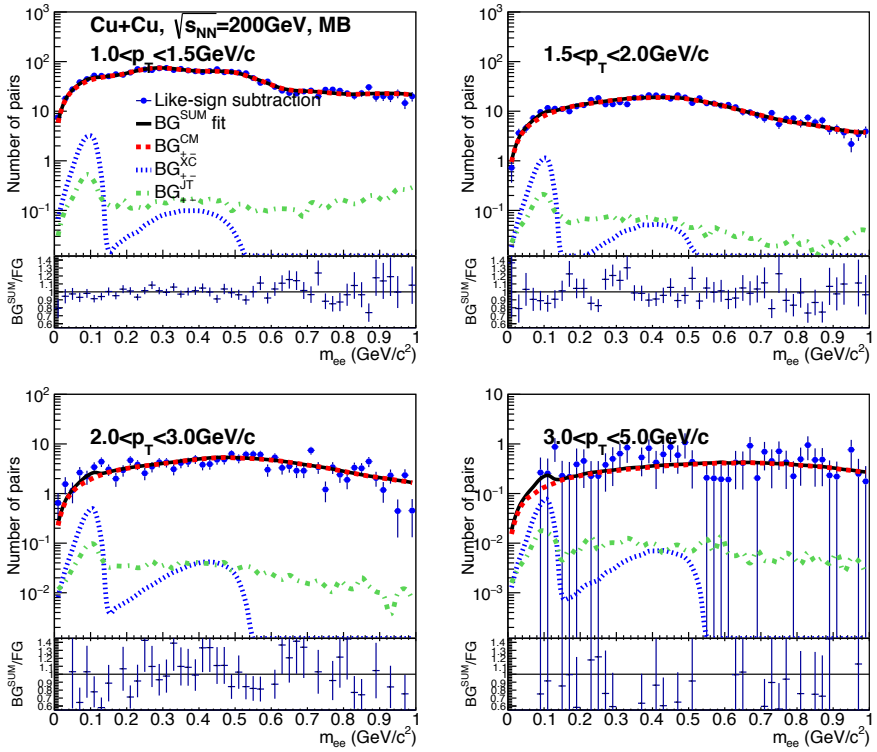

Figure 3.22: The comparison of invariant mass distributions between the acceptance-corrected foreground like-sign and $\mathrm{BG}^{\mathrm{SUM}}_{++,--}$ evaluated by the simulation-based approach with the $\mathrm{BG}^{\mathrm{SUM}}_{++,--}$/FG for Cu+Cu minimum bias events at $\sqrt{s_{NN}} = 200$ GeV.

can parametrize this invariant yield:

$$E\frac{d^3\sigma}{dp^3} = A\left(e^{-\left(ap_T+bp_T^2\right)} + p_T/p_0\right)^{-n}. \tag{3.35}$$

The transverse invariant-mass scaling generates the invariant yield of other hadrons, and it can be express as:

$$E\frac{d^3\sigma}{dp^3} = A\left(e^{-1(a\sqrt{m_T^2-m_{\pi^0}^2}+b(m_T^2-m_{\pi^0}^2)}) + \sqrt{m_T^2-m_{\pi^0}^2}/p_0\right)^{-n}. \tag{3.36}$$

Table 3.9.3 lists the Hagedorn function parameters for Minimum Bias, 0–40%, and 40–94% centrality classes. It is important to note that the large

Table 3.6: Considered decay modes and their branching ratios [84] in the hadronic cocktail simulation by EXODUS

Mother particle	Decay modes	Branching ratio %
π^0	$\pi^0 \to \gamma + e^+e^-$	1.174
	$\pi^0 \to e^+e^- + e^+e^-$	3.34×10^{-3}
η	$\eta \to \gamma + e^+e^-$	6.90×10^{-1}
	$\eta \to e^+e^- + e^+e^-$	2.40×10^{-3}
ω	$\omega \to e^+e^-$	7.28×10^{-3}
	$\omega \to \pi^0 + e^+e^-$	7.7×10^{-2}
η'	$\eta' \to \gamma + e^+e^-$	9.0×10^{-2}
ϕ	$\phi \to e^+e^-$	2.954×10^{-2}
	$\phi \to \eta + e^+e^-$	1.15×10^{-2}
ρ	$\rho \to e^+e^-$	4.72×10^{-3}

Table 3.7: Meson to π^0 ratios and their uncertainties [85]

particle	η	ω	η'	ϕ	ρ
meson/π^0	0.48	0.90	0.25	0.40	1.00
uncertainty	$\pm$0.03	$\pm$0.06	$\pm$0.075	$\pm$0.12	$\pm$0.30

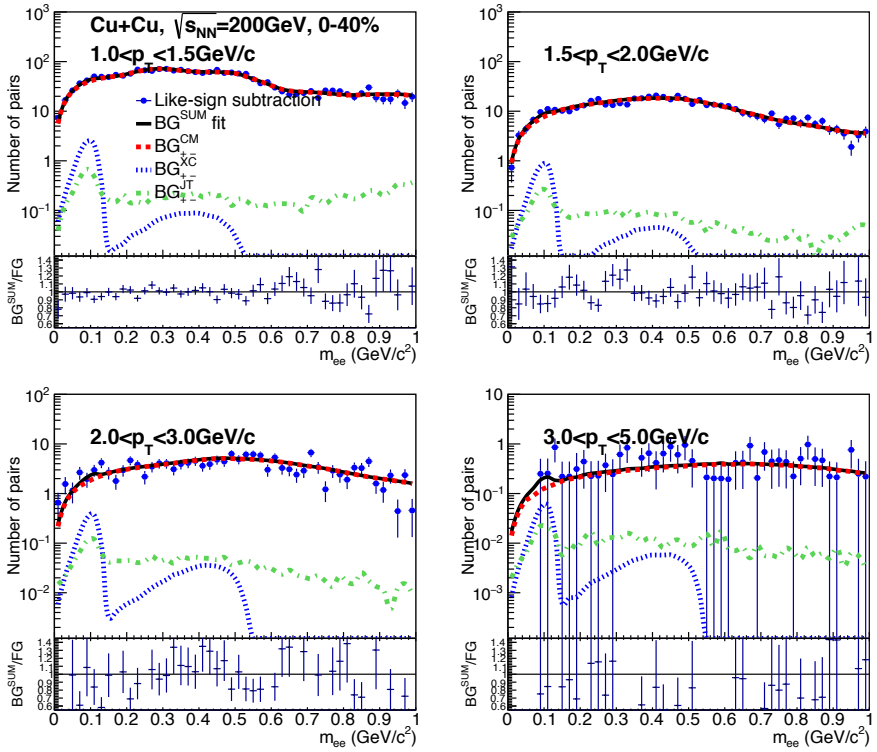

Figure 3.23: The comparison of invariant mass distributions between the acceptance-corrected foreground like-sign and $\mathrm{BG}^{\mathrm{SUM}}_{++,--}$ evaluated by the simulation-based approach with the $\mathrm{BG}^{\mathrm{SUM}}_{++,--}$/FG for Cu+Cu 0–40% centrality events at $\sqrt{s_{NN}} = 200$ GeV.

uncertainty in the absolute scale parameter A does not affect the extraction of direct virtual-photon component because the shape of the hadronic cocktail is only entered into the determination.

Once the function evaluates the hadron transverse-momentum spectra, electron pair spectra originated from the hadrons can be given by decay kinematics and branching ratios implemented in the EXODUS simulation.

Generated electrons arisen from hadron decays in EXODUS are passed through the PHENIX GEANT3 simulation, PISA, to simulate detector response and consider the detector acceptance. The same electron identification and pair-cuts are applied, and electron-pair invariant-mass distributions are reproduced. The relative scale between hadrons is normalized by the

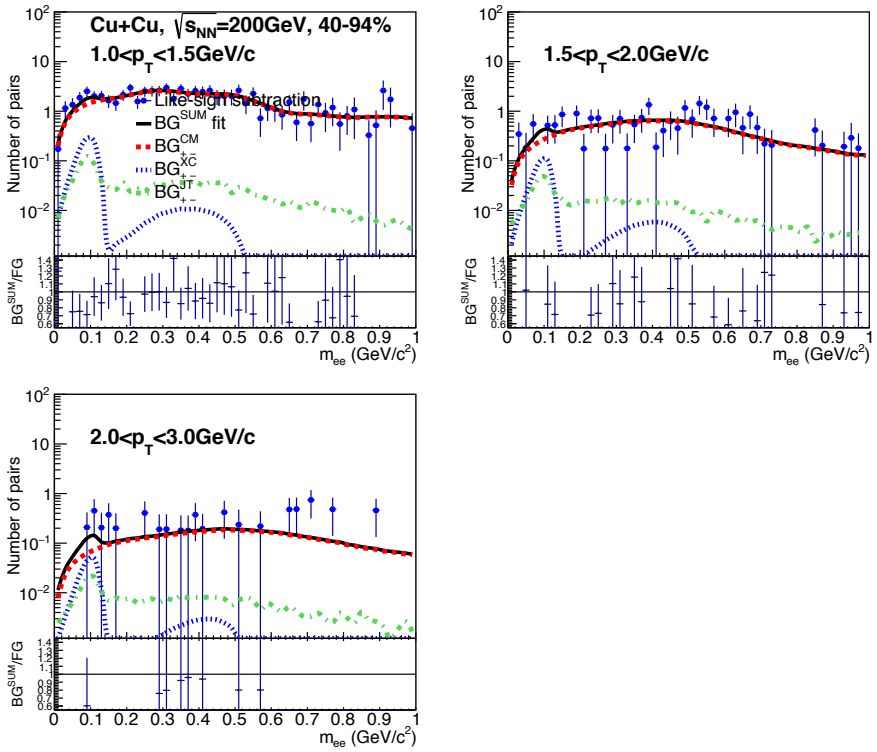

Figure 3.24: The comparison of invariant mass distributions between the acceptance-corrected foreground like-sign and $BG^{SUM}_{++,--}$ evaluated by the simulation-based approach with the $BG^{SUM}_{++,--}$/FG for Cu+Cu 40–94% centrality events at $\sqrt{s_{NN}} = 200$ GeV.

meson-to-pion ratios listed in Table 3.7 and branching ratios listed in Table 3.6.

The invariant mass distribution of simulated electron-pair from known hadron decays are merged as a hadronic cocktail shown in Fig. 3.25. The cocktail distribution is represented in a solid black line, while each component is expressed in colored lines.

3.14 Open heavy flavor contribution

An additional background contribution is open heavy flavor decays that produce correlated electron pairs. It is a semi-leptonic decay of charm hadrons,

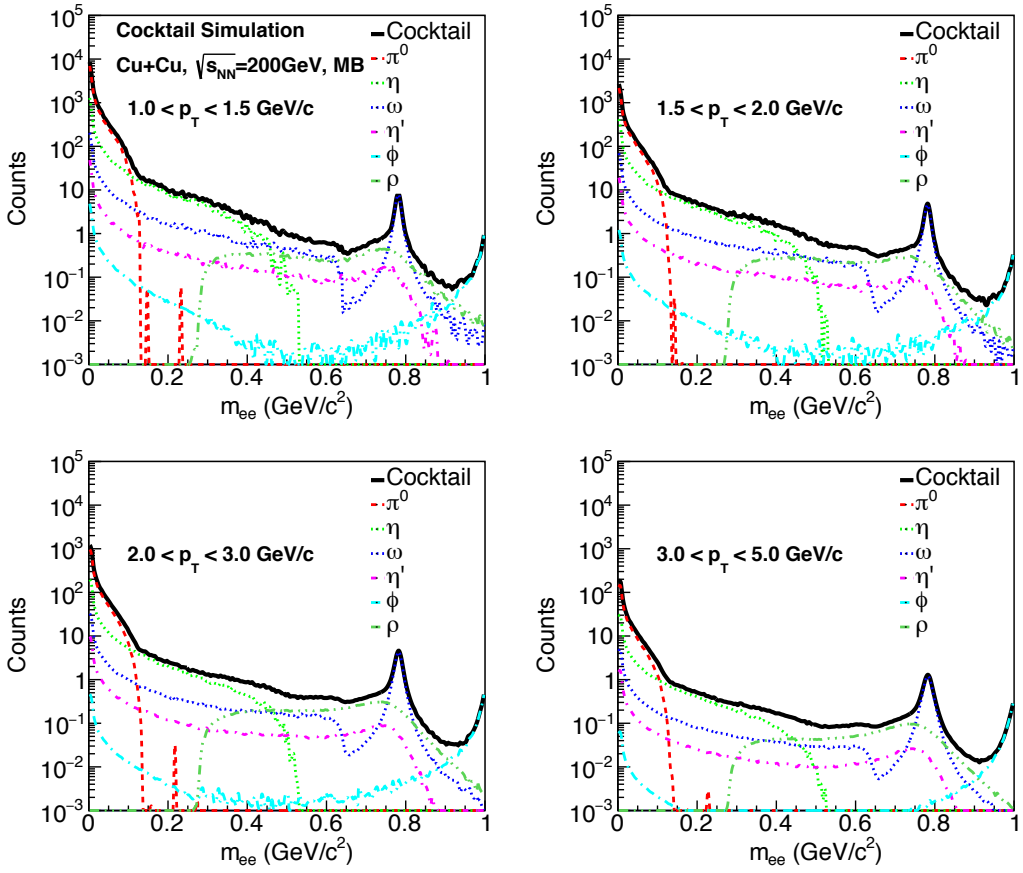

Figure 3.25: The invariant mass shape of a hadronic cocktail evaluated by the EXODUS and PISA simulation for $\sqrt{s_{NN}} = 200$ GeV Cu+Cu collisions. The black lines represent the summed shape of cocktail components. The colored dashed lines express each cocktail components from π^0 to ρ meson.

and the contribution is the so-called $c\bar{c}$ contribution.

The PYTHIA and PISA simulations evaluated the open heavy flavor contribution for the p+p collision system condition. The evaluated contribution is scaled by the number of collisions $N_{\rm coll}$ by the d+Au results [83]. The $c\bar{c}$ contribution and the background-subtracted invariant mass distributions are shown in Fig. 3.26. The contribution is small and hiding behind the hadronic cocktail in the invariant mass region interested in this study below $m_{ee} = 0.3$ GeV/c^2. The $c\bar{c}$ contribution becomes dominant in the high invariant-mass

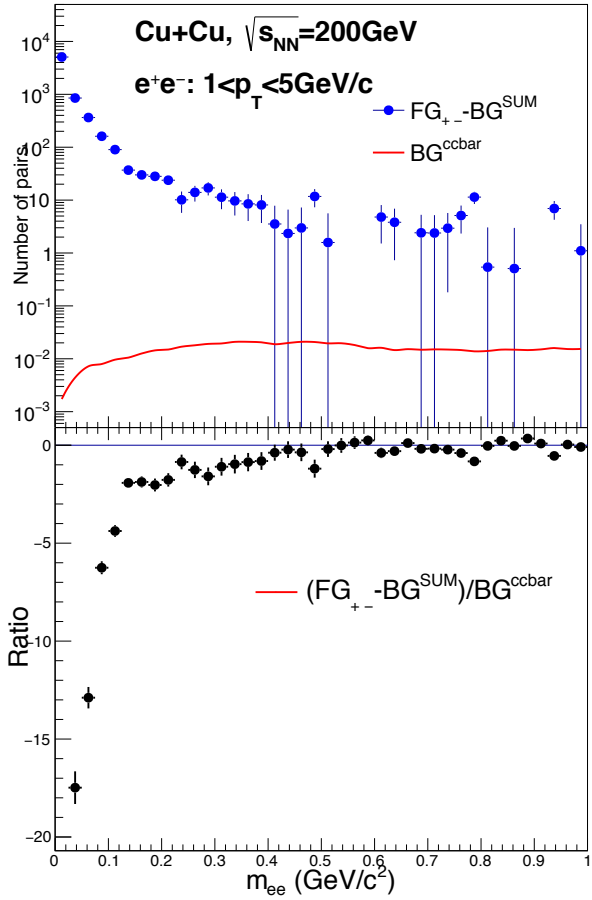

Figure 3.26: The evaluated $c\bar{c}$ contribution together with the background subtracted distribution

region due to their large opening angle. The contribution is less than 0.1% at most in the mass region $m_{ee} < 0.3$ GeV/c^2, even if the 100% uncertainty from the model dependence is considered.

3.15 Determination of direct photon fraction

In this section, we describe the extraction of the direct virtual-photon signal. The virtual photon composition is extracted as an excess over the hadronic cocktail after subtracting the background components.

Virtual photons are measured by fitting on the invariant mass spectra of electron pairs for $0.12 < m_{ee} < 0.3$ GeV/c^2 which is almost above the neutral pion invariant-mass. The very low mass region is derived from neutral pions; therefore, the signal-to-background ratio can be improved in the intended mass region.

The fit function on the invariant mass spectra is given by

$$f_{\mathrm{FG}}\left(m_{ee}\right) = \left(1 - r_{\gamma}\right) f_{c}\left(m_{ee}\right) + r_{\gamma} f_{\mathrm{dir}}\left(m_{ee}\right) + f_{\mathrm{BG}}\left(m_{ee}\right) \tag{3.37}$$

where r_{γ} is the only fit parameter which is called direct photon fraction, f_c and f_{BG} are the hadronic cocktail invariant-mass shape and the fixed contribution $\mathrm{BG}^{\mathrm{SUM}}$, respectively, and f_{dir} is the expected mass shape of direct photons. The invariant mass shape of f_c and f_{dir} is independently normalized to the foreground in the invariant mass < 30 MeV/c^2.

A similar fitting procedure is employed in the previous studies, although there are a few differences. In the previous studies, the fit function is given by

$$f_{\mathrm{FG-BG}}\left(m_{ee}\right) = \left(1 - r_{\gamma}\right) f_{c}\left(m_{ee}\right) + r_{\gamma} f_{\mathrm{dir}}\left(m_{ee}\right). \tag{3.38}$$

The hadronic cocktail is only included in the function since the $\mathrm{BG}^{\mathrm{SUM}}$ and the open heavy flavor contributions are subtracted before the fit. Moreover, the fit in this study is applied by a log-likelihood fit in order that the fitting works correctly even though limited statistics, especially at higher transverse momentum region.

The relation between real photon and the associated electron pair productions can be expressed as

$$\frac{dN^2}{dm_{ee}dp_T} = \frac{2\alpha}{3\pi}\frac{1}{m_{ee}}\sqrt{1 - \frac{4m_e^2}{M_{ee}^2}}\left(1 + \frac{2m_e^2}{M_{ee}^2}\right) S\left(m_{ee}, p_T\right)\frac{dN_{\gamma}}{dp_T} \tag{3.39}$$

where α is the fine structure constant, and $S\left(m_{ee}, p_T\right)$ is a process-dependent factor. The factor $S\left(m_{ee}, p_T\right)$ took account of differences between real photon and virtual photon productions, such as form factors and phase space. $S\left(m_{ee}, p_T\right)$ becomes negligible in the high transverse momentunm ($p_T \gg m_{ee}$), and the factor becomes 1 as $m_{ee} \to 0$. In addition, the electron pair invariant

mass M_{ee} should be greater than electron mass m_e. Therefore, Equation 3.41 can simplifies as

$$\frac{dN^2}{dm_{ee}} \simeq \frac{2\alpha}{3\pi}\frac{1}{M_{ee}}\frac{dN_\gamma}{dp_T}. \tag{3.40}$$

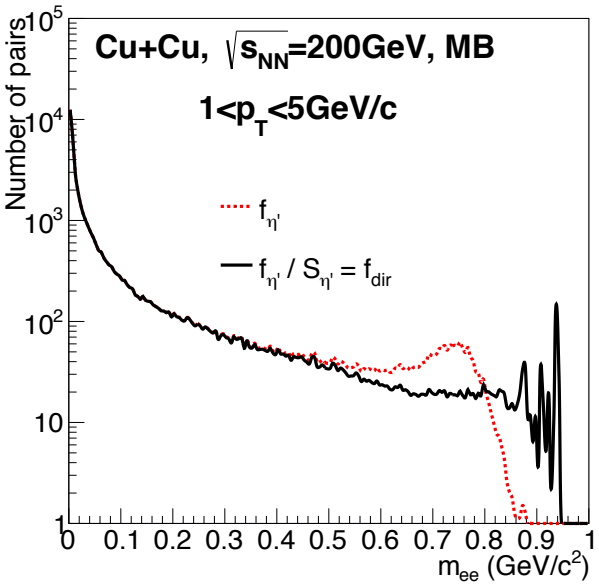

Figure 3.27: The expected invariant-mass shape for direct virtual photon in Cu+Cu collisions at $\sqrt{s_{NN}}$ = 200 GeV. The expected shape is calculated using η' in the hadronic cocktail simulation.

The direct virtual photon's mass-shape is evaluated using the η' Dalitz-decay component in the cocktail simulation. The decay rate of Dalitz decay for pseudo-scaler mesons can be expressed by

$$\frac{dN^2}{dm_{ee}dp_T} = \frac{2\alpha}{3\pi}\frac{1}{m_{ee}}\sqrt{1-\frac{4m_e^2}{M_{ee}^2}}\left(1+\frac{2m_e^2}{M_{ee}^2}\right)|F\left(m^2\right)|\left(1-\frac{m^2}{M_h^2}\right)^3\left(m_{ee},p_T\right)\frac{dN_\gamma}{dp_T} \tag{3.41}$$

where $S\left(m_{ee},p_T\right) = |F\left(m^2\right)|\left(1-\frac{m^2}{M_h^2}\right)^3$, and $\left(1-\frac{m^2}{M_h^2}\right)^3$ term in $S\left(m_{ee},p_T\right)$ is a suppression factor which arises due to the finite invariant mass of the

parent particles [86]. Therefore, the mass shape for the virtual photons can be evaluated by

$$f_{\rm dir}\left(m_{ee}\right) = f_{\eta'}\left(m_{ee}\right)/S_{\eta'}\left(m_{ee}\right). \tag{3.42}$$

The expected invariant-mass shape for direct virtual-photons together with the η' meson are shown in Fig. 3.27.

Figures 3.28, 3.29, and 3.30 show the electron pair invariant mass distributions with the fit results by Eq. 3.37 for minimum bias, 0–40%, and 40–94% centralities, respectively. The black markers represent the measured foreground electron pairs, and the shaded red regions are the evaluated background distribution. The hadronic cocktail distribution are represented by the dotted blue lines, while the fit results are shown by the solid red lines. The fit for mass distributions are performed within an invariant mass range $0.1 < m_{ee} < 0.3$ GeV/c^2 for several transverse momentum bins separately.

Direct photon fractions expected by a next-to-leading-order (NLO) perturbative-quantum-chromodynamics (pQCD) calculation are compared to the data. The definition of the direct photon fraction in which all contributions arise from the pQCD processes are expressed by

$$r_\gamma = \frac{N_{\rm pQCD}}{N_{\rm inclusive}} = \frac{N_{\rm pQCD}}{N_{\rm decay} + N_{\rm pQCD}}. \tag{3.43}$$

The expectations from NLO pQCD calculation for Cu+Cu collisions are calculated by the $N_{\rm coll}$ scaling, and it is given by

$$r_\gamma^{\rm centrality} = \frac{N_{\rm pQCD}\left(N_{\rm coll}^{\rm centrality}/N_{\rm coll}^{\rm Min.Bias}\right)}{N_{\rm decay}^{\rm centrality} + N_{\rm pQCD}\left(N^{\rm centrality}/N_{\rm coll}^{\rm Min.Bias}\right)}, \tag{3.44}$$

where $N_{\rm pQCD}$ is given by

$$N_{\rm pQCD} = \frac{r_\gamma^{\rm Min.Bias}}{1 - r_\gamma^{\rm Min.Bias}} N_{\rm decay}, \tag{3.45}$$

and $N_{\rm decay}$ denotes decay photon invariant yields evaluated by the Monte Carlo simulations described in the below section.

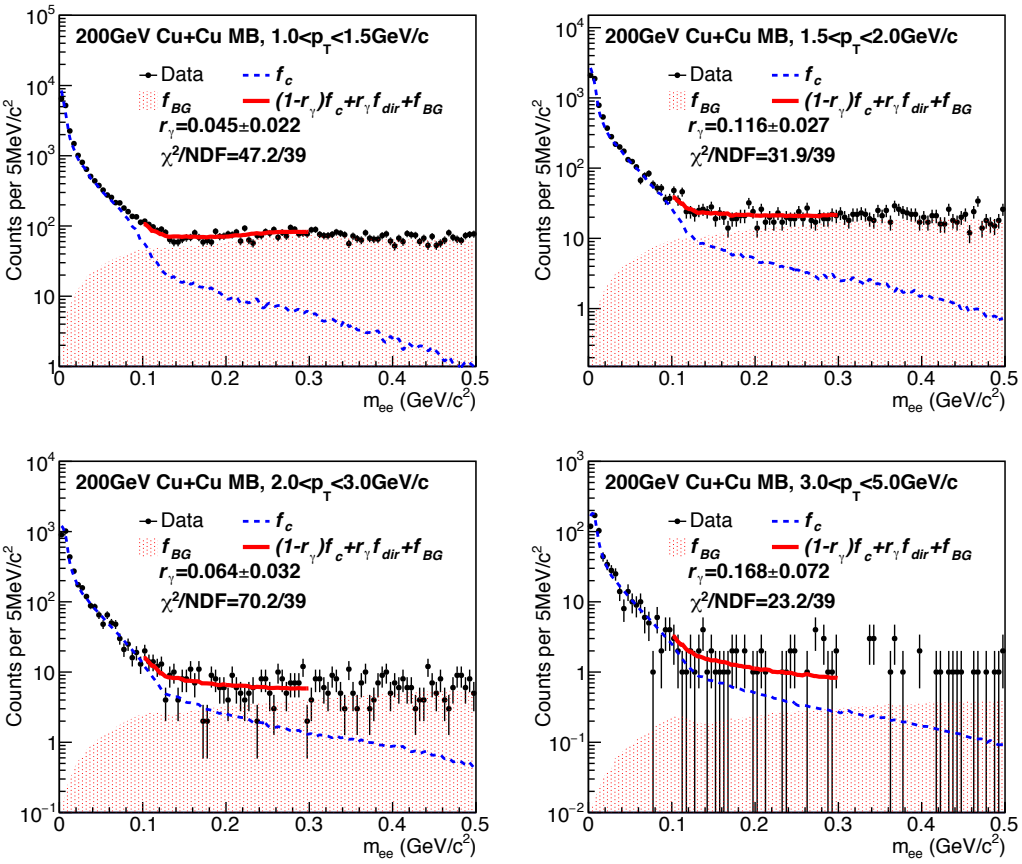

Figure 3.28: The e^+e^- pair mass distributions in Cu+Cu Minimum Bias collisions for four transverse momentum regions. The data (closed circles), the fit function (red curve), hadronic contribution (blue curve), and the background $\mathrm{BG}^{\mathrm{SUM}}$.

3.16 Systematic uncertainties

In this section, we describe the possible sources of systematic errors and explain how to evaluate the uncertainties. We take into account the following sources of systematic uncertainties.

- Background normalization
- Particle composition in hadronic cocktail

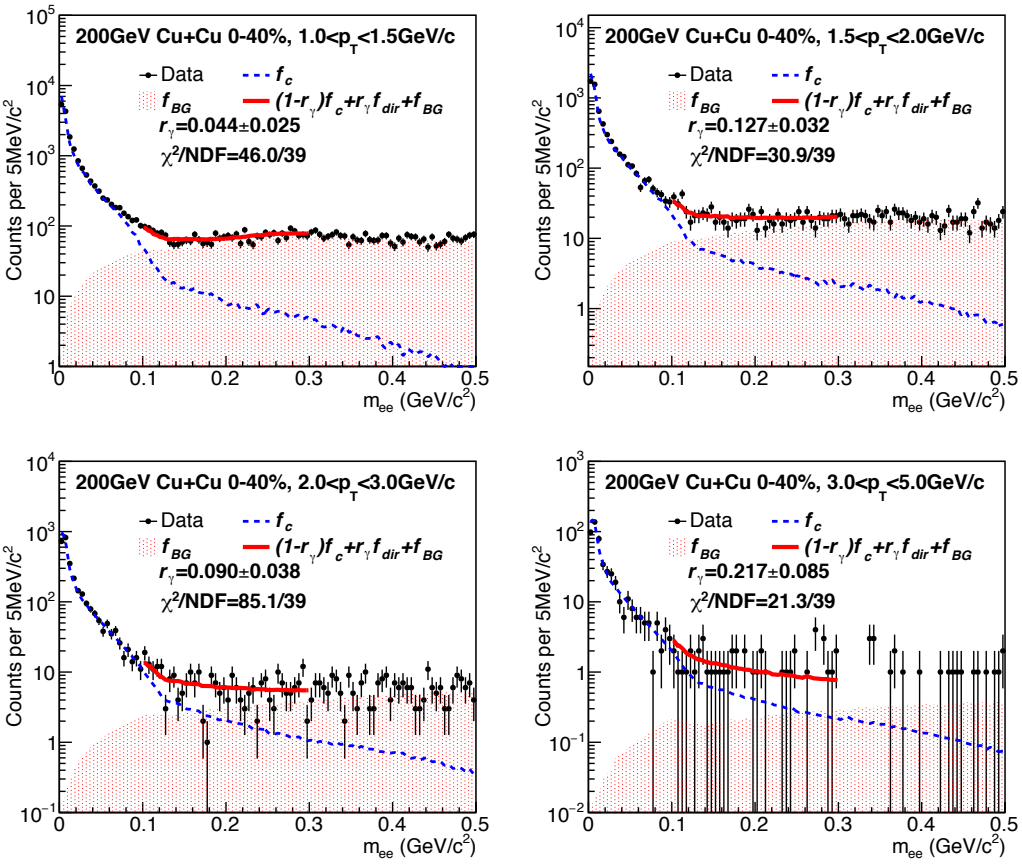

Figure 3.29: The e^+e^- pair mass distributions in Cu+Cu 0–40% collisions for four transverse momentum regions. The data (closed circles), the fit function (red curve), hadronic contribution (blue curve), and the background $\mathrm{BG}^{\mathrm{SUM}}$.

- Hadronic cocktail normalization
- Fitting range for r_γ calculation

Each systematic uncertainty is obtained from the Root-Mean-Square error of the results in the direct photon fractions, r_γ.

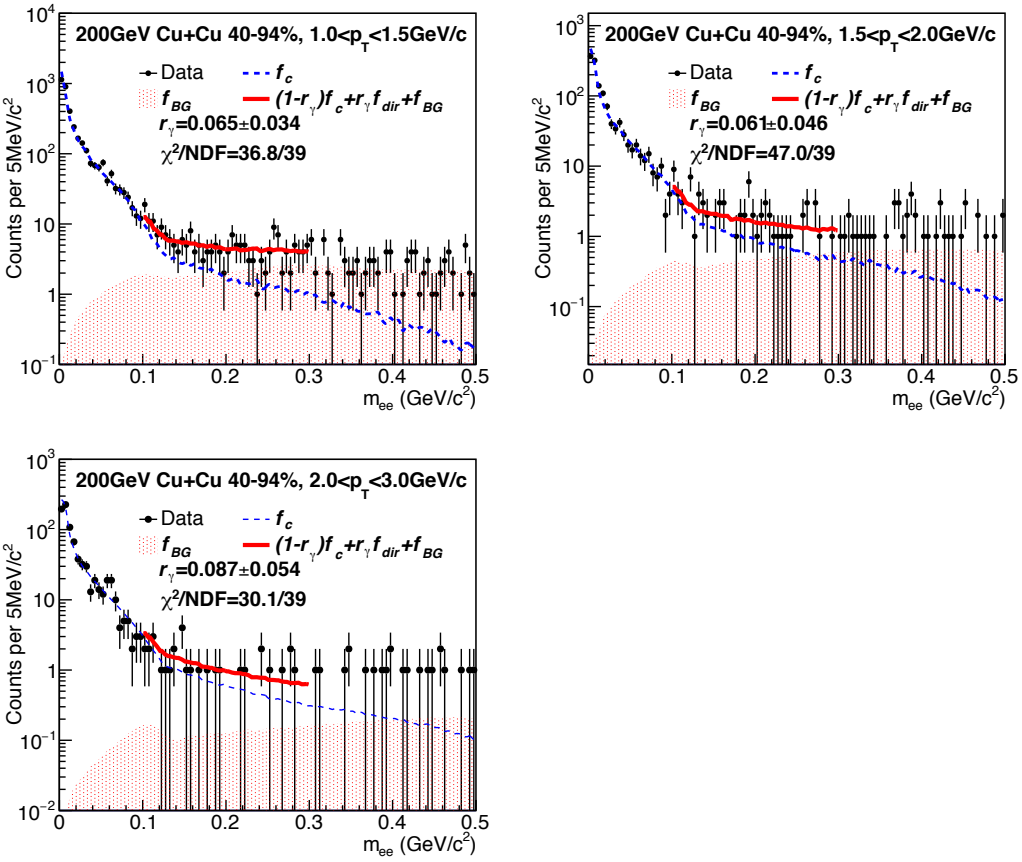

Figure 3.30: The e^+e^- pair mass distributions in Cu+Cu 40–94% collisions for three transverse momentum regions. The data (closed circles), the fit function (red curve), hadronic contribution (blue curve), and the background $\mathrm{BG}^{\mathrm{SUM}}$.

3.16.1 Background normalization uncertainties

First systematic uncertainty is in the background normalization of the four-component fit. The normalization factors of background components lead to a systematic error. To evaluate the systematic error related to the normalization, we vary the fitting parameters one by one to shift $\pm$ 1 sigma.

The uncertainty evaluation procedure is as follows: First of all, we shift one of the fitting parameters obtained from the four-component fit by one sigma. Second, shifted parameters are fixed, and a three-component fit is

applied to the invariant-mass foreground distribution. Third, we subtract the background and compare the cocktail distribution to evaluate the direct photon fraction. Lastly, the above processes are repeated for all of the fitting parameters.

3.16.2 Particle composition uncertainties

The second systematic uncertainty is particle composition, which is the uncertainty of neutral pion to meson ratios. We need to estimate the impact of the ratio uncertainties on the results.

We evaluate the systematic error with the following procedure. First, we shift one ratio by $\pm 1\sigma$ from the nominal ratio and create a cocktail distribution. Secondly, we calculate r_γ with the obtained cocktail distribution. Finally, we repeat the above processes for all meson to neutral pion ratios. This procedure is employed independently to the collision centrality. Table 3.7 shows the meson to neutral pion ratios with uncertainty. We employ the ratios and uncertainties for this systematic error estimation.

3.16.3 Uncertainty in hadronic cocktail normalization

The hadronic cocktail normalization is the other origin of systematic error. We use the invariant mass region of 0.03 GeV/c^2 as the nominal normalization region. The low mass region of the electron-pair invariant-mass is dominantly originated from π^0 Dalitz decays, and electron pairs are affected by the finite mass resolution. Therefore, it is crucial to evaluate the effect of the normalization region.

To evaluate the systematic error, we vary the mass region for the normalization. The evaluation procedure is as follows: Firstly, we apply the 0.03$\pm$0.01 GeV to the cocktail normalization. Then, we calculate r_γ with the normalized cocktail distribution. This procedure is employed independently to the collision centrality.

3.16.4 Uncertainty in the fitting range for r_γ

The final source of systematic uncertainty is the fitting range of r_γ. This fitting is for the extraction of direct photon fraction. The nominal fitting range in the invariant mass distribution is $0.12 < m_{ee} < 0.3$ GeV/c^2, but this range may affect the direct photon fraction.

To evaluate the fitting's uncertainty, we shift the upper and lower limit of the fitting range slightly and apply the six kinds of fitting ranges in the invariant mass distributions. We calculate the r_γ in each fitting range and estimate the systematic error.

3.16.5 Summary of systematic uncertainties

We explain the four kinds of systematic errors in the above subsections. We evaluate the total systematic error by calculating the Root Mean Square Error of these four uncertainties. The total systematic errors are calculated for each transverse momentum bin and centrality class.

Chapter 4

Results and Discussion

4.1 Direct photon fraction

Direct photon fractions have been measured by the virtual photon method in Cu+Cu collisions at $\sqrt{s_{NN}} = 200$ GeV. The results are presented as a function of transverse momentum for three centrality bins: minimum bias, 0–40%, and 40–92% centrality events. The direct photon fractions are obtained as excess over the hadronic cocktail as described in the previous chapter.

Figure 4.1 shows the direct photon fractions r_γ for three centrality bins. The data points are presented with both statistical and systematic uncertainties. The results are compared with the expectations by next-to-leading-order (NLO) perturbative-quantum-chromodynamics (pQCD) calculations with the three curves of the NLO pQCD calculations corresponding to the theory scales $\mu = 0.5p_T$, p_T, and $2.0p_T$. The direct photon fractions of the data exceed the NLO pQCD calculations, especially minimum bias and central collisions.

Comparison with other collision systems

The direct photon fraction has been measured by the virtual photon method in several collision systems at $\sqrt{s_{NN}} = 200$ GeV. Figure 4.2 shows direct photon fractions as a function of transverse momentum measured by the virtual photon method in p+p, d+Au, Cu+Cu, and Au+Au in minimum bias events. The error bars denote the statistical uncertainty, while the error boxes represent the systematic uncertainty. The data points are compared with the NLO pQCD calculations with three theoretical scales.

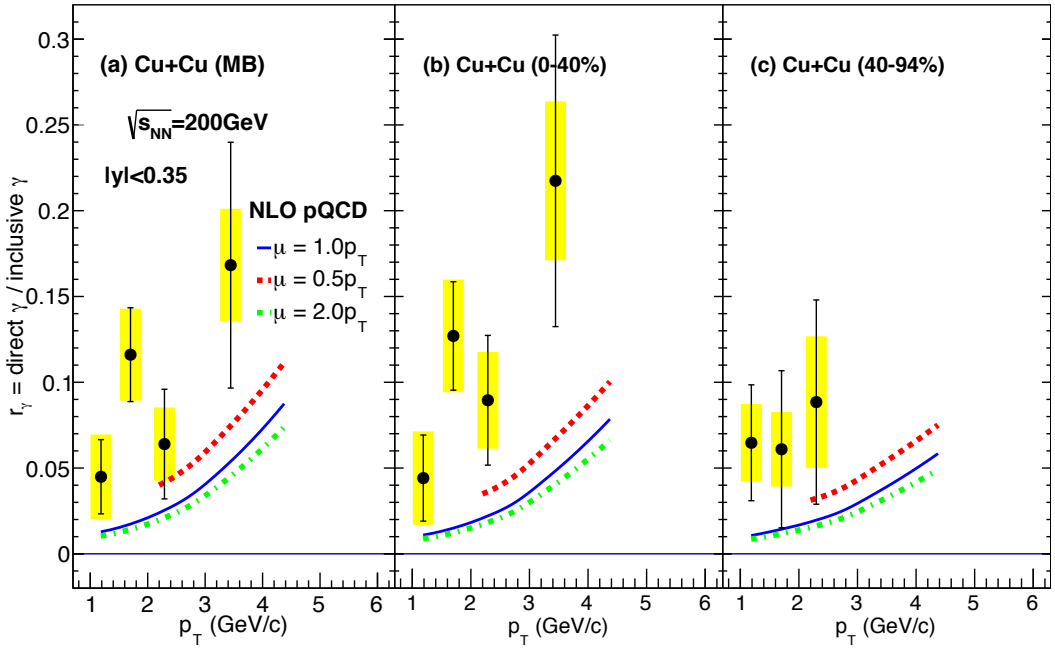

Figure 4.1: Direct photon fraction measured with the virtual photon method as a function of transverse momentum in Cu+Cu collisions at $\sqrt{s_{NN}} = 200$ GeV

The p+p and d+Au results show agreements with the NLO pQCD calculations, whereas the Cu+Cu and Au+Au results show excess over the theoretical expectations. Direct photons in small collision systems originate from initial hard scattering since the hot medium is not created in the collisions. In heavy-ion collision systems, there is a contribution of thermal radiation from the created medium. The excess in Cu+Cu collisions is more modest than that in Au+Au. It is possibly due to a smaller volume of the created matter.

4.2 Direct photon spectra

The direct photon spectra are calculated from the direct photon fractions and the decay photon yields. The decay photon yields are obtained from

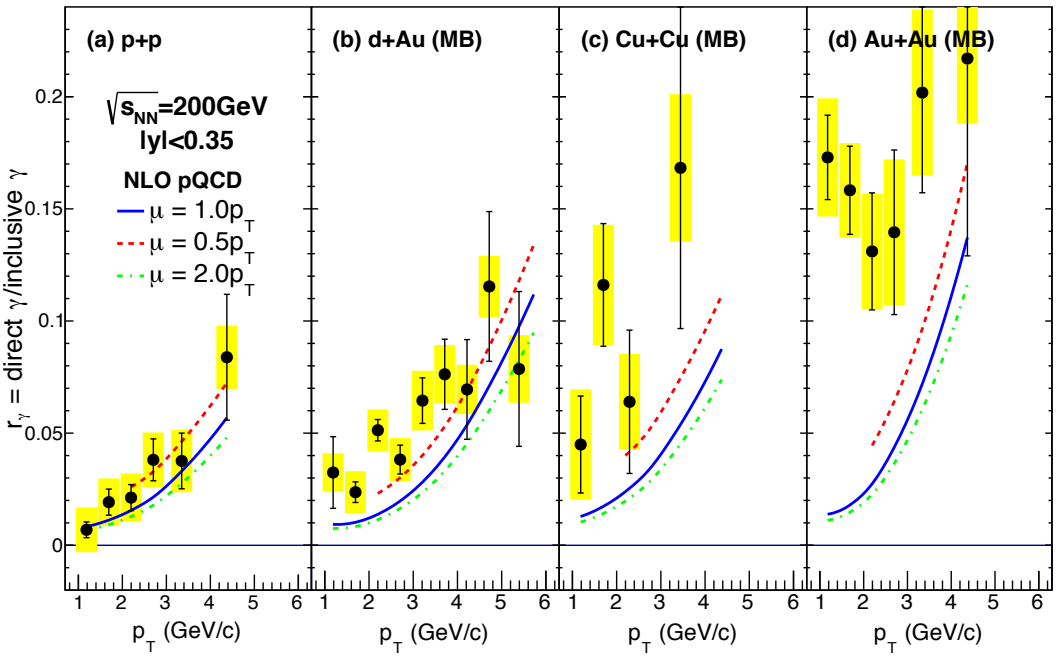

Figure 4.2: Direct photon fraction measured with the virtual photon method for different collision systems in $\sqrt{s_{NN}} = 200$ GeV: (a) p+p collisions [40], (b) d+Au collisions [40], (c) Cu+Cu collisions by this work, and (d) Au+Au collisions [39]. Expectations from NLO pQCD calculations [87] are also shown by curves.

the EXODUS simulation. EXODUS simulates the hadron decays with photons. The considered hadrons and their decay modes are tabulated in Table 4.1. The input shape of the transverse momentum distribution for the π^0 meson is a modified Hagedorn function, and the shapes for other mesons are obtained from the transverse invariant-mass scaling. The evaluated decay photon spectra for three centrality classes are shown in Fig. 4.3. The total decay photon spectra are denoted by the black line, while colored lines indicate decay photon contributions from each hadron decay.

Direct photon spectra are obtained by multiplying the direct photon frac-

Table 4.1: Considered hadrons and their decay modes in the decay photon simulation by EXODUS. Branching ratios are from the Particle Data Group [84].

Mother particle	Decay modes	Branching ratio
π^0	2γ	$(98.823 \pm 0.034)\%$
	γe^+e^-	$(1.174 \pm 0.035\%$
η	2γ	$39.41 \pm 0.20)\%$
	$\gamma\pi^+\pi^-$	$(4.22 \pm 0.88)\%$
	γe^+e^-	$(6.9 \pm 0.4) \times 10^{-3}$
	$3\pi^0$	$(32.68 \pm 0.23)\%$
	$\pi^0 2\gamma$	$(2.7 \pm 0.5) \times 10^{-4}$
ω	$\pi^+\pi^-\pi^0$	$(89.2 \pm 0.7)\%$
	$\pi^0 e^+e^-$	$(7.7 \pm 0.6) \times 10^{-4}$
	$\pi^0\gamma$	$(9.28 \pm 0.28)\%$
η'	2γ	$(2.20 \pm 0.08)\%$
	γe^+e^-	$< 9 \times 10^{-4}$
	$\omega\gamma$	$(2.75 \pm 0.23)\%$
	$\rho\gamma$	$(29.1 \pm 0.5)\%$
	$\pi^0\pi^0\eta$	$(22.2 \pm 0.8)\%$

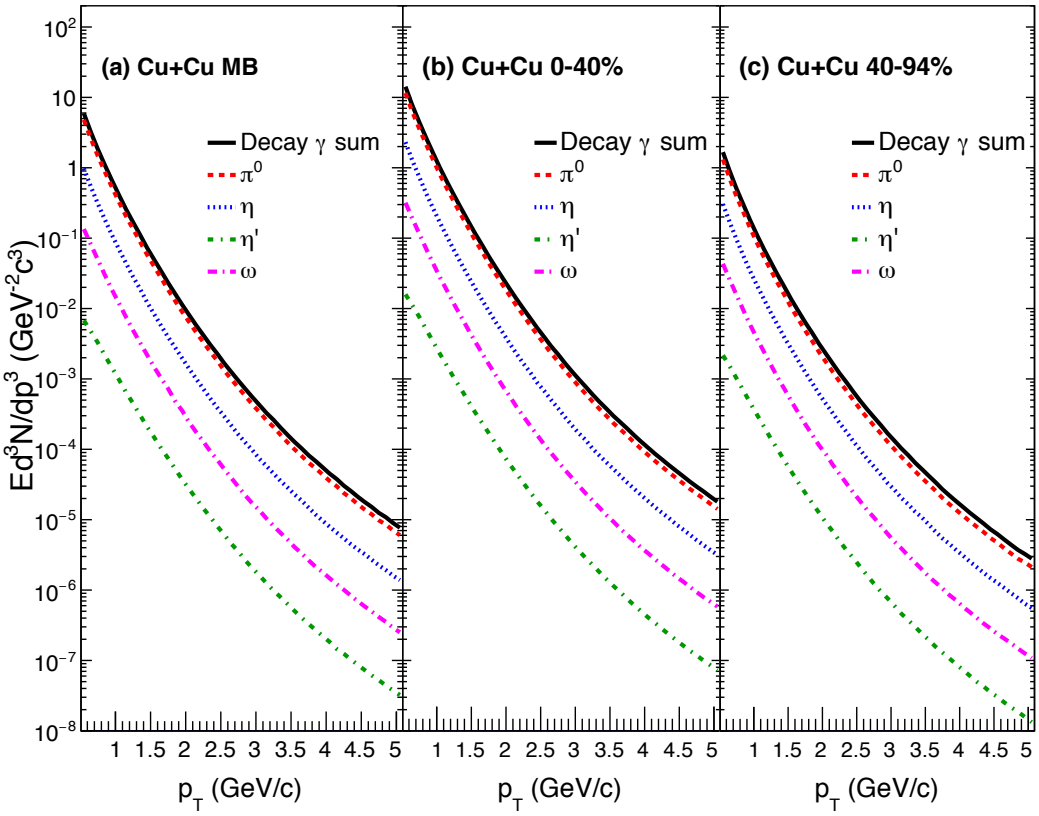

Figure 4.3: Decay photon spectra in Cu+Cu collisions at $\sqrt{s_{NN}} = 200$ GeV for minimum bias, 0–40%, and 40–94% centrality classes calculated by the EXODUS simulation.

tion by the decay photon spectrum. The calculation is given by:

$$\frac{dN^{\text{direct}\gamma}}{dp_T} = \frac{r_\gamma}{1 - r_\gamma} \frac{dN^{\text{decay}\gamma}}{dp_T} \tag{4.1}$$

where r_γ is the direct photon fraction defined by:

$$r_\gamma = \frac{\text{direct}\gamma}{\text{inclusive}\gamma}. \tag{4.2}$$

The direct photon invariant yield is obtained from the following equation:

$$E\frac{d^3N}{dp_T^3} = \frac{1}{2\pi p_T}\frac{dN_\gamma^{\rm direct}}{dp_T dy} = \frac{1}{2\pi p_T}\frac{1}{N_{\rm events}}\frac{N_\gamma^{\rm direct}}{\Delta p_T \Delta y} \tag{4.3}$$

where $N_{\rm events}$ is the number of events for each centrality, and Δp_T and Δy are the given transverse momentum and rapidity bin, respectively.

Figure 4.4 shows the direct photon spectra in Cu+Cu collisions at $\sqrt{s_{NN}} =$ 200 GeV for minimum bias, 0–40%, and 40–94% centralities. The direct photon spectrum in Cu+Cu minimum bias collisions is compared to the T_{AA} scaled p+p results and its parameterized function. The scaling parameter T_{AA} is evaluated from the Glauber calculations. The spectra in other centralities are compared with the parameterized function. The scaled p+p results [40] are parameterized by a modified power-law function $A_{pp}\left(1 + {p_T}^2/B_{pp}\right)^{n_{pp}}$. The fit function is an empirical parametrization, but it describes the p+p results well, especially at the low transverse-momentum region. The direct photon spectra in Cu+Cu collisions have a clear enhancement from the binary scaled p+p results.

Spectrum comparison with Au+Au collision system

The direct photon spectra in Cu+Cu collisions are compared to the Au+Au results at $\sqrt{s_{NN}} = 200$ GeV. The $N_{\rm part}$ in Cu+Cu 0–40% and 40–94% centralities are comparable to the Au+Au 40–60% and 60–92% centralities. The $N_{\rm part}$ of 0–40% and 40–94% centralities are 66.4 and 11.6, while those for Au+Au collisions are 56.0 (40–60%) and 12.5 (60–92%).

The spectra in Au+Au collisions are scaled by the $N_{\rm part}$ ratios, and the scaled spectra are shown with the open square markers in Fig. 4.4. The spectra in Cu+Cu collisions are consistent with the Au+Au results within the uncertainties.

Temperature estimation

It is known that the excess yield of the direct photon spectrum indicates the contribution from thermal photons arisen from Quark-Gluon Plasma; therefore, the inverse slope of the spectrum implies the effective temperature of the created matter. The spectrum is parameterized as:

$$A\exp\left(\frac{-p_T}{T}\right) + T_{AA}A_{pp}\left(1 + \frac{p_T^2}{B_{pp}}\right)^{n_{pp}}. \tag{4.4}$$

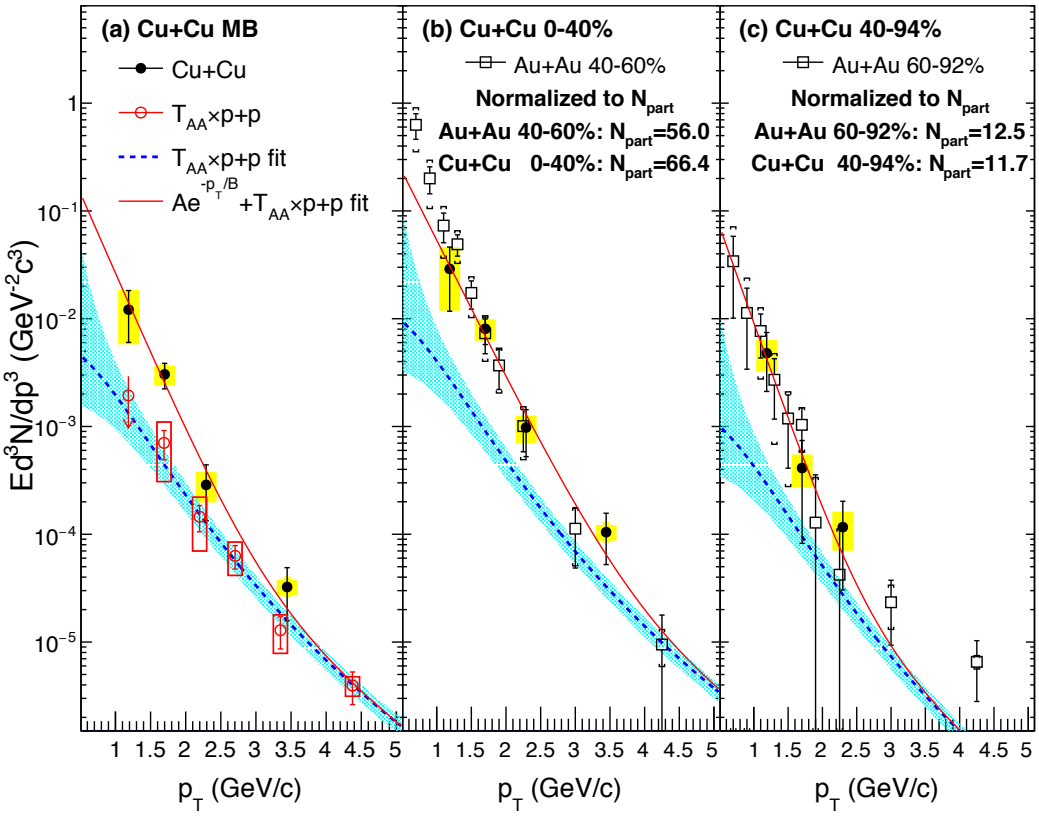

Figure 4.4: Direct photon spectra in Cu+Cu collisions for (a) minimum bias, (b) 0–40%, and (c) 40–94% centrality events. The Cu+Cu minimum bias result is shown together with the T_{AA} scaled p+p spectra and its fit results. The central and peripheral results for Cu+Cu collisions are compared to the p+p parameterized function and the $N_{\rm part}$ scaled Au+Au peripheral results. Furthermore, the inverse slopes of the exponential function fit to the data give the effective temperature.

The function consists of two terms. The first term denotes an exponential function with the free parameters A and T. The parameter T is the inverse slope, and it implies the effective temperature of the created matter. The second term of the function represents the scaled p+p parameterization. The parameters in the second term are calculated by the fit on the measured direct

photon spectra in p+p collisions at $\sqrt{s}$ = 200 GeV. The data points are measured by the virtual photon method at the low transverse-momentum region p_T < 6 GeV/c, and the real photon measurement results are also shown together at the high transverse-momentum region 4 < p_T < 10 GeV/c. The inverse slope are 285 ± 53 (stat) ± 57 (syst) MeV/c for minimum bias collisions, 333 ± 72 (stat) ± 45 (syst) MeV/c for 0–40% centrality events, and 237 ± 117 (stat) ± 212 (syst) for 40–94% centrality events, respectively.

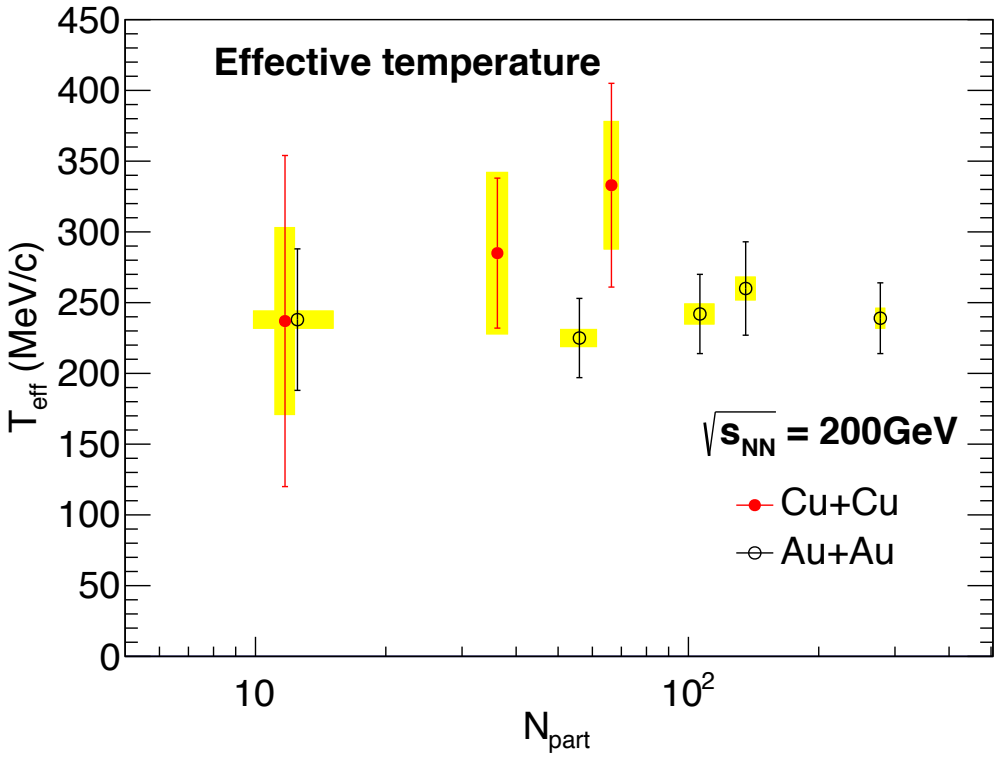

Figure 4.5: The effective temperature as a function of $N_{\rm part}$ for Cu+Cu and Au+Au collisions at $\sqrt{s_{NN}}$ = 200 GeV

The $N_{\rm part}$ dependence of the effective temperature is investigated shown in Fig. 4.5. The measured temperature is compared to the Au+Au results at $\sqrt{s_{NN}}$ = 200 GeV. The Cu+Cu data points present in the small-$N_{\rm part}$ region. There is no clear $N_{\rm part}$-dependence on the effective temperature in the same collision energy.

4.3 Rapidity density

Integrated direct photon yields called the rapidity densities are further investigated in Cu+Cu collisions. The rapidity density at the mid-rapidity is calculated by summing the direct photon yields in given transverse momentum bins considered with the bin width correction:

$$\frac{dN}{dy} = 2\pi \sum_{p_T^i > 1\mathrm{GeV}/c} \left({p_T}^i y_\gamma^i C_{bw}^i \Delta {p_T}^i \right), \tag{4.5}$$

$$C_{bw}^i = \int_{p_T.\mathrm{min}}^{p_T.\mathrm{max}} f_{\mathrm{fit}}\left(p_T\right) dp_T / \left[f_{\mathrm{fit}({p_T}^i)} \Delta {p_T}^i \right], \tag{4.6}$$

where y_γ^i and $\Delta {p_T}^i$ are the direct photon yield and transverse momentum bin-width for the ith p_T bin, respectively. $f_{\mathrm{fit}}\left(p_T\right)$ is the fit function to the data points of direct photon spectra.

Figure 4.6 shows the rapidity densities in Cu+Cu collisions with three centrality bins at $\sqrt{s_{NN}}$ = 200 GeV as functions of N_{part}. The rapidity density tends to increase logarithmically as a function of N_{part}. The rapidity density clearly increase with N_{part}, whereas the effective temperature are approximately 250 MeV/c independent N_{part}. The Cu+Cu rapidity densities are compared with the Au+Au results at the same collision energy [42]. A simple power-law function with the fixed power of 1.25 is employed to fit both the Cu+Cu and Au+Au results, and the function is reported in Ref. [44]. The Cu+Cu data give the data points in the small N_{part} region. The simple function works well to describe the N_{part} dependence. The direct photon rapidity density for the different collision system-size at the same collision energy seems to follow the identical scaling. It suggests that the sources of low transverse-momentum direct photons are no qualitative change for different centrality and system size at $\sqrt{s_{NN}}$ = 200 GeV.

Comparison to other collision systems

The Cu+Cu rapidity density results are further compared to the other collision systems with different collision energies and collision sizes. Figure 4.7 shows the integrated direct-photon yields ($p_T > 1.0$ GeV/c) as a function of $dN_{\mathrm{ch}}/d\eta$ for various collision systems, including the Cu+Cu results [44]. $dN_{\mathrm{ch}}/d\eta$ is a charged particle multiplicity. It is roughly proportional to N_{part}

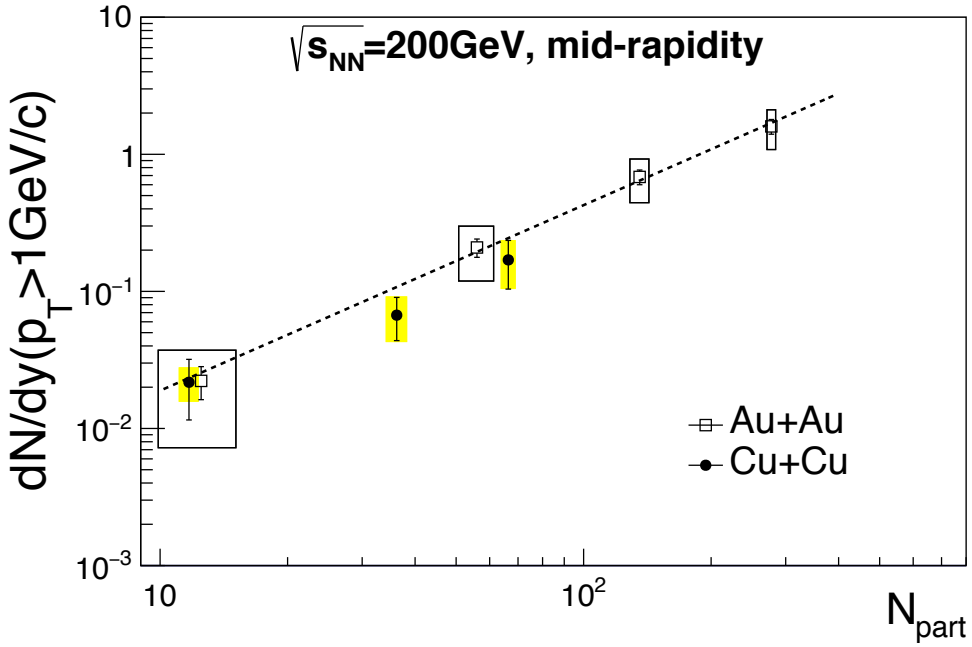

Figure 4.6: Rapidity densities of the direct photon yield for $p_T > 1$ GeV/c as functions of $N_{\rm part}$ and $dN_{\rm ch}/d\eta$ together with the Au+Au results. The power-law functions are the fit results for the Au+Au data.

for fixed beam energy, and it does not saturate unlike $N_{\rm part}$. $dN_{\rm ch}/d\eta$ signifies the system size at the hadronization. The rapidity densities in heavy-ion collisions are fitted by a power-law function with a fixed power of 1.25. The power-law function describes the $dN_{\rm ch}/d\eta$ dependence of the rapidity densities for heavy-ion collisions well. The rapidity density of the fit to p+p data and pQCD calculations seem to be the similar power to the heavy-ion collision resutls, although the yield is smaller.

The rapidity densities in the heavy-ion collision results measured in the wide range of the collision energy from $\sqrt{s_{NN}} = 39$ to 2760 GeV, and different collision systems follow the same scaling behavior. Even if the number of charged particles is the same, the initial conditions of the QGP should be different for different collision energies. If thermal photons are the dominant source at the low transverse-momentum region, the result suggests that thermal photons are emitted near the QGP-hadron transition. The direct photon spectrum itself has a large yield, suggesting an early contribution. However,

its integral, rapidity density implies that low transverse-momentum direct photons arise from the collision's late stage. Besides, the simple power-law function, which is only two parameters, empirically describes the heavy-ion collision data very well. It suggests that some fundamental commonality is underlying the production mechanism of the direct photon production.

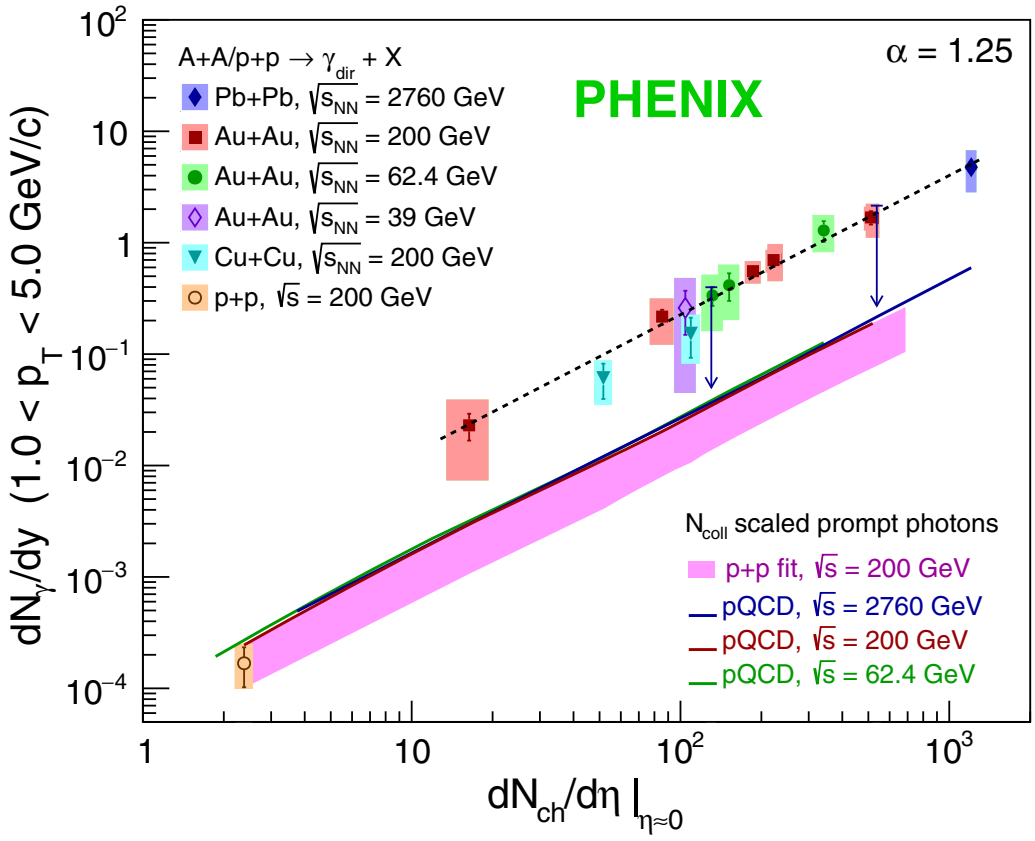

Figure 4.7: Rapidity densities of direct photons with $p_T > 1$ GeV/c as a function of $dN_{\rm ch}/d\eta$. The rapidity densities cover the wide range of collision energies from $\sqrt{s_{NN}} = 39$ to 2760 GeV and the collision nuclei of Au+Au, Pb+Pb, and Cu+Cu. The rapidity density data are fitted by a power-law function with the fixed $\alpha = 1.25$. [44]

Chapter 5

Summary and Conclusion

We have studied the production of low transverse-momentum direct photons in Cu+Cu collisions at $\sqrt{s_{NN}} = 200$ GeV. We have measured direct photons by the virtual photon method with the PHENIX experiment at the RHIC collider in Brookhaven National Laboratory.

The direct photon fraction as a function of transverse momentum is obtained for three centrality classes: minimum bias, 0–40% and 40–94%. The measured fractions are compared to the expectations from next-to-leading-order (NLO) perturbative-quantum-chromodynamics (pQCD) calculations. The results have an excess over the NLO pQCD calculations in all centrality classes. The excess appears the contribution of thermal photons from the hot medium. The Cu+Cu results are compared to the results in p+p, d+Au, and Au+Au collisions at $\sqrt{s_{NN}} = 200$ GeV. An excess over the theoretical calculations is seen in the Cu+Cu and Au+Au results, whereas the p+p and d+Au results correspond with the calculations. The excess in the Cu+Cu results is relatively modest compared to the Au+Au results. It is possible due to a smaller volume of the created medium.

Direct photon spectra have been measured, and these are compared with the binary scaled p+p results. The Cu+Cu spectra have an excess yield above the scaled p+p, as well as in the Au+Au collisions. The Cu+Cu spectra are also compared with the Au+Au results scaled by the $N_{\rm part}$ ratio, and the spectra are consistent within the uncertainties. An exponential fit to the excess yield gives inverse slopes of 285±53(stat)±57(syst) MeV/c for minimum bias collisions and 333±72(stat)±45(syst) MeV/c for the most central 0–40%, and 237±117(stat)±66(syst) MeV/c for 40–94% centralities. The calculated inverse slopes indicate the effective temperature of the created

medium, and no $N_{\rm part}$ dependence is found in the temperature at the given collision energy of $\sqrt{s_{NN}} = 200$ GeV.

The $N_{\rm part}$ dependence of the direct photon rapidity density is further investigated. The Cu+Cu results are compared with the Au+Au results. The Cu+Cu data points help to look at the dependence in the small $N_{\rm part}$ region. An increasing trend for $N_{\rm part}$ is reported in Au+Au collisions, and the Cu+Cu results follow the same $N_{\rm part}$ dependence. A simple power-law function empirically describes the dependence with a fixed power of 1.25. This result suggests that the principal source of low transverse-momentum direct photons is no qualitative change. Moreover, the collision energy dependence of the direct-photon rapidity density is discussed, and the charged-particle multiplicity ($dN_{\rm ch}/d\eta$) dependency is shown. The Cu+Cu results provide new data points in the small $dN_{\rm ch}/d\eta$ region. The rapidity density for low transverse-momentum direct photons in heavy-ion collisions follow the same $dN_{\rm ch}/d\eta$ scaling in the wide range of collision energy between 39 to 2760 GeV. This result implies that the direct photon sources are similar across the wide collision energy region. Even if $dN_{\rm ch}/d\eta$ is the same, the initial conditions should be different if the collision energy is different. Therefore, the scaling suggests that the low transverse-momentum direct photons are produced near the QGP-hadron transition.

This thesis provides the collision system-size dependence of low transverse-momentum direct-photon production. The Cu+Cu results improve the knowledge of the direct photon production, especially in the small $N_{\rm part}$ and $dN_{\rm ch}/d\eta$ regions. Theoretical models qualitatively express the direct photon production; however, quantitative understanding has not yet been achieved. The rapidity density of direct photons follows the unified scaling regardless of collision system size and energy. The Cu+Cu collisions provide new results in a small $dN_{\rm ch}/d\eta$ region, but there is still a gap between the p+p collision results. The PHENIX experiment has taken the data for small collision systems, such as p+Au and ^{3}He+Au collisions to understand the direct photon production in smaller $dN_{\rm ch}/d\eta$ region than the Cu+Cu peripheral collisions. The studies of direct photon production in small collision systems have begun, and it will help quantitative understanding of low transverse-momentum direct photon production.

Acknowledgements

I would like to express the most profound appreciation to my supervisor, Prof. K. Shigaki. He gave me continuous guidance and support. He also gave me an excellent opportunity to join the PHENIX collaboration. Without his agreement of my travel to Brookhaven National Laboratory, I would not have finished this thesis. I would like to heartfelt appreciate Prof. Y. Yamaguchi, who advises and support my thesis work. I would never finish this thesis without his valuable advice and discussions. I would also like to express my deepest gratitude to Dr. Y. Akiba for his support. He gave me insightful comments and generous support. His book on Quark-Gluon Plasma was also an excellent reference for this thesis. I am grateful to Assoc. Prof. K. Homma for his insightful suggestions for this thesis. He also taught me much knowledge and technical skills of the Beam-Beam Counter in the PHENIX experiment.

I must gratefully acknowledge Dr. H. En'yo for the financial support during JRA at RIKEN. Without his help, I would not have completed this thesis. I would like to thank Prof. T. Sugitate. He taught me Quark-Gluon Plasma and the history of particle physics. I would also like to acknowledge Assoc. Prof. T Miyoshi for his comment on my thesis and presentation.

I express my sincere thanks to the member of the Paper Preparation Group 200 in the PHENIX collaboration. I owe a significant debt to Prof. R. Seto. I would also like to thank the PHENIX collaboration. I have greatly benefited from the conveners of the physics working group meetings, including Prof. V. Riabov and Dr. T. Sakaguchi. Those people give me constructive comments and warm encouragement. I also appreciate Dr. C. H. Pinkenburg, Dr. C. Mickey, and Mr. S. Stoll for their cooperation in the BBC operation and maintenance.

I would like to show my most tremendous appreciation to Dr. Y. Nakamiya, Mr. D. Watanabe, Dr. K. M. Kijima, Dr. M. Ouchida, and Mr. M. Nihashi,

who taught me much knowledge and many technical skills. In particular, Mr. M. Nihashi gave me a lot of supports for life at BNL. I would like to offer my special thanks to all the people who worked together at BNL and RIKEN. Thanks to them, I was able to enjoy BNL and RIKEN life.

Appendix A

Data table

Table A.1: Direct photon fraction in Cu+Cu minimum bias

p_T	r_γ	Stat. error	Syst. error
$1.0< p_T <1.5$GeV/c	0.045	0.022	0.548
$1.5< p_T <2.0$GeV/c	0.116	0.027	0.231
$2.0< p_T <3.0$GeV/c	0.064	0.032	0.334
$3.0< p_T <5.0$GeV/c	0.168	0.072	0.195

Table A.2: Direct photon fraction in Cu+Cu 0–40% centrality

p_T	r_γ	Stat. error	Syst. error
$1.0< p_T <1.5$GeV/c	0.044	0.025	0.618
$1.5< p_T <2.0$GeV/c	0.127	0.032	0.259
$2.0< p_T <3.0$GeV/c	0.090	0.038	0.315
$3.0< p_T <5.0$GeV/c	0.217	0.085	0.213

Table A.3: Direct photon fraction in Cu+Cu 40–94% centrality

p_T	r_γ	Stat. error	Syst. error
1.0< p_T <1.5GeV/c	0.065	0.034	0.350
1.5< p_T <2.0GeV/c	0.061	0.046	0.357
2.0< p_T <3.0GeV/c	0.088	0.060	0.434

Table A.4: Direct photon yield in Cu+Cu minimum bias

p_T	Mean	Stat. error	Syst. error
1.1874	0.0121337	0.00611175	0.00635632
1.7006	0.00304398	0.000811146	0.000621467
2.2915	0.000287172	0.000153236	8.98173e-05
3.4444	3.24082e-05	1.65889e-05	5.26481e-06

Table A.5: Direct photon yield in Cu+Cu 0–40% centrality

p_T	Mean	Stat. error	Syst. error
1.1875	0.0289627	0.0172251	0.017096
1.7008	0.00805553	0.00229759	0.00181826
2.2898	0.00097946	0.000454379	0.000280948
3.445	0.000104529	5.22027e-05	1.74203e-05

Table A.6: Direct photon yield in Cu+Cu 40–94% centrality

p_T	Mean	Stat. error	Syst. error
1.1879	0.00478253	0.00266948	0.00156414
1.7034	0.000411663	0.000329365	0.000137916
2.297	0.000116383	8.59435e-05	4.5993e-05

Table A.7: Direct photon rapidity density in Cu+Cu collisions

Centrality	dN/dy	Stat. error	Syst. error
Minimum Bias	0.0670627	0.0233227	0.0239785
0–40%	0.169709	0.0657873	0.0646457
40–94%	0.0217306	0.0101927	0.00592101

Bibliography

[1] RIKEN BNL Research Center. Quantum chromodynamics. `https://www.bnl.gov/riken/research/QCD.php`.

[2] Edward V. Shuryak. Quark-Gluon Plasma and Hadronic Production of Leptons, Photons and Psions. *Sov. J. Nucl. Phys.*, 28:408, 1978.

[3] Andreas Ipp. Quark gluon plasma. `http://hep.itp.tuwien.ac.at/~ipp/qgp.html`.

[4] David J. Gross and Frank Wilczek. Ultraviolet Behavior of Nonabelian Gauge Theories. *Phys. Rev. Lett.*, 30:1343–1346, 1973.

[5] J. D. Bjorken. Energy Loss of Energetic Partons in Quark - Gluon Plasma: Possible Extinction of High p(t) Jets in Hadron - Hadron Collisions. 8 1982.

[6] Szabolcs Borsanyi, Gergely Endrődi, Zoltan Fodor, Antal Jakovac, Sandor D Katz, Stefan Krieg, Claudia Ratti, and Kalman K Szabo. The qcd equation of state with dynamical quarks. *Journal of High Energy Physics*, 2010(11):77, 2010.

[7] K. Johnson. A Field Theory Lagrangian for the {MIT} Bag Model. *Phys. Lett. B*, 78:259–262, 1978.

[8] Krishna Rajagopal. Mapping the QCD phase diagram. *Nucl. Phys. A*, 661:150–161, 1999.

[9] K. Adcox et al. Formation of dense partonic matter in relativistic nucleus-nucleus collisions at RHIC: Experimental evaluation by the PHENIX collaboration. *Nucl. Phys. A*, 757:184–283, 2005.

[10] John Adams et al. Experimental and theoretical challenges in the search for the quark gluon plasma: The STAR Collaboration's critical assessment of the evidence from RHIC collisions. *Nucl. Phys. A*, 757:102–183, 2005.

[11] B. B. Back et al. The PHOBOS perspective on discoveries at RHIC. *Nucl. Phys. A*, 757:28–101, 2005.

[12] I. Arsene et al. Quark gluon plasma and color glass condensate at RHIC? The Perspective from the BRAHMS experiment. *Nucl. Phys. A*, 757:1–27, 2005.

[13] K. Adcox et al. Suppression of hadrons with large transverse momentum in central Au+Au collisions at $\sqrt{s_{NN}}$ = 130-GeV. *Phys. Rev. Lett.*, 88:022301, 2002.

[14] K.H. Ackermann et al. Elliptic flow in Au + Au collisions at (S(NN))**(1/2) = 130 GeV. *Phys. Rev. Lett.*, 86:402–407, 2001.

[15] S.S. Adler et al. Elliptic flow of identified hadrons in Au+Au collisions at s(NN)**(1/2) = 200-GeV. *Phys. Rev. Lett.*, 91:182301, 2003.

[16] Michael L. Miller, Klaus Reygers, Stephen J. Sanders, and Peter Steinberg. Glauber modeling in high energy nuclear collisions. *Ann. Rev. Nucl. Part. Sci.*, 57:205–243, 2007.

[17] Raimond Snellings. Elliptic Flow: A Brief Review. *New J. Phys.*, 13:055008, 2011.

[18] The STAR Collaboration. The search for qgp. `https://www.star.bnl.gov/~gorbunov/main/node5.html`.

[19] P. Stankus. Direct photon production in relativistic heavy-ion collisions. *Ann. Rev. Nucl. Part. Sci.*, 55:517–554, 2005.

[20] G. David, R. Rapp, and Z. Xu. Electromagnetic Probes at RHIC-II. *Phys. Rept.*, 462:176–217, 2008.

[21] Gabor David. Direct real photons in relativistic heavy ion collisions. *Rept. Prog. Phys.*, 83(4):046301, 2020.

[22] Simon Turbide, Ralf Rapp, and Charles Gale. Hadronic production of thermal photons. *Physical Review C*, 69(1):014903, 2004.

[23] Norman M. Kroll and Walter Wada. Internal pair production associated with the emission of high-energy gamma rays. *Phys. Rev.*, 98:1355–1359, 1955.

[24] Rupa Chatterjee, Lusaka Bhattacharya, and Dinesh K. Srivastava. Electromagnetic probes. *Lect. Notes Phys.*, 785:219–264, 2010.

[25] A. Adare et al. Detailed measurement of the e^+e^- pair continuum in $p+p$ and Au+Au collisions at $\sqrt{s_{NN}} = 200$ GeV and implications for direct photon production. *Phys. Rev. C*, 81:034911, 2010.

[26] Robert D. Pisarski. Phenomenology of the Chiral Phase Transition. *Phys. Lett. B*, 110:155–158, 1982.

[27] A. Adare et al. Dielectron production in Au+Au collisions at $\sqrt{s_{NN}}$=200 GeV. *Phys. Rev. C*, 93(1):014904, 2016.

[28] L. Adamczyk et al. Dielectron Mass Spectra from Au+Au Collisions at $\sqrt{s_{\rm NN}} = 200$ GeV. *Phys. Rev. Lett.*, 113(2):022301, 2014. [Addendum: Phys.Rev.Lett. 113, 049903 (2014)].

[29] L. Adamczyk et al. Measurements of Dielectron Production in Au+Au Collisions at $\sqrt{s_{\rm NN}} = 200$ GeV from the STAR Experiment. *Phys. Rev. C*, 92(2):024912, 2015.

[30] Jaroslav Adam et al. Measurements of Dielectron Production in Au+Au Collisions at $\sqrt{s_{NN}}$= 27, 39, and 62.4 GeV from the STAR Experiment. 10 2018.

[31] Sarah Campbell. Dilepton continuum at PHENIX. *J. Phys. Conf. Ser.*, 230:012034, 2010.

[32] L. Adamczyk et al. Dielectron azimuthal anisotropy at mid-rapidity in Au + Au collisions at $\sqrt{s_{NN}} = 200$ GeV. *Phys. Rev. C*, 90(6):064904, 2014.

[33] S.S. Adler et al. Centrality dependence of direct photon production in s(NN)**(1/ 2) = 200-GeV Au + Au collisions. *Phys. Rev. Lett.*, 94:232301, 2005.

[34] J. Adams et al. Transverse momentum and collision energy dependence of high p(T) hadron suppression in Au+Au collisions at ultrarelativistic energies. *Phys. Rev. Lett.*, 91:172302, 2003.

[35] S. S. Adler et al. High p_T charged hadron suppression in Au + Au collisions at $\sqrt{s}_{NN} = 200$ GeV. *Phys. Rev. C*, 69:034910, 2004.

[36] M.M. Aggarwal et al. Observation of direct photons in central 158-A-GeV Pb-208 + Pb-208 collisions. *Phys. Rev. Lett.*, 85:3595–3599, 2000.

[37] M.M. Aggarwal et al. Interferometry of direct photons in central Pb-208+Pb-208 collisions at 158-A-GeV. *Phys. Rev. Lett.*, 93:022301, 2004.

[38] Simon Turbide, Ralf Rapp, and Charles Gale. Hadronic production of thermal photons. *Phys. Rev. C*, 69:014903, 2004.

[39] A. Adare et al. Enhanced production of direct photons in Au+Au collisions at $\sqrt{s_{NN}} = 200$ GeV and implications for the initial temperature. *Phys. Rev. Lett.*, 104:132301, 2010.

[40] A. Adare et al. Direct photon production in d+Au collisions at $\sqrt{s_{NN}} =$ 200 GeV. *Phys. Rev. C*, 87:054907, 2013.

[41] L. Adamczyk et al. Direct virtual photon production in Au+Au collisions at $\sqrt{s_{NN}} = 200$ GeV. *Phys. Lett. B*, 770:451–458, 2017.

[42] A. Adare et al. Centrality dependence of low-momentum direct-photon production in Au+Au collisions at $\sqrt{s_{_{NN}}} = 200$ GeV. *Phys. Rev. C*, 91(6):064904, 2015.

[43] Grazyna Odyniec. Beam Energy Scan Program at RHIC (BES I and BES II) – Probing QCD Phase Diagram with Heavy-Ion Collisions. *PoS*, CORFU2018:151, 2019.

[44] A. Adare et al. Beam Energy and Centrality Dependence of Direct-Photon Emission from Ultrarelativistic Heavy-Ion Collisions. *Phys. Rev. Lett.*, 123(2):022301, 2019.

[45] Jaroslav Adam et al. Direct photon production in Pb-Pb collisions at $\sqrt{s_{\rm NN}} =$ 2.76 TeV. *Phys. Lett. B*, 754:235–248, 2016.

[46] A. Adare et al. Scaling properties of azimuthal anisotropy in Au+Au and Cu+Cu collisions at s(NN) = 200-GeV. *Phys. Rev. Lett.*, 98:162301, 2007.

[47] A. Adare et al. Deviation from quark-number scaling of the anisotropy parameter v_2 of pions, kaons, and protons in Au+Au collisions at $\sqrt{s_{NN}} = 200$ GeV. *Phys. Rev. C*, 85:064914, 2012.

[48] A. Adare et al. Systematic Study of Azimuthal Anisotropy in Cu+Cu and Au+Au Collisions at $\sqrt{s_{NN}} = 62.4$ and 200 GeV. *Phys. Rev. C*, 92(3):034913, 2015.

[49] H. Niemi, G.S. Denicol, P. Huovinen, E. Molnar, and D.H. Rischke. Influence of a temperature-dependent shear viscosity on the azimuthal asymmetries of transverse momentum spectra in ultrarelativistic heavy-ion collisions. *Phys. Rev. C*, 86:014909, 2012.

[50] Huichao Song, Steffen A. Bass, Ulrich Heinz, Tetsufumi Hirano, and Chun Shen. Hadron spectra and elliptic flow for 200 A GeV Au+Au collisions from viscous hydrodynamics coupled to a Boltzmann cascade. *Phys. Rev. C*, 83:054910, 2011. [Erratum: Phys.Rev.C 86, 059903 (2012)].

[51] R.A. Soltz, I. Garishvili, M. Cheng, B. Abelev, A. Glenn, J. Newby, L.A. Linden Levy, and S. Pratt. Constraining the initial temperature and shear viscosity in a hybrid hydrodynamic model of $\sqrt{s_{NN}}$=200 GeV Au+Au collisions using pion spectra, elliptic flow, and femtoscopic radii. *Phys. Rev. C*, 87(4):044901, 2013.

[52] Paul Romatschke and Ulrike Romatschke. Viscosity Information from Relativistic Nuclear Collisions: How Perfect is the Fluid Observed at RHIC? *Phys. Rev. Lett.*, 99:172301, 2007.

[53] Peter F Kolb, Ulrich Heinz, Pasi Huovinen, Kari J Eskola, and Kimmo Tuominen. Centrality dependence of multiplicity, transverse energy, and elliptic flow from hydrodynamics. *Nuclear Physics A*, 696(1-2):197–215, 2001.

[54] A. Adare et al. Azimuthally anisotropic emission of low-momentum direct photons in Au+Au collisions at $\sqrt{s_{NN}} = 200$ GeV. *Phys. Rev. C*, 94(6):064901, 2016.

[55] A. Adare et al. Observation of direct-photon collective flow in $\sqrt{s_{NN}} =$ 200 GeV Au+Au collisions. *Phys. Rev. Lett.*, 109:122302, 2012.

[56] A. Adare et al. Measurements of Higher-Order Flow Harmonics in Au+Au Collisions at $\sqrt{s_{NN}} = 200$ GeV. *Phys. Rev. Lett.*, 107:252301, 2011.

[57] Shreyasi Acharya et al. Direct photon elliptic flow in Pb-Pb collisions at $\sqrt{s_{\rm NN}} = 2.76$ TeV. *Phys. Lett. B*, 789:308–322, 2019.

[58] M Harrison, T Ludlam, and S Ozaki. Rhic project overview. *Nuclear Instruments and Methods in Physics Research Section A: Accelerators, Spectrometers, Detectors and Associated Equipment*, 499(2-3):235–244, 2003.

[59] K. Adcox et al. PHENIX detector overview. *Nucl. Instrum. Meth. A*, 499:469–479, 2003.

[60] The PHENIX Collaboration. The detector configuration in run-5. `https://www.phenix.bnl.gov/runs/run05.html`.

[61] M. Allen et al. PHENIX inner detectors. *Nucl. Instrum. Meth. A*, 499:549–559, 2003.

[62] K. Ikematsu et al. A Start - timing detector for the collider experiment PHENIX at RHIC-BNL. *Nucl. Instrum. Meth. A*, 411:238–248, 1998.

[63] Torsten Dahms. Dilepton spectra in p+p and au+au collisions at rhic, 2008.

[64] Clemens Adler, Alexei Denisov, Edmundo Garcia, Michael J. Murray, Herbert Strobele, and Sebastian N. White. The RHIC zero degree calorimeter. *Nucl. Instrum. Meth. A*, 470:488–499, 2001.

[65] The PHENIX collaboration. The phenix central magnet. `https://www.phenix.bnl.gov/index.html`.

[66] S.H. Aronson et al. PHENIX magnet system. *Nucl. Instrum. Meth. A*, 499:480–488, 2003.

[67] K Adcox, NN Ajitanand, J Alexander, D Autrey, R Averbeck, B Azmoun, KN Barish, VV Baublis, R Belkin, S Bhaganatula, et al. Phenix central arm tracking detectors. *Nuclear Instruments and Methods in Physics Research Section A: Accelerators, Spectrometers, Detectors and Associated Equipment*, 499(2-3):489–507, 2003.

[68] M. Aizawa et al. PHENIX central arm particle ID detectors. *Nucl. Instrum. Meth. A*, 499:508–520, 2003.

[69] L Aphecetche, TC Awes, J Banning, S Bathe, A Bazilevsky, S Belikov, ST Belyaev, C Blume, M Bobrek, D Bucher, et al. Phenix calorimeter. *Nuclear Instruments and Methods in Physics Research Section A: Accelerators, Spectrometers, Detectors and Associated Equipment*, 499(2-3):521–536, 2003.

[70] S.S. Adler et al. PHENIX on-line and off-line computing. *Nucl. Instrum. Meth. A*, 499:593–602, 2003.

[71] Stephen Scott Adler et al. PHENIX on-line systems. *Nucl. Instrum. Meth. A*, 499:560–592, 2003.

[72] F Pilat, L Ahrens, M Bai, DS Barton, J Beebe-Wang, M Blaskiewicz, JM Brennan, D Bruno, P Cameron, R Connolly, et al. Operations and performance of rhic as a cu-cu collider. In *Proceedings of the 2005 Particle Accelerator Conference*, pages 4281–4283. IEEE, 2005.

[73] S.S. Adler et al. Identified charged particle spectra and yields in Au+Au collisions at S(NN)**1/2 = 200-GeV. *Phys. Rev. C*, 69:034909, 2004.

[74] R. Brun, F. Bruyant, M. Maire, A. C. McPherson, and P. Zanarini. GEANT3. 9 1987.

[75] A. Trivedi et al. PISA: The PHENIX experiment simulation package. In *9th International Conference on Computing in High-Energy and Nuclear Physics*, 4 1997.

[76] Arthur M. Poskanzer and S.A. Voloshin. Methods for analyzing anisotropic flow in relativistic nuclear collisions. *Phys. Rev. C*, 58:1671–1678, 1998.

[77] Torbjorn Sjostrand, Stephen Mrenna, and Peter Z. Skands. A Brief Introduction to PYTHIA 8.1. *Comput. Phys. Commun.*, 178:852–867, 2008.

[78] Torbjörn. Sjöstrand et al. Pythia 8. `http://home.thep.lu.se/~torbjorn/pythia81html/Welcome.html`.

[79] H. L. Lai, J. Huston, S. Kuhlmann, J. Morfin, Fredrick I. Olness, J. F. Owens, J. Pumplin, and W. K. Tung. Global QCD analysis of parton structure of the nucleon: CTEQ5 parton distributions. *Eur. Phys. J. C*, 12:375–392, 2000.

[80] A. Adare et al. Onset of π^0 Suppression Studied in Cu+Cu Collisions at $\sqrt{s_{NN}}$ =22.4, 62.4, and 200 GeV. *Phys. Rev. Lett.*, 101:162301, 2008.

[81] Rolf Hagedorn. Multiplicities, p_T Distributions and the Expected Hadron $\rightarrow$ Quark - Gluon Phase Transition. *Riv. Nuovo Cim.*, 6N10:1–50, 1983.

[82] A. Adare et al. System-size dependence of open-heavy-flavor production in nucleus-nucleus collisions at $\sqrt{s_{NN}}$=200 GeV. *Phys. Rev. C*, 90(3):034903, 2014.

[83] A. Adare et al. Measurements of e^+e^- pairs from open heavy flavor in p+p and d+A collisions at $\sqrt{s_{NN}}$ = 200 GeV. *Phys. Rev. C*, 96(2):024907, 2017.

[84] C. Patrignani et al. Review of Particle Physics. *Chin. Phys. C*, 40(10):100001, 2016.

[85] S.S. Adler et al. Common suppression pattern of eta and pi0 mesons at high transverse momentum in Au+Au collisions at S(NN)**(1/2) = 200-GeV. *Phys. Rev. Lett.*, 96:202301, 2006.

[86] R. I. Dzhelyadin et al. Study of the Electromagnetic Transition Formfactor in $\omega \rightarrow \pi^0\mu^+\mu^-$ Decay. *JETP Lett.*, 33:228, 1981.

[87] L.E. Gordon and W. Vogelsang. Polarized and unpolarized prompt photon production beyond the leading order. *Phys. Rev. D*, 48:3136–3159, 1993.